

Assessment of the 3D spatial distribution of the Calcium/Phosphorus ratio in bone



Andria Hadjipanteli

Department of Medical Physics and Bioengineering

University College London

A thesis submitted for the degree of

Doctor of Philosophy

2013

I, Andria Hadjipanteli confirm that the work presented in this thesis is my own. Where information has been derived from other sources, I confirm that this has been indicated in the thesis.

Signature.....

Acknowledgements

I would firstly like to express my gratitude to my supervisors, who helped me develop as a researcher, as well as a person, throughout my PhD studies. I would like to acknowledge Professor Robert Speller, for his warm welcome to the excellent environment of the radiation physics group, and for his continual guidance and support throughout my studies. I am also very grateful to Dr Alessandro Olivo and Dr Paul Fromme, by whom I have been challenged and from whom I have received excellent direction. Furthermore, I would like to thank Dr Jie Huang for all her help and support.

I really appreciated the knowledge and encouragement given by Dr Nicolaos Kourkoumelis. In addition, I would like to acknowledge Garrard Cole for his help in the use of the scanning electron microscope system and Dr Jamie McClelland for his help in the use of NifTK platform.

I would like to gratefully acknowledge the financial support received from EPSRC that has allowed me to perform this work. Furthermore, I would like to thank the Department of Medical Physics of the University of Ioannina for providing the samples for this project.

In addition, I would like to express my appreciation to Dr Prodromos Kaplanis for his career guidance since my school years.

I would like to express my many thanks to all my friends in the radiation physics group, with whom I had an enjoyable and unforgettable time, especially in the last two years of my PhD studies, in and out of the office. I would specifically like to thank Tasos for being a good advisor and friend.

There are no words to express my thanks to Paul for providing love, laughter, and emotional and scientific support that made my “battle” much easier. In addition, my friends Charalambos, Charis, Chrystalla and Natasa, even though miles far away, they were always by my side when I needed them.

I would like dedicate this thesis to my family, my parents Pantelis and Agathi, my brother Nicolas, my sisters Kyriaki and Christiana, and her

family, Marios and little Agathi, my grandmother Kyriakoula, who always believed in me and guided me with love all these years. I would like to thank them for their patience and support.

Abstract

The purpose of this study was the development of a technique for the non-invasive assessment of the 3D spatial distribution of the Ca/P ratio in bone, which can be applied in a conventional computed-tomography (CT) system, to investigate the variation of Ca/P ratio in healthy and osteoporotic bone, and to potentially enhance osteoporosis understanding and diagnosis. Three-material mass-fraction decomposition CT dual energy analysis (CT-DEA) was developed and optimised for the assessment of Ca/P ratio. As part of this process, density values are provided as a bi-product. The technique was optimised and experimentally applied through a microCT system. The target of the optimisation was to achieve a precision of better than 0.09 in the Ca/P ratio, in order to be able to distinguish between all healthy and osteoporotic regions. Electron dispersive X-ray spectroscopy (EDX) was used to evaluate the performance of CT-DEA on bone apatite. Ca/P ratio measurements were made on the same healthy and inflammation mediated osteoporotic (IMO) rabbit cortical bone surfaces, using CT-DEA and EDX. The mean difference in the Ca/P ratio between the two techniques was 0.11 ± 0.08 ($8 \pm 6\%$) and the correlation was $R^2=0.69$, suggesting sufficient confidence in the experimental capabilities of the CT-DEA technique. Healthy and IMO rabbit, both collagen-free and intact, cortical bone samples were assessed by CT-DEA. Qualitative analysis of the results involved the production of Ca/P ratio and density distribution maps. Quantitative analysis involved the quantification of the Ca/P ratio and density across the whole sample and in volumes of interest, as well as the low Ca/P ratio proportion in each sample. Furthermore, a 3D region growing technique was used to study the uniformity of Ca/P ratio in the samples. Results showed differences in both density and Ca/P ratio between healthy and IMO bone samples, supporting their use as possible osteoporosis indicators and the use of the developed technique for further studies.

List of Publications

Journal Publications

- Hadjipanteli, A., Kourkoumelis, N., Fromme, P., Olivo, A., Huang, J. and Speller, R. (2013). A new technique for the assessment of the 3D spatial distribution of the Calcium/Phosphorus ratio in bone apatite. *Physiological Measurement*. (accepted)
- Hadjipanteli, A., Kourkoumelis, N., Fromme, P., Olivo, A., Huang, J. and Speller, R. (2013). Bone density and Ca/P ratio 3D assessment in cortical bone using CT-DEA. (in preparation)

Conference Publications

- Electronic Poster: Hadjipanteli, A., Olivo, A., Kourkoumelis, N., Fromme, P., Huang, J. and Speller, R. (2013) A new technique for the assessment of the 3D spatial distribution of the Ca/P ratio in bone for osteoporosis diagnosis and fracture prevention. *European Congress of Radiology* DOI: 10.1594/ecr2013/C-2397.
- Poster presentation: Hadjipanteli, A., Kourkoumelis, N., Tzaphlidou, M., Speller, R. (2013) Ca/P concentration ratio of bone tissues evaluated by energy dispersive X-ray spectroscopy and X-ray microtomography. *ICDD Spring Meetings*.
- Proceedings paper, poster presentation: Hadjipanteli, A., Huang, J., Fromme, P., Kourkoumelis, N., Olivo, A., Tzaphlidou, M., Speller, R. (2012) Development of a new technique for the investigation of the 3D spatial distribution of the Calcium/Phosphorus ratio effect in osteoporosis. *Osteoporosis International* 23:605.

Contents

Contents	6
List of Figures	10
List of Tables	17
1 Osteoporosis and its diagnosis	19
1.1 Overview	19
1.2 Bone	19
1.3 Osteoporosis diagnosis	20
1.3.1 The importance of osteoporosis diagnosis and prevention . . .	20
1.3.2 Current imaging methods of osteoporosis diagnosis	21
1.3.3 Other imaging methods for monitoring osteoporosis	24
1.3.4 The study of mechanical properties of bone for monitoring osteoporosis	26
1.4 The approach of this study to the problem of osteoporosis	28
1.4.1 Bone mineral material density	29
1.4.2 The Calcium/Phosphorus ratio in bone	31
1.4.3 The aim of this study	34
1.5 Structure of the rest of this thesis	35
2 Materials and Methods	36
2.1 Overview	36
2.2 Micro-computed tomography	36
2.2.1 X-ray interactions with matter	36
2.2.2 Principles of computed tomography	38
2.2.3 X-Tek benchtop micro-computed tomography system	40
2.3 Scanning electron microscope	41

2.3.1	Electrons interaction with matter	42
2.3.2	Principles of scanning electron microscopy	43
2.4	Dual energy analysis	45
2.4.1	Historical background of dual energy analysis in bone decom- position	45
2.4.2	Principles of dual energy analysis technique	46
2.4.3	Computed tomography dual energy analysis (CT-DEA)	47
2.4.4	CT-DEA for density and Ca/P ratio assessment in bone min- eral content	49
2.4.5	CT-DEA for density and Ca/P ratio assessment in intact bone	53
2.5	Samples	55
2.5.1	Di-potassium phosphate solutions	55
2.5.2	Bone phantoms	55
2.5.3	Bone samples	56
2.6	Summary	59
3	CT-DEA optimisation	60
3.1	Overview	60
3.2	Optimisation of the magnification parameter	60
3.2.1	Unsharpness	61
3.2.2	Edge imaging	62
3.2.3	Unsharpness analysis	64
3.2.4	Results: optimum sample magnification	67
3.2.5	Conclusions on the optimum magnification parameter	69
3.3	Optimisation of the X-ray spectral pair	71
3.4	Optimum average energies	73
3.4.1	Theoretical optimum average energies	73
3.4.2	Beam filtration	75
3.4.3	System power	76
3.4.4	Beam hardening	79
3.5	Scattering	81
3.6	Signal to noise ratio	82
3.6.1	Noise in CT dual energy imaging	82
3.6.2	CT grey value calibration	83
3.6.3	Number of projections	85

3.6.4	Number of frames	85
3.6.5	Correction of the centre of rotation	86
3.7	Conclusions on the optimum imaging conditions	87
3.8	Summary	88
4	Evaluation of CT-DEA	90
4.1	Overview	90
4.2	Theoretical precision of CT-DEA	90
4.2.1	Simulation method	90
4.2.2	Results: theoretical precision	91
4.3	Experimental precision of CT-DEA	93
4.3.1	Experimental methods	93
4.3.2	Results: experimental precision	94
4.4	Evaluation of CT-DEA performance for Ca/P ratio assessment in bone apatite	99
4.4.1	CT sample imaging and CT-DEA analysis	99
4.4.2	SEM sample imaging and EDX analysis	101
4.4.3	Image registration and analysis	101
4.4.4	Results: Areal Ca/P ratio assessment using EDX	104
4.4.5	Results: CT-DEA performance for Ca/P ratio assessment in bone apatite	108
4.5	Summary	110
5	Density and Ca/P ratio assessment in healthy and osteoporotic cortical bone apatite	111
5.1	Overview	111
5.2	Experimental methods	112
5.2.1	Collagen-free bone imaging	112
5.2.2	Qualitative and quantitative analysis	113
5.2.3	Statistical analysis	114
5.3	Results: comparing healthy and IMO bones	115
5.3.1	Density and Ca/P ratio bulk results	115
5.3.2	Density and Ca/P ratio in volumes of interest	118
5.3.3	Low Calcium/Phosphorus ratio proportion	122
5.3.4	3D region-grown low Ca/P ratio	123
5.3.5	Low Ca/P ratio homogeneity	127

5.4	Results: comparing different bone sites	127
5.5	Results: comparing healthy and IMO bones for each bone site	133
5.6	Summary	135
6	Density and Ca/P ratio assessment in healthy and osteoporotic intact cortical bone	137
6.1	Overview	137
6.2	Experimental methods	137
6.3	Results: comparing healthy and IMO bones	139
6.3.1	Density and Ca/P ratio bulk results	139
6.3.2	Density and Ca/P ratio in volumes of interest	141
6.3.3	Low Ca/P ratio proportion	142
6.4	Results: comparing different bone sites	143
6.5	Results: comparing healthy and IMO bones for each bone site	144
6.6	Summary	145
7	Concluding remarks and future potential of CT-DEA for density and Ca/P ratio 3D assessment	147
7.1	Prospects for CT-DEA system: current limitations and future developments	147
7.1.1	Progress achieved in present study	147
7.1.2	Limitations of the current CT-DEA technique and results	149
7.2	Future system developments towards mechanical testing	151
7.3	Future system developments towards clinical implementation	152
7.4	Conclusions	152
	References	154

List of Figures

1.1	Diagnostic thresholds for women based on the distribution of bone mineral density (BMD) in the young healthy female population (Kanis and Glu [2000]).	22
1.2	“Different types of mineral density: $BMD_{material}$ and $BMD_{compartment}$ (A and B) in trabecular bone and (C and D) cortical bone. The mass of mineral (in grey) determining $BMD_{material}$ and $BMD_{compartment}$ is identical (mass 1 = mass 2), but the volume (encircled by black lines) differs (volume 2 > volume 1). Therefore, $BMD_{material}$ is higher than $BMD_{compartment}$. (E) BMD_{total} is defined as the mass of mineral divided by the volume enclosed by the periosteal envelope. This definition can be applied to the entire bone, part of the bone, or section through the bone” (Rauch and Schoenau [2001]).	30
2.1	Variation of the mass attenuation coefficient with photon energy for the two main bone components: apatite in the chemical form of hydroxyapatite (blue line) and collagen (red line). The attenuation of hydroxyapatite is decomposed into the attenuation of its components: Ca (circles), PO_4 (diamonds), OH (squares).	38
2.2	Construction of an image intensifier (Webb [1988]).	40
2.3	The X-Tek microCT system.	41
2.4	Some of the signals which can be used in an SEM system (Goodhew et al. [2001]).	42
2.5	The parts of an SEM system (Goodhew et al. [2001]).	43
2.6	Parts of an energy dispersive spectrometer (Goodhew et al. [2001]).	44
2.7	Dual energy imaging of the chest. (a) Low kVp and (b) High kVp images are decomposed into (c) soft tissue and (d) bone images (Tountountzis [2009]).	47
2.8	Relations of (a) $F(Z_{eff})$ to Z_{eff} and (b) Z_{eff} to \bar{m}_L for bone mineral content composites of different Ca/P ratio.	52
2.9	Relations of (a) $F(Z_{eff})$ to Z_{eff} and (b) Z_{eff} to \bar{m}_L for bone composites (85% mineral and 15% collagen by weight) of different Ca/P ratio.	54

2.10	Typical bone phantoms.	56
2.11	A typical bone sample.	58
3.1	The geometric blurring or penumbra, U_f due to the focal spot.	61
3.2	Method of calculation of the angle of missalignment θ	64
3.3	(a) The edge image at a magnification of 6. The selected area shows the area of interest ($20 \times \text{pixels} \times 150 \text{ pixels}$) used for the production of the ERF, and in (b) the magnified area of interest, showing the blurring at the edge.	65
3.4	(a) The profile of the edge object ERF. (b) Following differentiation, the LSF and thus the FWHM (given by the open circle points) can be found.	66
3.5	FWHM versus $\frac{d_2}{d_1}$. The crosses represent the measured FWHM values of the LSF of the edge, while the smooth line shows the fitting of equation 3.7 ($f = 12 \mu\text{m}$ and $U_d = 630 \mu\text{m}$, calculated using the χ^2 test) through these points.	67
3.6	Plot of χ^2 value versus focal spot size versus intrinsic detector resolution. The black arrow represents the minimum χ^2 value which indicates the focal spot size and intrinsic detector resolution values that provide the best fitting of (equation 3.7), to the measured results of unsharpness (FWHM).	68
3.7	Detector MTF. The spatial frequency value which corresponds to 0.1 (dotted line) of the response of the detector represents the intrinsic detector resolution.	69
3.8	The total unsharpness (black) or effective system resolution, versus magnification, M , of an image of an object in the microCT. The effect of the focal spot (blue) and the detector (red) are shown separately. For a $U < 150 \mu\text{m}$ an $M > 4.1$ is required.	70
3.9	A microCT image of the femur of the hind leg of a sheep, implanted with 9 mm synthetic Hydroxyapatite (HA). The image was acquired at $M = 10$ (i.e. effective system resolution is $63 \mu\text{m}$). The trabecular structure of the bone can be resolved.	70
3.10	Absolute error in Ca/P ratio for different energy combinations.	75
3.11	Example of the effect of current on the average energy. The measurement of average energy was made at 95 kVp and using 0.2 mm Samarium, 0.35 mm Gadolinium and 0.5 mm Tin for filtration. The expected average energy was 81 keV as shown by the red line. The errors represent the standard deviation.	77

3.12	The average dose measurements, made every 50 seconds, at 95 kVp, 500 μ A and a beam filtration of 0.35 mm Gadolinium and 0.4 mm Samarium. The plot demonstrates the instability in dose with time when the microCT is used at a high power. The error bars represent the standard deviation.	78
3.13	Example of a slice of a microCT image of a bone phantom, acquired at 95 kVp and 500 μ A and with an external filtration to source window of 0.35 mm Gadolinium (Gd) and 0.5 mm Tin (Sn). Ring artefacts being present.	78
3.14	Absolute error in Ca/P ratio for different energy combinations. The highlighted light-grey areas represent the energies eliminated for practical reasons such as flux instability with time and the production of ring artefacts in the images.	79
3.15	(a) A slice through a microCT image of a bone phantom with a line profile selection, and (b) its corresponding profile plot. Beam hardening is shown by the ‘cupped appearance’ of the line profile. The red line represents the expected appearance attenuation coefficient.	80
3.16	Absolute error in Ca/P ratio for different energy combinations. The highlighted light-grey areas represent the energies eliminated for practical reasons such as flux instability with time and ring artefacts in the images. The highlighted dark-grey areas represent the energies eliminated due to the presence of beam hardening in the microCT images.	81
3.17	Absolute error in Ca/P ratio for different combinations of noise in μ_L and μ_H	83
3.18	Calibration of the microCT grey value to the theoretical linear attenuation coefficient (in cm^{-1}) at the (a) low energy and (b) high energy imaging conditions. The calibration was performed using five K_2HPO_4 solutions of different concentrations. The red line through the points represents the resulting equation of the calibration procedure.	84
3.19	A reconstructed bone phantom microCT image (a) without and (b) with the correction of the COR, using CT Pro software.	87
3.20	Simulated X-ray energy spectra used in CT-DEA.	88
4.1	Simulation results. Deviation from the expected f_{Ca} (blue triangles) and f_P (pink squares) for phantoms of different Ca/P ratio. All phantoms of same Ca/P ratio had identical f_{Ca} and f_P errors.	92
4.2	Simulation results. Deviation from the expected Ca/P ratio for phantoms of different Ca/P ratio. The red line represents the minimum difference between healthy and IMO bone samples found in literature.	93

4.3	(a) Density colour map, and (b) its corresponding density map after thresholding, produced after the analysis of a phantom ($\text{Ca}(\text{H}_2\text{PO}_4)_2(\text{H}_2\text{O})$) CT slice for phantom volume and density calculations. The yellow and red voxels were rejected from further analysis.	94
4.4	Density colour map plots extracted from five K_2HPO_4 solutions of known density of (a) 1.39, (b) 1.59, (c) 1.94, (d) 2.36 and (e) 2.68 g/cm^3 . All maps are 2.3 mm \times 2.3 mm. Each voxel is 96 μm^3	95
4.5	Experimental results. CT-DEA average density results of K_2HPO_4 solutions shown in green circles. The red line expresses the relation of a CT-DEA density result to the actual density of the sample. Error bars represent the standard deviation.	95
4.6	(a) SEM backscatter image of a phantom ($\text{CaHPO}_4 \cdot 2(\text{H}_2\text{O})$), and (b) the histogram produced for the whole surface. The peak at ~ 0 grey value shows the presence of air.	96
4.7	Experimental results. CT-DEA average density results of bone phantoms shown in green. The red line expresses the relation of a CT-DEA density result to the actual density of the sample. Error bars represent the standard deviation.	97
4.8	Ca/P ratio maps plots extracted from phantoms of known Ca/P ratio of (a) 0.5, (b) 1.0, (c) 1.5 and (d) 1.67. All maps are 3 mm \times 3 mm. Each voxel is 96 μm^3	98
4.9	Experimental results. Phantom CT-DEA average Ca/P ratio results shown in blue circles. The red line expresses the relation of a CT-DEA density result to the actual density of the sample. Some samples had similar/identical results, therefore they overlap of the graph: there are two results at 0.70 and 0.71, and two results at 1.21. Error bars represent the standard deviation.	98
4.10	Original low energy CT images ((a) and (c)) and the corresponding Ca/P ratio 2D maps ((b) and (d)) for rear tibia rabbit bone samples. The samples are healthy ((a) and (b)) and IMO ((c) and (d)) The selected areas represent ROIs in the samples.	100
4.11	(a) Backscatter SEM image, (b) CT-DEA Ca/P ratio colour map of the surface of an IMO bone sample. The mapping of the two images in NifTK is shown in (c).	102
4.12	A case where there was a misalignment of the pixels of CT image to the pixels of the SEM image, due to the different orientation of the sample to the detector in the two systems.	103

4.13 (a) SEM backscatter image, with a selection of the ROI, and (b) its corresponding EDX spectrum, acquired using a bone phantom of Ca/P ratio = 0.5.	104
4.14 EDX measurements. Deviation from the expected f_{Ca} (blue triangles) and f_P (pink squares) for phantoms of different Ca/P ratio.	105
4.15 Experimental results. Expected phantom Ca/P ratio versus EDX-measured average Ca/P ratio. The red line expresses the expected relationship.	106
4.16 SEM backscatter image of a healthy bone sample. The rectangular selections represent the selected areas analysed in this sample.	106
4.17 Examples of the spectra acquired from (a) a healthy bone sample and (b) an IMO bone sample.	107
4.18 CT-DEA Ca/P ratio versus EDX Ca/P ratio of 58 regions of interest in 8 samples; 4 healthy (blue) and 4 osteoporotic (red).	108
5.1 A typical 3D image of one healthy rabbit rear tibia bone sample, acquired using the microCT system.	112
5.2 (a) Ca/P ratio map of a rear tibia bone sample, and (b) its corresponding Ca/P ratio map after thresholding. Yellow ($Ca/P \text{ ratio} \leq 0$) and red ($0 < Ca/P \text{ ratio} \leq 1.00$) areas were rejected, while green ($1.00 < Ca/P \text{ ratio} \leq 1.49$) and blue ($1.5 < Ca/P \text{ ratio} \leq 1.80$) were used for bone analysis.	113
5.3 The bulk densities of 18 collagen-free bone samples, with healthy samples in red and IMO samples in blue, filled circles. Error bars have been excluded, for clarity, as the standard error < 0.002 . Some samples had identical results: for IMO samples there are two results at 2.23; for healthy samples there are two results at 2.24.	116
5.4 The bulk Ca/P ratios of 18 collagen-free bone samples, with healthy samples in red, open circles and IMO samples in blue, filled circles. Error bars have been excluded for clarity, as the standard error < 0.001 . Some samples had identical results: for IMO sameples there are three results at 1.65 and two at 1.68; for healthy samples there are three results at 1.67.	117
5.5 One image slice of a front tibia bone sample at (a) low energy and (b) high energy. The corresponding density colour map (c) and Ca/P ratio colour map (d) are products of CT-DEA. Each voxel is $96 \mu\text{m}^3$	118
5.6 Ca/P ratio colour maps ((a) and (c)) and their corresponding density colour maps ((b) and (d)), extracted from two different positions within a healthy rear tibia sample image. The resolution of all colour maps is $96 \mu\text{m}$. The red squares illustrate VOIs, of volume 0.03 mm^3 analysed quantitatively in table 5.3.	119

5.7	Ca/P ratio colour maps ((a), (c) and (e)) and their corresponding density maps ((b), (d) and (f)), extracted from three different positions of an IMO femur sample image. The resolution of the colour maps is 96 μm . The red squares illustrate VOIs, of volume 0.03 mm^3 , analysed quantitatively in table 5.4.	121
5.8	The low Ca/P ratio proportion of the 18 collagen-free bone samples. The healthy samples are shown in blue, filled circles and the IMO samples in red, open circles.	122
5.9	Low Ca/P ratio grown regions for healthy rear tibia (a), femur (b) and front tibia (c) bone samples. Voxels are shown by crosses, with the ‘low’ (1-1.49) Ca/P ratio range in red, and the ‘high’ (1.5-1.8) Ca/P ratio range in blue.	124
5.10	Low Ca/P ratio grown regions for IMO rear tibia (a), femur (b) and front tibia (c) bone samples. Voxels are shown by crosses, with the ‘low’ (1-1.49) Ca/P ratio range in red, and the ‘high’ (1.5-1.8) Ca/P ratio range in blue.	125
5.11	The region-grown low Ca/P ratio proportion of the 18 collagen-free bone samples. The healthy samples are shown in blue, filled circles and the IMO samples in red, open circles. Some samples had similar results, overlapping on the plot: for IMO sameples there is one result at 0 and one at 0.07.	126
5.12	The low Ca/P ratio homogeneity (region-grown (RG) low Ca/P ratio volume to low Ca/P ratio total sample volume), of the 18 collagen-free bone samples. The healthy samples are shown in blue, filled circles and the IMO samples in red, open circles.	127
5.13	The bulk densities of the collagen-free 6 rear tibiae (RT), 6 femurs (F) and 6 front tibiae (FT); healthy (red) and IMO (blue) samples. Error bars have been excluded, for clarity, as the standard error<0.002. Some samples had identical results: for IMO samples there are two results at 2.23; for healthy samples there are two results at 2.24.	128
5.14	The bulk Ca/P ratios of the collagen-free 6 rear tibiae (RT), 6 femurs (F) and 6 front tibiae (FT); healthy (red) and IMO (blue) samples. Error bars have been excluded, for clarity, as the standard error<0.001. Some samples had identical results: for IMO samples there are three results at 1.65 and two at 1.68; for healthy samples there are three results at 1.67.	129
5.15	The low Ca/P ratio proportion of the collagen-free six RT, six F and six FT; healthy (red) and IMO (blue) samples.	130
5.16	The region-grown low Ca/P ratio proportion of the collagen-free six RT, six F and six FT; healthy (red) and IMO (blue) samples. There is an overlap in healthy samples results: one at 0 and one at 0.07.	131

5.17 The low Ca/P ratio homogeneity (region-grown (RG) low Ca/P ratio volume to low Ca/P ratio total sample volume), of the collagen-free six RT, six F and six FT; healthy (red) and IMO (blue) samples. 131

6.1 (a) Original low energy image of a rear tibia bone sample, and (b) its corresponding density map after thresholding. Yellow ($\rho \leq 0$) and red ($0.01 < \rho \leq 1.25$ and $\rho > 3.60$) areas were rejected, while blue areas ($1.25 < \rho \leq 3.60$) were used for bone analysis. 138

6.2 The densities (g/cm^3) of the 18 intact bone samples, with healthy samples in red and IMO samples in blue. Error bars have been excluded as the standard error < 0.002 139

6.3 The Ca/P ratios of the low-density ($1.25\text{-}3.60 \text{ g/cm}^3$) region of 18 intact bone samples, with healthy samples in red and IMO samples in blue. Error bars have been excluded as the standard error < 0.001 140

6.4 Density maps, ((a) and (c)), and their corresponding Ca/P ratio maps, ((b) and (d)), of one healthy (top) and one IMO (bottom) rear tibia intact cortical bone sample. The resolution of all maps is $96 \mu\text{m}$ 141

6.5 The bulk Ca/P ratios of the intact 9 healthy (red) and 9 IMO (blue) samples, after thresholding with density. 142

List of Tables

1.1	The approximate percentage of the constituents (by weight) of bone; both inorganic and organic as found in literature (Miller and Martin [1968], Bauer and Link [2009], Gong et al. [1964]), Dorozhkin [2009]).	20
2.1	Summary of the studies of the main CT-DEA material decomposition algorithms.	49
2.2	Details of phantoms used in CT-DEA precision evaluation.	56
2.3	Numbers of bone samples for each bone type and each bone site.	58
2.4	Bone samples sets and usage.	59
3.1	Examples of filtration added to a 100 kVp beam using Samarium (Sm), Gadolinium (Gd), Tin (Sn) and Copper (Cu) of different thicknesses. The average energy (\bar{E}) is shown and the presence of ring artefacts is stated. In all cases the number of projections was 360 and the number of frames was 256.	76
3.2	Examples of filtration added to a 50 kVp and 60 kVp beam using Aluminium (Al) of different thicknesses, t . The average energy (\bar{E}) is shown and the presence of beam hardening is stated. In all cases the number of projections was 360 and the number of frames was 256.	80
3.3	Experimental imaging conditions used for all the imaging performed using the X-tek benchtop microCT system in this study.	88
4.1	Simulation results. Deviation from the expected density for ten phantoms of different Ca/P ratio. All phantoms of same chemical formula (but different density) had identical density errors.	91
4.2	Simulation results. Deviation from expected density with different weight proportions of air in a given voxel of bone.	97
4.3	Details of collagen-free bone samples.	109

5.1	Statistical analyses, using the Student's t-test, performed on the studied parameters of collagen-free bone samples (set 1) and their corresponding sections, where the results can be found.	115
5.2	Student's t-test results of the bulk density and bulk Ca/P ratio, of the nine healthy and nine IMO bone samples.	116
5.3	Average density and Ca/P ratio results of the selected VOIs of a healthy rear tibia, shown in figure 5.6.	120
5.4	Average density and Ca/P ratio results of the selected VOIs, of an IMO femur, shown in figure 5.7.	122
5.5	Student's t-test results of the low Ca/P ratio proportion, of the nine healthy and nine IMO bone samples.	123
5.6	Student's t-test results of the region-grown low Ca/P ratio proportion, of the nine healthy and nine IMO bone samples.	126
5.7	Student's t-test results of region grown low Ca/P ratio volume to the whole bone low Ca/P ratio volume, of the nine healthy and nine IMO bone samples.	128
5.8	Student's t-test results of the studied parameters, between the 3 healthy and 3 IMO rear tibia, femur and front tibia bone samples. The number of observations in each analysis was 3.	132
5.9	Student's t-test results of the studied parameters, of the 3 healthy and 3 IMO rear tibia, femur and front tibia bone samples.	134
6.1	Statistical analyses, using the Student's t-test, performed on the studied parameters of intact bone samples (set 2) and their corresponding sections where the results can be found.	139
6.2	Student's t-test results of the bulk density (g/cm ³) and bulk Ca/P ratio, of the 9 healthy and 9 IMO bone samples.	140
6.3	Average density and Ca/P ratio results of the selected ROIs of a healthy rear tibia, shown in figure 6.4	142
6.4	Student's t-test results of the low Ca/P ratio proportion, of the nine healthy and nine IMO bone samples.	142
6.5	Student's t-test results of the studied parameters, between the 3 healthy and 3 IMO rear tibia, femur and front tibia intact cortical bone samples. The number of observations in each analysis was three.	144
6.6	Student's t-test results of the studied parameters, of the three healthy and three IMO rear tibia, femur and front tibia bone samples.	145

Chapter 1

Osteoporosis and its diagnosis

1.1 Overview

In this chapter osteoporosis and its diagnosis are discussed. In section 1.2, a brief background on bone is given. In section 1.3, osteoporosis and its consequences are described and the importance of early osteoporosis diagnosis is explained. Furthermore, the current imaging and mechanical methods of osteoporosis diagnosis and monitoring are described. In section 1.4, the approach of the current study to the problem of osteoporosis is given. The study of bone material density and Ca/P ratio in bone as possible osteoporosis indicators is discussed. Finally, in section 5, the structure of the rest of this thesis is presented.

1.2 Bone

Bone is a type of dense connective tissue. Tissue types found in bone include osseous tissue (primary bone tissue), bone marrow, endosteum and periosteum, nerves, blood vessels and cartilage. Osseous tissue is the type of tissue mostly known to be affected by osteoporosis.

Osseous tissue is a relatively hard and lightweight composite material, formed mostly (60%-85% by weight) of Calcium Phosphates (table 1.1) (Miller and Martin [1968], Bauer and Link [2009], Gong et al. [1964]), Dorozhkin [2009]). Chemically this is often termed as Calcium hydroxyapatite $\text{Ca}_{10}(\text{PO}_4)_6(\text{OH})_2$, which is combined to the organic part of the bone, Type-I collagen (15-40%). The stoichiometric fraction of Calcium and Phosphorus in hydroxyapatite is Calcium 39.9%, Phosphorus 18.5%. Thus the stoichiometric atomic Ca/P ratio is 1.67. However, the exact composition of bone varies depending on sex, age, type and site, and alterations are also known to occur in bone metabolic diseases (Akesson et al. [1994]).

Osseous tissue is synthesised by osteoblasts which produce the consequent min-

Table 1.1: The approximate percentage of the constituents (by weight) of bone; both inorganic and organic as found in literature (Miller and Martin [1968], Bauer and Link [2009], Gong et al. [1964]), Dorozhkin [2009]).

Inorganic phases	wt%	Bioorganic phases	wt%
Calcium Phosphates	60-85	Collagen type I	15-40
Water	~9	Non-collagenous proteins	~3
Carbonates	~4	Polysacchrides, lipids, cytokines	Balance
Citrates	~0.9	Primary bone cells	Balance
Sodium	~0.7		
Magnesium	~0.5		
Other traces	Balance		

eralization. Osseous tissue is resorbed by the osteoclasts which are activated by hormones to secrete substances that break down the bone. Bone turnover is the combination of bone formation by osteoblasts and resorption by osteoclasts. Bone formation and resorption are activated at variable rates. There is not any particular factor that predicts whether bone formation or bone resorption will dominate. The almost constant bone mass, is achieved by BMUs (bone multicellular units, cells with which bone renews itself), which counter balance bone formation and resorption.

There are two types of osseous tissue. One of them is the cortical (or compact) bone, the hard outer layer of bones, with a porosity of 5-30%. The interior of the bone is the trabecular bone tissue (also called cancellous or spongy bone), which is a network of rod- and plate-like elements that make the bone lighter and allow room for blood vessels and marrow. Its porosity is 3-90% (Hall [2006]).

1.3 Osteoporosis diagnosis

1.3.1 The importance of osteoporosis diagnosis and prevention

Osteoporosis is by definition a progressive, systematic skeletal disease characterised by low bone mass and micro-architectural deterioration of bone tissue, with a consequent increase in bone fragility and susceptibility to fracture (Kanis et al. [1994], Ferguson [2004]). The most common osteoporotic fracture sites are spine (120 000/year in UK), hip (over 60 000/year in UK) and wrist (50 000/year in UK) (van Staa et al. [2001]). Osteoporosis is multi-factorial in origin and the precise pathogenesis is still unknown.

The incidence of osteoporosis is known to increase with advancing age. Osteoporosis is most common in women after the menopause, but may develop in men and premenopausal women. During the menopause the ovaries produce lower levels of the female hormone oestrogen, which is essential for bone health. Thus after the

menopause the rate of bone loss that starts in the thirties accelerates, increasing the risk of osteoporosis (Heaney et al. [1978]).

Fractures due to osteoporosis represent a significant social and medical problem in terms of treatment and rehabilitation and will become an even greater problem, as the proportion for the elderly increases. The personal cost of the occurrence of a related fracture is the restriction of activity, mobility and in severe cases the result of fatality. During the first 12 months after a hip fracture over half of people who walked unaided prior to the fracture will be unable to walk independently. 55% of patients will require assistance at home and 33% will experience difficulty sleeping due to pain (Osnes et al. [2004]).

The number of people suffering from osteoporosis is large. It is estimated that one in two women and one in five men will suffer a fracture after the age of 50 (van Staa et al. [2001]). Osteoporosis DALYs (disability adjusted life years) are higher than cancer DALYs (Johnell and Kanis [2006]). Also, it has been reported that the lifetime risk of fracture in women at age 50 years is greater than the risk of breast cancer or cardiovascular disease (WHO Study Group, 1994).

The financial costs in the UK for NHS and government are significant. As an indication, in the UK, the average hospital stay for hip fracture is 30 days. Osteoporosis costs 2.3 GBP billion a year; that is 6 GBP million a day, according to the National Osteoporosis Society.

Osteoporosis is usually called the “silent epidemic”. It can be present in a patient for many years without any apparent consequence, either as an apparent symptom or as a medical condition that would prompt the patient to seek medical advice.

At present there is no widely applicable method of fully restoring skeletal strength once it has been lost (Kanis et al. [2005], Teegarden et al. [1998]). In common with a number of disorders, osteoporosis should be viewed as a condition for which prevention is better than cure. Under the above aspects reliable early diagnosis and prevention of osteoporosis are of particular importance.

1.3.2 Current imaging methods of osteoporosis diagnosis

Bone mineral density (BMD), an areal parameter with units of g/cm^2 , describes the bone mineral within a projected area and is the conventional method of assessing osteoporosis, in the clinical environment under the scale developed by the World Health Organisation (WHO). Measurements of BMD are widely recognised as being effective at identifying patients who are at a higher than the average risk of fracture (Kanis and Glu [2000]).

The WHO scale is based on comparison of a patient’s BMD with that of a healthy young adult. A T-score is defined as the patient’s BMD value minus young

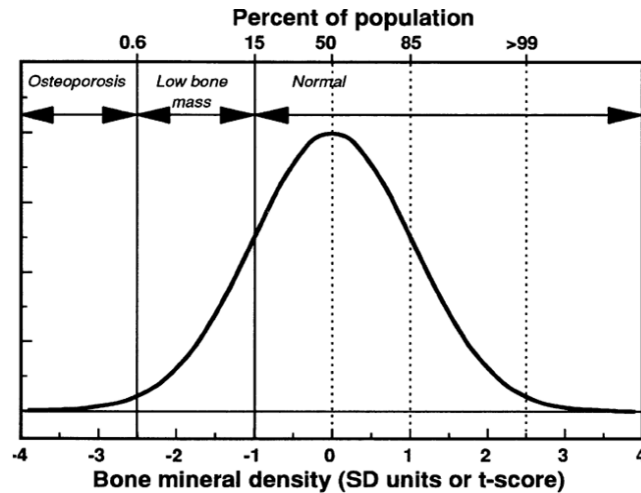


Figure 1.1: Diagnostic thresholds for women based on the distribution of bone mineral density (BMD) in the young healthy female population (Kanis and Glu [2000]).

reference BMD divided by young-reference standard deviation at the corresponding anatomical site. The WHO scale is divided into three main different categories: normal, low bone mass (osteopenia) and osteoporosis. A T-score equal to or less than -2.5 is taken as an indication of osteoporosis (figure 1.1).

In the early 1960s, routine quantitative BMD was achieved by measuring the absorption of a highly collimated photon beam from a single-energy radionuclide source (SPA), such as Iodine-125 or Americium-241. The anatomical site being measured was generally immersed in a water bath to correct for overlying soft tissue. The difference in attenuation between an image of bone and water and an image of water only was attributed to bone. The distal radius and calcaneus were the sites that were generally measured. Later low-dose single X-ray absorptiometry (SXA) replaced SPA as it provides a greater photon flux and thus improved spatial resolution and precision. However, SPA and SXA could not be applied to important fracture sites and so dual photon absorptiometry (DPA) techniques were introduced. These utilised Gadolinium-153 which emits gamma radiation with strong peaks at 41 keV and 102 keV. Bone was assumed to be a two component system; mineral and soft tissue. When soft tissue absorption was subtracted out, the BMD could be determined from the absorption of each beam by bone. In 1989, a new instrumentation, enabled Dual Energy X-ray Absorptiometry (DEXA or DXA) to be conducted using two energies (usually around 70 and 140 kVp) generated by an X-ray generator and k-edge filter (Lewis et al. [1994]). The preferred anatomic sites for DEXA measurement of bone mineral include the typical osteoporotic fracture sites of lumbar spine, proximal femur and distal radius, as well as whole body assessment (Langton [2010], Kazakia and Majumdar [2006]). Other advantages of DEXA include low effective radiation dose (around 0.07-5.90 μSv depending on scan mode) compared with dose entailed by other radiological procedures, low cost, ease of use and speed (2-20 min-

utes depending on the scan mode) of measurement (Lewis et al. [1994]). DEXA BMD measurement is the gold standard for T-score assessment and the standard by which other bone imaging measures are evaluated.

However, many authors have reported inconsistency in WHO classification using DEXA. It is widely, but not universally accepted. Physicians face the dilemma of deciding which patients should receive long-term treatments.

One of the major problems that have been reported in the WHO classification is that classification is based on data collected from epidemiological studies on white, postmenopausal women. This has to be taken into consideration when looking at other cohorts of population, such as men. The choice of the corresponding reference population, bone age and the measurement site have a direct impact on the management of individual patients in clinical practice (Lu et al. [2001], Grampp et al. [1997], Kanis and Glu [2000]). The extent to which the threshold based classification depends on reference data used, was shown by Lu et al. [2001], who examined three models with different criteria and reference population for the diagnosis of osteoporosis.

Similarly, the choice of bone measurement technology has a direct impact on the management of individual patients in clinical practice (Lu et al. [2001], Grampp et al. [1997], Kanis and Glu [2000]). Device manufacturers typically use different reference populations for different machines. Grampp et al. [1997] showed that there is a small correlation (correlation coefficient, $r = 0.10-0.93$) among different commonly available methods of assessing bone mineral, and bone sites as well, for measuring the BMD and bone mineral content (BMC, the amount of mineral in the specific site scanned, when divided by the area measured, can be used to derive a value for BMD).

A false impression or confusion is sometimes created through the WHO classification. The risk factor is distributed throughout the whole population, leading to an arbitrary cut-off point that over or under-treats individuals at the extreme limits of each category. There is also terminology confusion as a T-score of -2.5 or less is considered to represent osteoporosis, and those with a T-score of between -1 and -2.5 are diagnosed with osteopenia. Subjects with a T-score of -2.5 therefore meet both definitions. A false impression might also be caused because there may be other reasons for low BMD, such as osteomalacia, hyper-parathyroidism, or a combination of two. Finally, there is considerable overlap in bone densities among normal individuals and those that suffer from bone fractures (Ciarelli et al. [1991]).

Moreover, DEXA calculates BMD using area (aBMD) and it is not an accurate measurement of true bone mineral density, due to the missing depth value in the calculation of bone mineral density (Bolotin and Sievänen [2001]). Furthermore, planar imaging, cannot differentiate between trabecular and cortical bone. Thus,

BMD measurement is independent of the ratio of trabecular to cortical bone and therefore does not give a complete picture of the strength of the bone (Kazakia and Majumdar [2006]).

Finally, in DEXA measurements it is assumed that the composition of imaged tissue is the same between different people. However, soft tissue is composed of variable amounts of fat and lean. Variations in fat-lean composition produce differences in the attenuation coefficients for soft tissue at both energies. Therefore, one must obtain an estimate of soft tissue composition in order to obtain accurate bone mineral and soft tissue masses.

1.3.3 Other imaging methods for monitoring osteoporosis

In addition to the established SPA, SXA, DPA and DEXA methods, there are a number of research methods for diagnosing osteoporosis.

Quantitative ultrasound (QUS) uses high frequency acoustic waves to measure how much energy is absorbed by the bone, generally referred to as Broadband Ultrasound Attenuation (BUA, dB MHz), or the speed of sound (SOS, ms^{-1}). Then BUA or SOS are then changed into the density of bone. The advantage of QUS is that the QUS unit is inexpensive and portable, scans quickly and does not utilise ionising radiation. It has been clinically demonstrated that BUA measurement of the calcaneus provides an accurate indication of osteoporosis fracture risk, particularly for hip fractures (Kazakia and Majumdar [2006]). Measurements can also be made at the phalanges and tibia. However, due to technical difficulties, ultrasound measurements cannot to date be performed at the common osteoporosis anatomical sites. In addition, there is a lack of uniformity and sensitivity of reported BUA measurements. QUS measures are inappropriate for long term monitoring of osteoporosis or response to drug therapy. Images are therefore not usually obtained by QUS systems (Langton [2010]).

A technique that is gaining increasing interest is magnetic resonance imaging (MRI). Usually associated with soft tissue imaging, it works in bone by measuring the water content of bone marrow and subtracting it by its background, which is trabecular bone and does not give any signal. From this, a 3D volumetric image of trabecular structure can be obtained and the bone architecture parameters (trabecular thickness, trabecular number) can be measured. Bone architectural parameters are becoming popular in osteoporosis research (Cohen et al. [2009], Laib et al. [2000]). In addition to being non-ionising it is possible to obtain high in-plane resolution of $\sim 150 \mu\text{m}$ and slice thicknesses of $\sim 300 \mu\text{m}$ (Majumdar [2008]). In predicting the existence of vertebral fractures it has been shown that distal radius MR images perform significantly better than DEXA scans of the same region (Kazakia

and Majumdar [2006]). However, MRI is only usually performed at peripheral sites such as the heel, knee and wrist due to signal to noise ratio (SNR) limitations.

Conventional radiography is a projected 2D imaging modality, used with a spatial resolution of up to 40 μm (Bauer and Link [2009]). Lateral chest radiographs are performed in many elderly patients and can be used to identify vertebral fractures. It is attractive because of its ease of use and availability. However, the big disadvantage is that large amounts of bone loss must be present before an abnormality is detected.

Computed tomography (CT) is used in bone imaging. Quantitative computed tomography (QCT) uses a conventional X-ray CT scanner, that can achieve in plane spatial resolution of $\sim 200 \mu\text{m}$, with slice thickness of $\sim 500 \mu\text{m}$. BMC may be determined separately for the trabecular and cortical bone components via a calibration phantom scanned adjacent to the subject. Volumetric BMD can then be found by dividing BMC by the corresponding tissue volume. Volumetric BMD is a robust measure for comparisons of bone density between populations. In clinical whole body CT scanners, QCT is being used increasingly, particularly at the lumbar spine (Kazakia and Majumdar [2006]).

The advantage of QCT over DEXA or QUS is 3D spatial resolution allowing for the assessment of volumetric BMD, in addition to macro-architecture. Comparing CT with MRI, CT has the advantage of directly visualising the bone. Limitations of QCT include the high radiation dose (approximately 60 μSv), around ten times higher than DEXA, and bigger expense.

The high capital and running costs associated with conventional CT scanner QCT assessment of volumetric bone density assessment has recently prompted the development of dedicated peripheral (p-QCT) systems. These can determine the volumetric density of the cortical and trabecular components at the distal radius and proximal tibia (Kazakia and Majumdar [2006]). Resolution of images using p-QCT is of the order of 80 μm . P-QCT inherently delivers a lower dose to the patient than standard spinal QCT as only the peripheral skeleton is irradiated. Doses are comparative to spinal DEXA ($< 2 \mu\text{Sv}$). P-QCT is often therefore used for detailed assessment of children, where it is particularly crucial to keep dose low. Peripheral scanners make QCT technology less expensive, easier to use and more accessible than traditional whole-body scanners. A disadvantage is that it is confined to peripheral sites, and it is not capable of generating images or direct measures within the spine or proximal femur (the typical bone sites of osteoporosis).

Micro-computed tomography (microCT) scanners have the advantages of conventional CT scanners, but in addition they reside at the highest hierarchy of resolution (up to 4 μm). This allowed for the separate determination of cortical, trabecular or integral bone architecture, with only a resolution of 150 μm required to visualise the trabecular network and to quantify morphological parameters (Ulrich et al. [1999]).

MicroCT has been used to study the trabecular and cortical architecture in humans (Majumdar [2008], Martn-Badosa et al. [2003], Nuzzo et al. [2003]) and rats (Laib et al. [2000]). It has also been used for mice, where the thinner bone structures require very high spatial resolution (Martn-Badosa et al. [2003]). Even though it is non-destructive, it is not used *in vivo* (at least not in humans). The reason is the long measurement time, the large amount of data for processing and the high radiation dose (Judex et al. [2003]), even though currently a number of *in vivo* microCT scanners are becoming commercially available. A big advantage of the 3D high resolution microCT images is that they help to monitor the effect of mechanical loading on structural and compositional changes (section 1.3.4). It was shown that it can be used to predict mechanical properties (Wachter et al. [2001]). Moreover, microCT allows the generation of micromechanical models of the scanned sample by converting bone voxels to mechanical elements that can be analysed by the finite element analysis method (van Der Linden et al. [2001], Shefelbine et al. [2005]).

1.3.4 The study of mechanical properties of bone for monitoring osteoporosis

“We have to hand a plethora of different bone densitometry techniques but often lose sight of what we are fundamentally trying to achieve, namely identification and monitoring of subjects at risk of an osteoporotic fracture through surrogates of mechanical integrity” (Langton [2010]). Bone is a biomaterial that is structurally adapted to different functions and loading situations (Cowin [1984]). Bone strength is the determining factor for bone quality and by assessing it one can more accurately gauge a patient’s susceptibility to a fracture. Of course there are some other factors that contribute to the risk of fracture due to osteoporosis. These are age, prior fragility fracture, a parental history of fracture, smoking, use of systemic corticosteroids, excess alcohol intake, rheumatoid arthritis.

Bone mechanical tests have been used to study osteoporosis for different aims and using different methods. The true gold standard measurement of the mechanical integrity of a bone is a destructive test, generally performed by compressing either a regional shaped sample or whole bone. FEA is an alternative to the experimental test. It is a simulated mechanical test that can be used to predict the stresses and strains on an object when loading conditions such as forces, moments or supports are applied to it. It has the advantage that the same bone can be tested under several different loading conditions, for example, torsion of bending, or different loading position.

The results from the mechanical compression/simulation tests are usually correlated with the results of imaging techniques in order to correlate a bone indicator,

for example density, microarchitecture, bone composition which can be assessed *in vivo* non-invasively, to bone strength. Studying the effect of an osteoporosis indicator on bone strength can result on the importance of this indicator on bone quality. If this indicator has a significant effect on bone quality it could then be used to diagnose osteoporosis.

In a study by Wachter et al. [2001] mineral density and porosity of femoral cortical bone from the mid-diaphysis of 24 patients were determined *in vitro* by microCT and then, the strength and the elastic modulus were assessed by a compression test. Results showed a significant negative correlation between porosity and yield stress stiffness and elastic modulus, and even stronger positive correlations between density and the mechanical parameters. Also, more recently, the contributions of trabecular microarchitecture, of the human lumbar spine, and its regional variation have been studied (Wegrzyn et al. [2010]) using mechanical compression test. In this study lumbar vertebrae were harvested fresh from 21 lumbar spines of human donors. They were tested, before the compression test, for BMD by dual-energy X-ray absorptiometry (DEXA) and microarchitecture by high-resolution peripheral quantitative computed tomography (HR-pQCT). A higher correlation was found between microarchitecture and mechanical behaviour (failure load, compressive stiffness, and work to failure) than BMD and mechanical behaviour. In a similar way, the correlation of the cortical mineral content of the radius, measured by QCT, to the compressive strength, measured using a compression test, was assessed (Louis et al. [1995]). In this study a high correlation was found between the mineral content, density and thickness of the cortical bone and its maximal stress.

Similarly, imaging and FEA were used together in order to find the correlation of density, trabecular micro-architecture to mechanical moduli and/or risk of fracture (Boutroy et al. [2008], Pistoia et al. [2002], Baum et al. [2010] Newitt et al. [2002]). Boutroy et al. [2008] used HR-pQCT to take images at the radius in 33 postmenopausal women with a prior history of fragility wrist fracture and 33 age-matched controls. The volumetric bone density, microarchitecture and microFE derived bone mechanical properties were assessed. The Young's moduli values of cortical and trabecular bone were found from literature and were assigned to them after the segmentation of trabecular and cortical bone tissue. Radius areal BMD was also measured by DEXA. Association between density, microarchitecture, mechanical properties and fracture status were evaluated. Their results suggest that bone mechanical properties assessed by microFE provide information about skeletal fragility and fracture risk not assessed by BMD or architecture measurements alone and are therefore likely to enhance the prediction of wrist fracture.

Similarly, Pistoia et al. [2002] reported stronger correlations between microFE analyses and measured failure load of the distal radius than those provided by bone

mass or bone structural parameter. In this study 54 embalmed cadaver arms were imaged using pQCT and structural indices were derived. Using these images microFE models were produced as well, with loading conditions that simulated real loading conditions that were later applied to the arms using a testing machine to produce a Colles-type fracture in the radii. Similar results were found by Baum et al. [2010] in a similar study.

Ulrich et al. [1999] and Newitt et al. [2002] used microCT and MRI respectively, to measure the structural parameters of normal and osteoporotic human bones. Then, microFEA models of these bones were produced using the microCT (Ulrich et al. [1999]) and MRI (Newitt et al. [2002]) images and reference values for trabecular Poisson's ratio (0.3) and Young's modulus (GPa). The directional Young's moduli, shear moduli and anisotropy ratios were calculated and were correlated to bone architecture and BMD. It was shown that the determination of mechanical properties of bone and the diagnosis of osteoporosis can be improved if, in addition, to BMD, the 3D bone microarchitecture is assessed.

In the studies above it was shown that the mechanical properties of bone, which determine bone quality, can be predicted by osteoporosis indicators measured using radiation imaging non-destructively. Correlations were studied between different osteoporosis indicators for example, bone microarchitecture, mineral content and density, and bone strength and/or risk of fracture.

1.4 The approach of this study to the problem of osteoporosis

As described in section 1.1 osteoporosis represents a serious medical and social problem. The use of aBMD measurements for osteoporosis diagnosis has significant disadvantages. Thus osteoporosis diagnosis needs to be enhanced. Furthermore, the pathogenesis of osteoporosis is unknown and multi-factorial in origin therefore research continues on the effect of other osteoporosis indicators, for example architectural, physical, chemical and biological factors, on bone quality.

In the current study the bone material density and Ca/P ratio in bone were studied as possible osteoporosis indicators. In the next section the reasons that support the study of bone material density and Ca/P ratio in bone for understanding, preventing and diagnosing osteoporosis are explained.

1.4.1 Bone mineral material density

As discussed in section 1.3.2 the bone size and bone mass are neglected by DEXA and the aBMD measurement. But even when these size-related problems are taken into account, densitometric data rarely interpret the biological processes in the bone. Increases in “bone density” during growth are often attributed uniformly to “bone mineralisation”. However, this might really represent greater cortical thickness, thicker trabeculae or incorporation of additional mineral into existing bone matrix.

To study the effect of biological processes only (and reject any structural processes) in the bone quality, $BMD_{material}$ has to be assessed. $BMD_{material}$ represents mineralization in its physiological sense and is identical for cortical and trabecular bone (Willnecker [2006]). Bone material is the extracellular bone matrix, whether mineralised or not. The relevant volume to calculate material density (true bone density) is the volume occupied by bone matrix and does not include air, marrow spaces, osteonal canals, lacunae and canaliculi. $BMD_{material}$ can be calculated as

$$BMD_{material} = \sum BMD_i v_i \quad (1.1)$$

where v is the volume fraction of component i in the material.

As shown in table 1.1 the different material components present in the bone matrix (non-cellular part of the bone) are apatite, organic constituents and water. Their material densities respectively are in the following ranges 2.85-3.20 g/cm³ (Robinson [1975]), 1.41-1.45 g/cm³ (Gong et al. [1964]) and 1 g/cm³. With an apatite volume of 40%, a collagen volume of 50% and water volume of 10% bone material density is ~ 2.01 g/cm³.

$BMD_{material}$ has to be distinguished from two different bone mineral density definitions (BMD) given in literature: (i) $BMD_{compartment}$ defined as the mass per unit volume in a bone’s trabecular and cortical tissue compartments, and (ii) BMD_{total} or apparent density, defined as the mass per unit volume in the entire bone (figure 1.2). These three different definitions of mineral density represent density at three different levels. As discussed by Rauch and Schoenau [2001] BMD_{total} is a function of $BMD_{compartment}$, which is in turn a function of $BMD_{material}$. Changes in $BMD_{compartment}$ are caused by variations in both $BMD_{material}$ and relative cortical or trabecular bone volume. Changes in BMD_{total} are caused by variations in both $BMD_{material}$ and relative cortical and trabecular bone volume.

Even though DEXA and QCT can be used to measure $BMD_{compartment}$ and BMD_{total} at particular bone sites, $BMD_{material}$ has not been assessed with noninvasive techniques (Rauch and Schoenau [2001]), until 2011 when Wagner et al. [2011] developed a grey value calibration approach that takes into account the presence of collagen, water and hydroxyapatite in bone. In the current study, CT-DEA is used

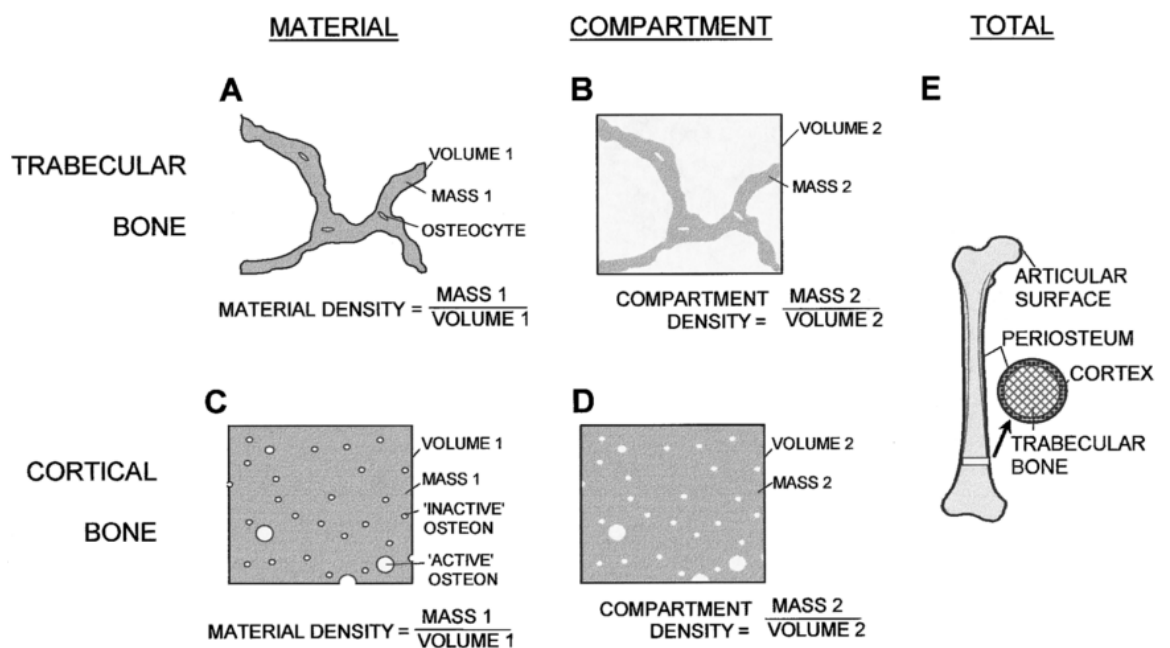


Figure 1.2: “Different types of mineral density: $BMD_{material}$ and $BMD_{compartment}$ (A and B) in trabecular bone and (C and D) cortical bone. The mass of mineral (in grey) determining $BMD_{material}$ and $BMD_{compartment}$ is identical (mass 1 = mass 2), but the volume (encircled by black lines) differs (volume 2 > volume 1). Therefore, $BMD_{material}$ is higher than $BMD_{compartment}$. (E) BMD_{total} is defined as the mass of mineral divided by the volume enclosed by the periosteal envelope. This definition can be applied to the entire bone, part of the bone, or section through the bone” (Rauch and Schoenau [2001]).

to assess $BMD_{material}$. For the rest of this thesis, bone density will have the meaning of $BMD_{material}$, unless stated otherwise.

1.4.2 The Calcium/Phosphorus ratio in bone

It was always assumed that the chemical composition of osteoporotic bone is the same as that of normal bone and in osteoporotic bone there is simply less bone (Avioli and Lindsay [1990]). However, more recent work has shown that variations in the chemical composition of the mineral or organic components of the bone may be important in understanding fragility fractures (McCreadie et al. [2006]). Such mineral composition changes may involve crystallite size and size distribution, structural rearrangement and/or substitution. At the molecular level, bone chemistry might have a significant effect on bone quality.

From the mechanical point of view hydroxyapatite (HA) provides the major support of bones. Bone is considered primarily as a HA reinforced collagen composite, with the additional secondary effect due to the arrangement of osteons (the fundamental function units of compact bone). Comparing the Young's modulus of HA (114 GNm^{-2}) and that of collagen (1 GNm^{-2}), with comparable volume fractions, HA is the major load bearing component of bone (in the elastic region, it can be shown that $\sim 97\%$ of any applied load is supported by the hydroxyapatite) (Bonfield [1998], Bonfield et al. [1998]). Actually, collagen in bone is considered to provide a matrix in which the brittle ceramic solid HA is distributed. The values of Young's modulus increase with increasing HA volume fraction in bone (Bonfield et al. [1981], Bonfield et al. [1998]). This shows the importance of studying further the effect of HA and its constituents.

From the dietary point of view it is believed that both Calcium and Phosphorus are very important in bone health. They are thought to modify bone and are related to bone accretion and maintenance. Studies have found a positive correlation between bone density and Calcium intake during teenage years and early adulthood, in premenopausal women ranging in age from 20 to 50 years (Teegarden et al. [1998]). An increase in teenage Calcium intake from 800 to 1200 mg per day is estimated to increase hip bone density by 6% (Nieves et al. [1995]). Unlike dietary Calcium, the speculated role of dietary Phosphorus in limiting peak bone mass involves an excess intake of this nutrient. Consumption of a large excess of dietary Phosphorus, when Calcium intake is adequate or low, will lead to secondary hyperparathyroidism and progressive bone loss in a number of species.

The association of osteoporosis with hyperparathyroidism further supports the effect of Ca/P ratio on bone density. Hyperparathyroidism is the over-activity of the parathyroid glands, resulting in excess production of parathyroid hormone (PTH).

This is a hormone that regulates Calcium and Phosphate levels and helps to maintain them at suitable levels in the body. Excess parathyroid hormone (PTH) acts indirectly on osteoclasts whose activation ultimately leads to the removal of Calcium from the bones in order to increase its levels in the blood. Removing the offending parathyroid gland restores normal bone density within several years.

Calcium, Phosphorus and the ratio of the two elements was measured by Zaichick and Tzaphlidou [2002] in cortical bone using neutron activation analysis. A lower standard deviation and coefficient of variation were obtained for the Ca/P ratio than for Calcium and Phosphorus respectively, due to the strong correlation between Calcium and Phosphorus in bone. This correlation for healthy women and men aged 15-55 year was 0.823 ($p < 0.001$) and 0.747 ($p = 0.001$), respectively. If their healthy cortical bone contained only mineral, a strong molar dependence between Calcium and Phosphorus should exist, i.e. $\text{Ca} = 1.67\text{P}$, and the correlation coefficient would be 1.0. However, bone also consists of organic matter, and the concentration of Calcium and Phosphorus in organic matter is lower than in mineral and the Ca/P ratio different than in HA, the individual variation of the organic matter in cortical bone varies. This results in a decreased correlation between Calcium and Phosphorus in the whole cortical bone. The lower standard deviation and coefficient of variation show that the individual variation for Ca/P ratio in the cortical bone of femoral necks of healthy humans is lower than those for Calcium and Phosphorus separately, suggesting that the specificity of Ca/P ratio is better. The Ca/P ratio may be more reliable for diagnosis of bone disorders than the individual Calcium and Phosphorus concentrations.

A possible explanation of a lower Ca/P ratio is given by Zaichick and Zaichick [2010]. In that study it was found that Calcium, Phosphorus and Magnesium decrease significantly with age in the human femoral neck of males. In female femoral necks there is a decrease of Calcium and a smaller decrease of Phosphorus, leading to a lowered Ca/P ratio. A similar phenomenon might happen in osteoporosis.

Some *in vitro* imaging experiments have investigated the correlation of the Ca/P ratio to osteoporosis. Tzaphlidou et al. [2005] and Speller et al. [2005] measured Ca/P ratio using a synchrotron microCT system and directly mapped the linear attenuation coefficient to the Ca/P ratio. A statistically significant decrease was observed in rabbit tibia Ca/P ratio for inflammation mediated osteoporotic samples, when compared with controls. This suggests that there is a relationship between bone loss and lowered Ca/P ratio. Also, it was shown that normal bone shows less variation in the distribution of Ca/P ratio, as demonstrated by the absence of Ca/P ratio slice contours throughout the bone volume. On the other hand, osteoporotic examples showed a higher density of Ca/P ratio slice contours in general, but also displayed regions of significant Ca/P ratio gradient changes. An interesting observa-

tion was that a sample which was judged to be osteoporotic from the bulk estimate of the Ca/P ratio showed regions of osteoporotic behaviour and regions of normal behaviour, suggesting osteoporosis does not affect the whole of a cortical bone. More recent studies of the Ca/P ratio, using Auger electron and energy dispersive X-ray spectroscopy (Kourkouvelis et al. [2011]), show similar results.

Bone Calcium or Phosphorus was measured directly in vivo by neutron activation analysis, and such measurements were optimised for Calcium (Cohn et al. [1977]) or Phosphorus (Boddy and Glaros [1973]) independently. Also, a dual energy analysis model has been developed for the 2D quantification of Ca/P ratio in the proximal phalanx of the middle finger in vivo using a conventional X-ray source (Fountos et al. [1999]). When conducting measurements of bone, Ca, PO₄ and water can be regarded as the major attenuators of X-rays, given a number of assumptions. These include assuming that the organic material in the path of the photons has the same mass attenuation coefficient as that of water, and that by omitting O and H in the measured Ca/P ratio, the introduced error is trivial. By placing Cerium (Ce) and Samarium (Sm) filters in the X-ray beam, average photon energies of 39 and 89 keV can be obtained. Fountos et al. [1999] measured the Ca/P ratio of the right radius in 20 osteoporotic females aged 56-72 years. The diagnosis of osteoporosis was based on findings of compression fracture(s) of the spine and low BMD values obtained by conventional DEXA. A average Ca/P ratio of 1.29 was found for the osteoporotic females. This was significantly lower than that of 1.71 from 50 normal adult females, aged 26-68 years. Fountos et al. [1999] 's data though could not draw any conclusions on whether the observed difference in the average Ca/P ratio between postmenopausal osteoporotic patients and premenopausal controls is due to disease or related entirely to aging.

The same DEA model was used to analyse gamma ray absorptiometry rabbit, lamb and sheep tibia images. A significant decrease (p-value<0.01) in the tibia Ca/P ratio in animals with inflammation-mediated osteoporosis has been found compared to controls (Fountos [1997]). Furthermore, severe alterations were detected at the microstructural level on bone collagen fibrils, studied using electron microscopy, from inflammation-osteoporotic rabbits (Kounadi et al. [1998]).

All the above studies support the hypothesis that the Ca/P ratio affects bone quality and also that it can be used as an osteoporosis indicator. Understanding the effect of Ca/P ratio on bone quality and the effectiveness of the quantification of the Ca/P ratio in bone merits further investigation for the purposes of osteoporosis diagnosis.

1.4.3 The aim of this study

The studies described in section 1.4.2 were only conducted in 2D or have required the use of facilities not practically available for a clinical environment or long-term access, such as synchrotrons. The understanding, diagnosis and thus management of osteoporosis could be enhanced with 3D assessment of the Ca/P ratio. In a conventional CT scanner, direct mapping is not possible due to the polychromaticity of the beam. However, this problem can be overcome using a dual energy analysis (DEA) technique (section 2.4). In this thesis such a method is presented for 3D Ca/P ratio quantification that can be applied through a conventional CT scanner. A major advantage of the developed technique over previous techniques for Ca/P ratio assessment, is the simultaneous assessment of volumetric density (known to be correlated to bone mechanical properties) in bone.

The ideal case was to achieve a precision of better than 0.09 in the Ca/P ratio assessment, given that the min/max difference in Ca/P ratio between healthy and inflammation-mediated osteoporotic (IMO) bone samples is 0.09/0.43 (Tzaphlidou et al. [2005], Speller et al. [2005], Kourkoumelis et al. [2011]).

The development of this technique can potentially be used to investigate the effect of density and Ca/P ratio on bone quality *in vitro* or *in vivo*. This can be achieved by linking density and Ca/P ratio amount and distribution to bone mechanical properties. This can be achieved by bone mechanical compressions and/or FEA.

In addition, the development of this technique can potentially be used to enhance the prediction of bone fracture in osteoporosis. If the Ca/P ratio affects bone quality significantly, the assessment of 3D Ca/P ratio spatial distribution could potentially be used clinically to enhance the diagnosis, and thus prevention, of osteoporosis. It might be possible to detect a small change in the Ca/P ratio in bone before its BMD has significantly changed. Furthermore, the Ca/P ratio could provide additional information for the bone quality of some critical individuals whose BMD alone is not sufficient for an accurate prediction of bone fracture.

The development of CT-DEA for density and Ca/P ratio assessment in bone included the optimisation and the validation of the technique. Furthermore, the technique was applied to healthy and inflammation-mediated osteoporotic bone apatite samples to investigate the effect of the value and distribution of density and Ca/P ratio, in bone apatite, in osteoporosis. Similarly, CT-DEA was applied to healthy and inflammation-mediated osteoporotic intact (with collagen) bone samples to investigate the feasibility of the technique on bone samples with collagen, and the effect of the value of density and Ca/P ratio, in intact bone, in osteoporosis.

1.5 Structure of the rest of this thesis

In this chapter, the motivation for this work was explored. Osteoporosis and the importance of its early diagnosis were discussed, the current methods of osteoporosis diagnosis were explained and the approach of this study to the problem of osteoporosis was analysed.

The structure of the rest of the thesis is as follows:

- Chapter 2 describes the materials and methods used for the development, optimisation, validation and application of CT-DEA, including the microCT system, scanning electron microscopy system, DEA technique and bone phantoms and samples.
- Chapter 3 presents the optimisation performed to the technique, including the optimisation of the sample magnification parameter and the X-ray spectral pair.
- Chapter 4 describes the methodology and the results of the validation of the technique, in bone phantoms and bone samples (using a scanning electron microscope).
- Chapter 5 presents the results of the application of the technique on collagen-free healthy and inflammation-mediated osteoporotic bones samples.
- Chapter 6 presents the results of the application of the technique on intact healthy and inflammation-mediated osteoporotic bone samples.
- Chapter 7 summarises the work completed so far on CT-DEA and its application to bone samples, and discusses possible potential use of the technique for the improvement of the understanding and diagnosis of osteoporosis.

Chapter 2

Materials and Methods

2.1 Overview

This chapter describes the methods and materials used for the purposes of this study.

In section 2.2, the principles of a microCT system and its possible applications are explained, and the system used in this study, X-Tek benchtop microCT is described.

In section 2.3, the scanning electron microscope system, used for the evaluation of the performance of CT-DEA Ca/P ratio assessment in bone, is introduced and described.

In section 2.4, a brief historical background is given on the use of Dual Energy Analysis (DEA), with more emphasis on its use in bone decomposition. The theoretical framework of DEA and Computed-Tomography Dual Energy Analysis (CT-DEA) are described. Furthermore, different types of CT-DEA are explained. Two different CT-DEA mathematical algorithms are analysed for the assessment of density and Ca/P ratio: (i) applied to the mineral content of bone, *in vitro* for collagen-free bone samples (section 2.4.4); (ii) applied to intact (with collagen) bone, *in vitro* or *in vivo* (section 2.4.5).

In section 2.5.3, the bone phantoms and samples used for the validation of the developed technique (chapter 3) and the study of density and Ca/P ratio effect in osteoporosis, using collagen-free (chapter 4) and intact (chapter 5) bone samples are described.

2.2 Micro-computed tomography

2.2.1 X-ray interactions with matter

X-rays interact with matter in several different ways. Relevant to the diagnostic energy range (20-150 keV) are the photoelectric effect and Compton scattering.

These are briefly described below. More information can be found in Beutel et al. [2000].

In photoelectric interaction, the incident X-ray interacts with an electron in matter. The incident X-ray is completely absorbed, and all of its energy is transferred to the electron. The electron is then ejected from the atom, causing ionisation and excitation in the atom. There are two ways in which the relaxation of the atom can happen: (i) characteristic X-ray and (ii) a characteristic Auger electron. The energy of the X-ray or Auger electron is then the difference between the energies of the two excited states and this is characteristic of the particular atomic species. The dependence of photoelectric interaction probability, τ , (relevant to diagnostic energy range) on the effective atomic number, Z_{eff} and effective density ρ_{eff} of the material and the X-ray beam energy, E can be approximated as follows:

$$\tau \propto Z_{\text{eff}}^3 E^{-3} \rho_{\text{eff}} \quad (2.1)$$

In Compton scattering, an X-ray of energy greater than the binding energy of the atomic electron interacts with the atomic electron. A scattered electron and a scattered X-ray photon emerge, causing ionisation. The dependence of Compton interaction probability, σ , (relevant to diagnostic energy range) on the density, ρ_{eff} of the material can be approximated as follows:

$$\sigma \propto \rho_{\text{eff}} \quad (2.2)$$

The Compton scattering probability is almost independent of the atomic number Z_{eff} . At a given energy the probability of Compton interaction is effectively constant.

The probability, per cm thickness of matter, that an X-ray photon will be attenuated is described by the linear attenuation coefficient, $\mu(Z_{\text{eff}}, \rho_{\text{eff}}, E)$ in cm^{-1} . This is the sum of τ and σ (for the diagnostic energy range) and is thus energy and material dependent.

The mass attenuation coefficient, $m = \mu(Z_{\text{eff}}, \rho_{\text{eff}}, E)/\rho_{\text{eff}}$ of unit g/cm^2 is usually used to compensate for the dependency of $\mu(Z_{\text{eff}}, \rho_{\text{eff}}, E)$ on ρ_{eff} . Figure 2.1 shows the variation with energy of the mass attenuation coefficient for the two main constituents of bone: apatite (in the chemical form of hydroxyapatite) and collagen. The attenuation of hydroxyapatite is decomposed into the attenuation of its components: Ca, PO_4 , OH. The data for figure 2.1 was provided by XMuDat software (Nowotny [1998]).

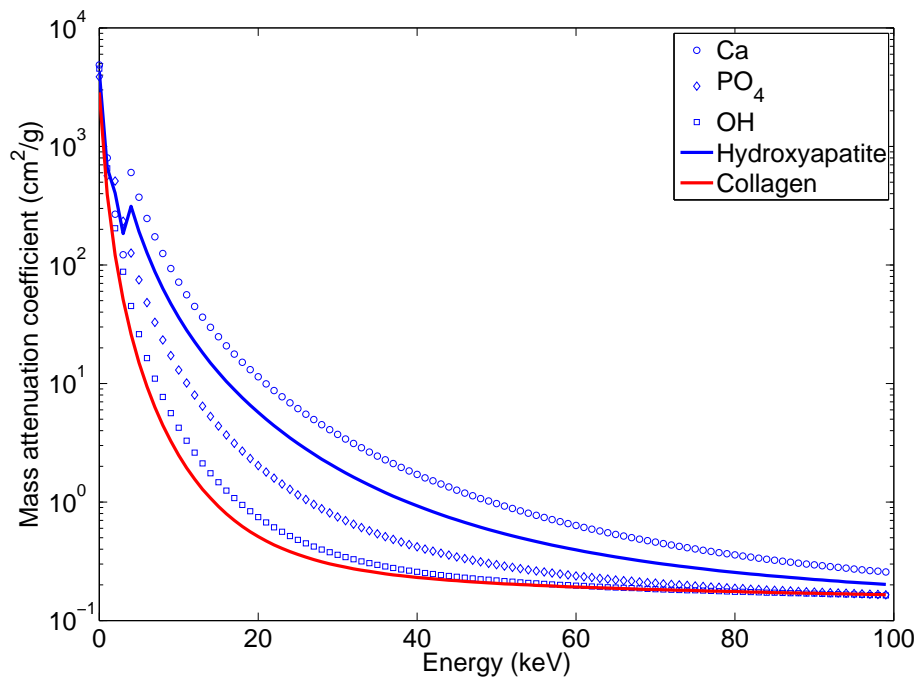


Figure 2.1: Variation of the mass attenuation coefficient with photon energy for the two main bone components: apatite in the chemical form of hydroxyapatite (blue line) and collagen (red line). The attenuation of hydroxyapatite is decomposed into the attenuation of its components: Ca (circles), PO_4 (diamonds), OH (squares).

2.2.2 Principles of computed tomography

In a CT system, X-rays are produced in an X-ray tube, which consists of an oil-filled housing containing an evacuated envelope of heat-resistant glass, within which are mounted a filament (cathode) and an anode. An electric current heats the filament, which then fires accelerated electrons, in a narrow beam, that finally strikes the anode. The electrons interact with the material of the anode, in which they release heat and 1% of X-rays in a beam. The X-ray beam is then attenuated by the sample (as described in section 2.2.1) and at the end it reaches the image receptor, which forms an image by the absorption of energy from the X-ray beam.

Computed tomography (CT) is the term that characterises the imaging technique in which transmission measurements of a narrow beam are made at several different angles (projections) around an object. Then these measurements are used to re-synthesise (or reconstruct) slices ('tomos') within the object.

A 2D map of X-ray attenuation is produced for each 2D slice of the subject, thus there is no compression of 3D data into a 2D plane. This is the advantage of CT over planar radiography, where many anatomical planes or slices may be considered superimposed upon each other, which can distract the viewer from a small lesion or fracture.

Various types of CT systems have been developed so far. Their differences are

mainly different combinations of motion(s), geometric design and detector types. The first generation used a single scanning beam and a single detector. The beam was first translated across the object, before rotating 1 degree before repeating the process. The second generation systems used several detectors, instead of one, like in first generation, monitoring a single X-ray source with a limited fan X-ray beam. The third generation system used a fan-beam geometry and a large number of detectors designed to rotate in synchronisation with the X-ray tube moving in single continuous rotational motion. The difference in the fourth generation was that there were several hundred detectors, which were kept fixed on a stationary ring and the X-ray source only moved. More details about each CT generation can be found in Beutel et al. [2000] and Webb [1988].

Nowadays, third- and fourth- generation geometry achieve full 360 degrees rotations in 1 second or less, therefore reducing patient motion problems. The slice thickness reduction since the original CT is 13 000 μm to 500 μm .

The reconstruction of slices is achieved by reconstruction algorithms. The projection tells you that the beam was attenuated somewhere along the path, but has no information about where. This averages you can smear the projection out with equal probability all along the ray path. This is back-projection. Back-projection though suffers from blurring. The X-rays passing through the diameter of a homogeneously solid cylindrical object in a CT system will be attenuated most, while the X-rays grazing the edges of the cylinder will be attenuated least. There will be blurring around the edges as the signal strength varies inversely with the radial coordinate in the image space. This is known as the star effect. This problem is overcome by filtering the profiles by a Kernel filter (a function that has negative side lobes) before back-projecting them.

An alternative reconstruction method is the iterative technique. In this, the projection image profiles are acquired, back-projected, and then successively modified until the modified data are consistent to within pre-defined limits of all their X-ray profiles. Successive approximations and changes are made after each iteration to make the profile converge to a solution.

The product of the reconstruction algorithms are the CT images, expressed in Hounsfield or CT numbers (in each voxel; the volume element represented by pixel size \times pixel size \times slice thickness), which is a function of the linear attenuation coefficient, $\mu(Z_{\text{eff}}, \rho_{\text{eff}}, E)$ is expressed as follows:

$$CT_i = 1000 \frac{\bar{\mu}(E, \rho_i, Z_{\text{eff}}) - \bar{\mu}(E, \rho_{\text{water}}, Z_{\text{water}})}{\bar{\mu}(E, \rho_{\text{water}}, Z_{\text{water}})} \quad (2.3)$$

where i represents the attenuating material.

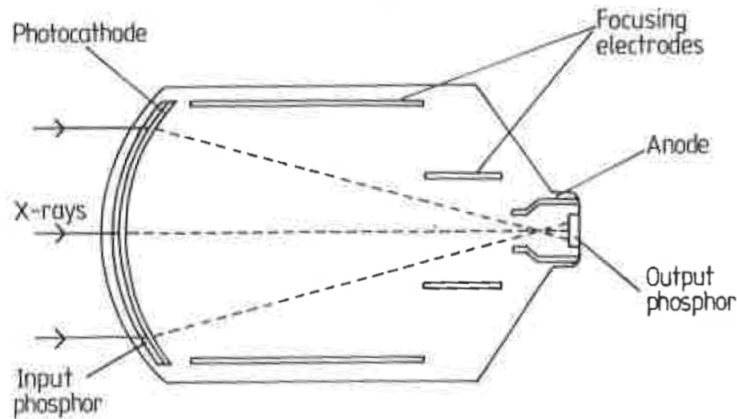


Figure 2.2: Construction of an image intensifier (Webb [1988]).

2.2.3 X-Tek benchtop micro-computed tomography system

X-ray micro-tomography is a miniaturised version of computerised tomography, the main difference being its smaller focal spot (a few μm) providing a resolution of the order of μm . This makes its use common in the study of trabecular and cortical architecture in humans (Majumdar [2008], Martn-Badosa et al. [2003], Nuzzo et al. [2003]), rats (Laib et al. [2000]) and mice (Martn-Badosa et al. [2003]). Other applications of the microCT in bone studies include the prediction of bone mechanical properties either by correlating microCT bone density and porosity measurements to bone stress, stiffness and Young's modulus (Wachter et al. [2001]) or by generating micromechanical models of the scanned sample by converting bone voxels to mechanical elements that can be analysed by the FEA method (van Der Linden et al. [2001], Shefelbine et al. [2005]).

For the purposes of this study a bench-top cone-beam microCT system (Nikon Metrology, X-Tek, United Kingdom); serial number: J00001, was used (figure 2.3). The device is equipped with a microfocus X-ray tube, of $12 \mu\text{m}$ focal spot size in an energy range from 0 up to 125 kVp, and a maximum current of $500 \mu\text{A}$.

The detector is a high resolution image intensifier, a high-gain device for imaging X-rays. It consists of an evacuated tube, with two intensifying screens, a photocathode and electron optics (figure 2.2). The X-rays pass through the entry window, strike the fluorescent screen, situated on the inner surface of the window, from where light fluorescent photons are emitted. These hit the photocathode, where photoelectrons are emitted. The electrons are accelerated through a potential difference, guided by electron optics, and strike an exit fluorescence screen, in order to produce further fluorescent photons. These are viewed by a charged-coupled device (CCD) camera. The field of view of the entry window is $160 \text{ mm} \times 160 \text{ mm}$ field of view and the pixel size is $170 \mu\text{m}$.

The effective resolution of the system, is dependent on sample magnification

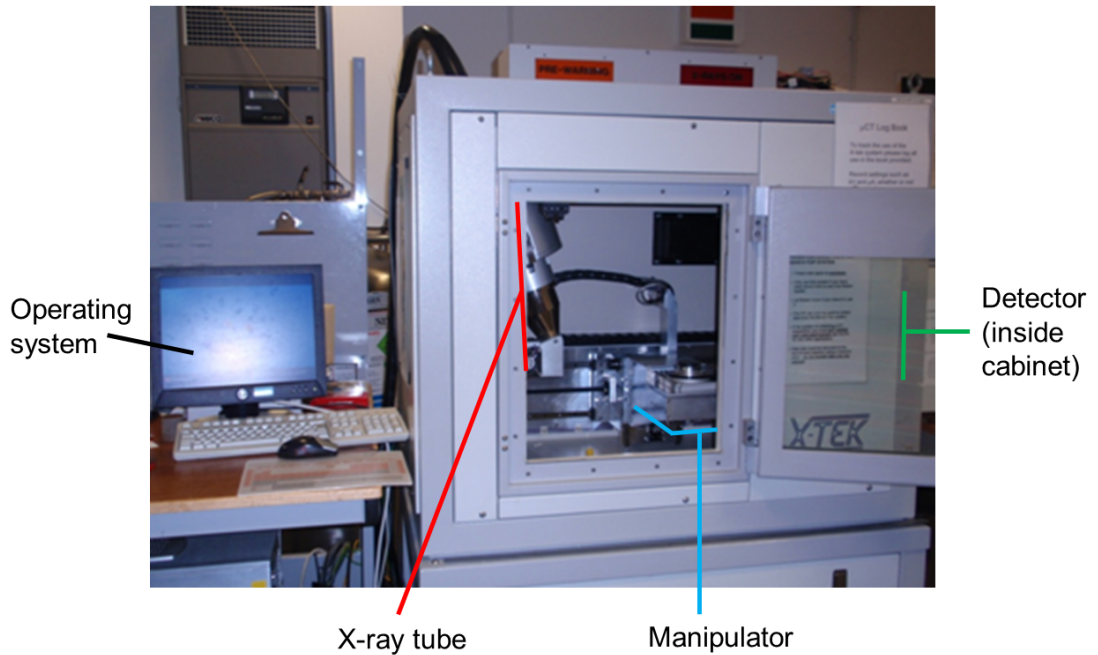


Figure 2.3: The X-Tek microCT system.

parameter. This is discussed in section 3.2. The source to detector distance is fixed (682 mm). In imaging, the samples are positioned onto the manipulator (a turn-up table) of the instrument (figure 2.3). CT image reconstruction was performed on the images using the in-built, filtered back-projection X-Tek software (Nikon Metrology, X-Tek, United Kingdom).

2.3 Scanning electron microscope

The scanning electron microscope (SEM) uses a focused beam of electrons to produce signals at the surface of solid samples. The interaction of electrons with the sample produces information about surface topography and chemical composition, and crystalline structure and orientation of materials making up the sample.

In most applications, data are collected over a selected area of the surface of the samples and a 2D image is generated that displays spatial variations in these properties, revealing details of less than 1 nm in size. It is impossible to produce the overall analysis of the whole sample without damaging it.

SEM was used in this study to determine the composition of regions of interest in the surface of eight (four healthy and four IMO) rabbit tibia cortical bone samples (section 2.5.3). Using the composition results, the Ca/P ratios of these areas were calculated and were compared to the Ca/P ratios of the same areas found using CT-DEA (section 4.4). In this section, a brief overview is made on how the SEM system works.

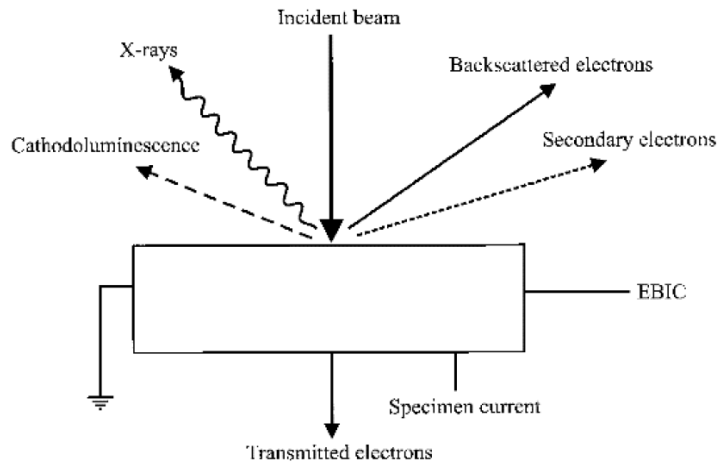


Figure 2.4: Some of the signals which can be used in an SEM system (Goodhew et al. [2001]).

2.3.1 Electrons interaction with matter

Electrons interact elastically or inelastically with matter. Elastic scattering does not change the energy of the primary electron, but might change its direction. Elastically scattered electrons produce a diffraction pattern (spatial distribution of the scattered electrons) from which a great deal of information about the arrangement of the atoms in the sample can be deduced. Diffraction patterns were not of use in this study, therefore elastic scattering will not be discussed further.

In inelastic scattering the primary electron loses a detectable amount of its kinetic energy, which ends up as heat in the sample or as secondary effects; the emission of secondary electrons, backscattered electrons and X-rays. All these end up being very useful for both imaging and analysis in SEM (figure 2.4).

In this study, backscatter imaging was used in SEM to acquire images of the samples. Backscattered electrons are primary electrons that leave the surface before giving up all their energy after inelastic collisions. The number of backscattered electrons emitted from the sample for each incident electron varies monotonically with atomic number. Using SEM images the composition of the sample was produced and the areas of compositional interest were identified by backscattered imaging and the phase compositions were then determined by analysis of the X-ray signal.

Phase composition is achieved using the relaxation of excited atoms in the sample, when a localised electron is knocked out of an atom. The two ways in which the relaxation of the atom can happen are the same as in the case of X-ray interaction with matter: (i) characteristic X-ray and (iii) a characteristic Auger electron. The energy of the X-ray is then the difference between the energies of the two excited states and this is characteristic of the particular atomic species. Therefore, information on the elements present and their amount can be retrieved. Further information

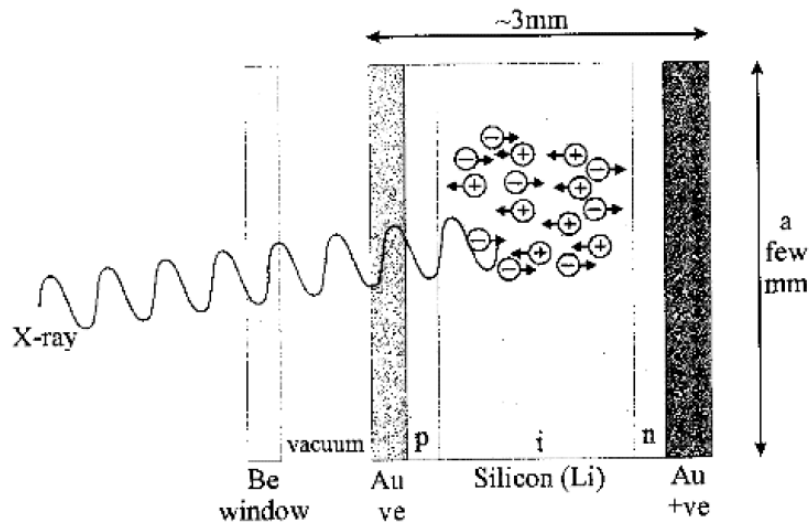


Figure 2.6: Parts of an energy dispersive spectrometer (Goodhew et al. [2001]).

which is reverse biased, using thin layers of gold on both surfaces of the detector. The gold coated outer surface is protected from contamination by a thin window of beryllium or a polymer. The whole detector is cooled at liquid nitrogen temperature ($-196\text{ }^{\circ}\text{C}$) to preserve the detector crystal and to reduce noise in the system.

Each incoming X-ray excites a number of electrons into the conduction band of the silicon leaving the same number of positively charged holes in the outer electron shells. The energy required for each of these excitations is only 3.8 eV ; consequently the number of electron-hole pairs generated is proportional to the energy of the X-ray photon being detected. If a voltage is applied across the semiconductor a current will flow as each X-ray is absorbed in the detector and the magnitude of the current will be proportional to the energy of the X-ray. It is impracticable to detect X-rays of energy less than 1 keV with this type of detector; therefore all elements lighter than sodium are eliminated. Finally, a multichannel analyser (MCA) is used to register the current (pulse) into different channels, and produce a histogram (spectrum).

In the SEM system it is necessary for the surface of the sample to be electrically conducting. During operation there is a surplus of electrons building up on the sample surface. Therefore electrons have to be conducted away to earth to prevent the sample surface from becoming negatively charged and the incoming primary electrons to be repelled and deviated from their normal path. There is no difficulty in studying clean metal samples. However, usually non-conductors such as biological materials present a problem. In this case it is usual to coat the sample with a thin (about 10 nm) conducting layer of gold or carbon. Coating was not required in this study, since collagen was removed from the bone samples (section 2.5.3), thus they only contained minerals which are ionising. Furthermore, the sample should ideally be flat, since on rough samples some X-rays might not reach the detector due to

scatter.

2.4 Dual energy analysis

2.4.1 Historical background of dual energy analysis in bone decomposition

Interest in decomposing bone components using DEA has existed since the early 1960s. In 1963, Cameron and Sorenson proposed a 2D DEA model for finding the concentrations of the elements present in bone, with projection radiography (Cameron and Sorenson [1963]). The model was tested with radioactive sources (Iodine-125 at 27.3 keV and Americium 241 at 59.6 keV) on blocks of paraffin and Calcium Carbonate (CaCO_3), homogeneously mixed in known proportions. The measurements resulted in determination of the percentage of CaCO_3 over a wide range of compositions, to an average accuracy of 3%. Their model however was never tested experimentally with X-rays and/or on bone phantoms/samples, for its potential clinical application.

In 1976, CT-DEA was first conceived. In the late 1970s and 1980s, a large amount of work was completed on the techniques and clinical applications of material decomposition imaging with CT-DEA (Alvarez and Macovski [1976], Kelcz et al. [1979], Chapman et al. [1980], Lehmann et al. [1981], Goldberg and Cann [1982] and Kalender et al. [1986]). Attempts were made to quantify the amount of the mineral content in bone using CT-DEA. Burgess [1987] assessed the mineral content of human vertebral trabecular bone using CT-DEA, with a correlation of 95% to the actual mineral content of the samples (Burgess [1987]).

In 1997, Fountos developed a new DEA system and model to assess, quantitatively, the amount of Ca/P ratio in animal and human bone in 2D, using radioactive sources (Fountos [1997]) and a commercial X-ray source (Fountos et al. [1999]).

Limitations in generator powers, tube heat capacity, tube cooling, and spatial and temporal resolution of earlier X-ray imaging systems put a limit to the potential of the DEA in clinical applications. Today, the main success of DEA is bone mineral density quantification. To the best of the knowledge of the author, there have not been any new results on bone elemental mineral decomposition using DEA since 1999.

However, interest in bone composition and especially the study of the Ca/P ratio still exists today. Other techniques, including neutron activation analysis (Zaichick and Tzaphlidou [2002]), synchrotron linear attenuation coefficient mapping (Tzaphlidou et al. [2005], Tzaphlidou et al. [2006], Speller et al. [2005], Postnov et al.

[2003]), SEM (Kourkouvelis et al. [2011], Kourkouvelis et al. [2011]), the study of human diet (Teegarden et al. [1998]), as discussed in section 1.4.2 have been used to determine the importance of Calcium and Phosphorus and/or Ca/P ratio in osteoporosis understanding and diagnosis. All the above studies have shown that research on the Calcium/Phosphorus in bone, and its relation to bone quality are justified.

Recently, CT (Wang et al. [2008]) and CT-DEA have regained focus in terms of both basic technology and new potential clinical applications, some of which are the quantification of iron in a fatty liver (Liu et al. [2009]), the quantification of iron in arteries for identifying vulnerable plaque (Wang et al. [2011]), the determination of urinary stone composition, the quantification of renal masses, urolithiasis and disorders of uroepithelium (Hartman et al. [2012]) and angiography (Watanabe et al. [2009]). Further clinical potential applications of CT-DEA are described by Karçaaltıncaba and Akta [2011]. However, no work has been completed before, on the use of CT-DEA for Ca/P ratio assessment.

2.4.2 Principles of dual energy analysis technique

DEA imaging involves the acquisition of images acquired at two different X-ray beam energies: one at a low-kVp and another at a high-kVp. Quantification of a defined set of material components can be achieved by appropriate processing of the pair of images. For example, in an X-ray image consisting of bone and soft-tissue, eliminating bone yields an image and quantification of soft-tissue, and vice versa. Figure 2.7 shows a typical case of DEA. The information from the two images acquired at the two different energies is decomposed into their component materials using the energy-dependent differences in their attenuation coefficients.

It is possible to conduct dual energy within a single exposure (SE) technique (Stewart and Huang [1990]). In the SE the X-ray detector is made of two layers, separated by a filter. Each layer is responsive to a different energy to allow simultaneous acquisition of two images of the same sample.

The conventional DEA technique involves a successive voltage change of the X-ray beam during the image acquisition process. This method is more efficient in terms of energy separation, and showed great increase in accuracy in the calculation of the measured quantity, compared with SE (Burgess [1987], Genant and Boyd [1977]). However, it assumes that the object is static during the acquisition of the two images. For the purposes of this study the DEA technique was used due to the single layer detector of the microCT system.

There are several models of DEA. The best choice of DEA model depends on the specific application of the considered problem. The ρZ decomposition method (Alvarez and Macovski [1976]) can be used to identify the materials present in the

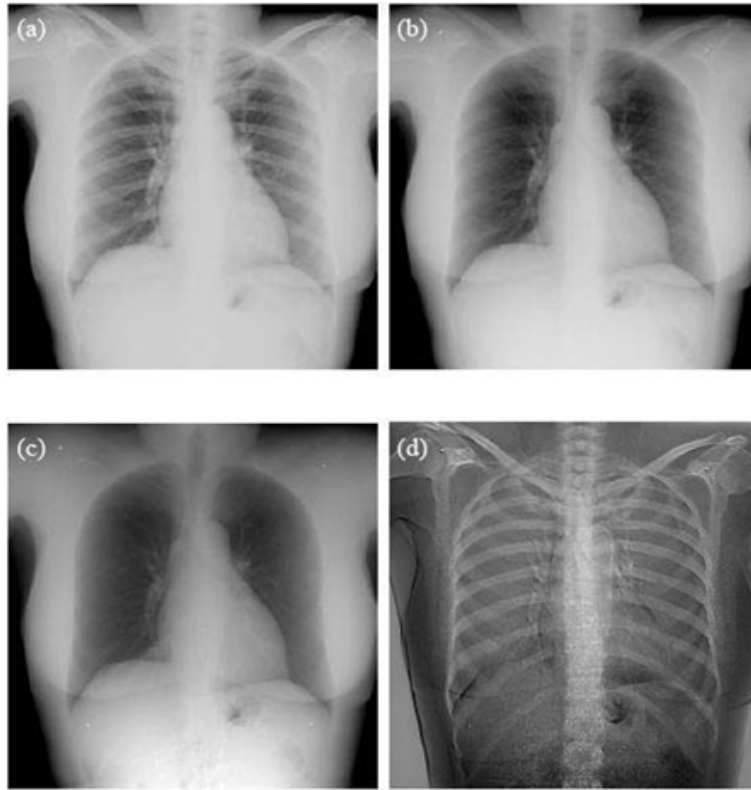


Figure 2.7: Dual energy imaging of the chest. (a) Low kVp and (b) High kVp images are decomposed into (c) soft tissue and (d) bone images (Toutountzis [2009]).

sample, and produce a material specific image. The two photon-matter interactions of the diagnostic energy range, the photoelectric effect and Compton scattering interactions, and their relative contribution to the total attenuation are energy dependent. The contribution of effective density and effective atomic number of the material to each type of X-ray interaction is known. Therefore, acquiring images at two different energies, and separating the two X-ray interactions, provides information for the effective density and effective atomic number of the sample.

Alternatively, the basis material decomposition method (Lehmann et al. [1981], Kalender et al. [1986], Arvanitis and Speller [2009]) is a technique that can be used to quantify the amount of a known component (its thickness or its concentration) present in a sample. Any material's mass attenuation coefficient, excluding K-edges, can be expressed as a linear combination of the attenuation coefficients of its components. This technique decomposes the image of a sample into two components by linearly combining the images acquired at the two different energies.

2.4.3 Computed tomography dual energy analysis (CT-DEA)

As for planar DEA, there are different ways of CT-DEA. The ρZ method and the basis-material decomposition method are the two main methods. The basic equations used in them are mathematically described below.

As mentioned above, in the ρZ method, the photoelectric effect and Compton scattering interaction effect are separated thus allowing determination of density and Z_{eff} . For the CT ρZ method the line integral over the linear attenuation coefficient of a CT measurement is given by

$$\int \mu(r, E) ds = \alpha \int \rho_{\text{eff}} \frac{Z_{\text{eff}}^k}{E^n} ds + \beta \int \rho_{\text{eff}} \phi_{KN}(E) ds \quad (2.4)$$

where ϕ_{KN} is the Klein-Nishina function, $k \approx 3-4$ and $n \approx 3-3.5$, and α and β are constants (Cho et al. [1975]).

In the basis material decomposition method the attenuation of the known sample components are separated and the amount of each material is quantified. The line integral over the linear attenuation coefficient of a CT measurement is given by

$$\int \mu(r, E) ds = \int \rho_{\text{eff}} f_1 m_1(r, E) ds + \int \rho_{\text{eff}} f_2 m_2(r, E) ds \quad (2.5)$$

where $\mu(r, E)$ is the local linear attenuation coefficient, f_1 and f_2 are the mass fractions of basis materials 1 and 2, and $m_1(r, E)$ and $m_2(r, E)$ are the mass attenuation coefficients of basis materials 1 and 2, respectively.

Both the ρZ and the basis material decomposition methods described above can be implemented either in pre-reconstruction space and post-reconstruction space. The advantage of the pre-reconstruction implementation is that raw data can be preprocessed, for example to correct for beam hardening. The advantage of a post-reconstruction implementation is its relatively ease of implementation and fast execution time.

Examples of pre-reconstruction implementations include Alvarez and Mackovski's (Alvarez and Macovski [1976]) ρZ method (Lehmann et al. [1981]) and Kalender's (Kalender et al. [1986]) basis material decomposition method. In 2003, Heismann et al implemented their ρZ method in post-reconstruction space (Heismann et al. [2003]). Liu et al described the implementation of a general material basis method in post-reconstruction space (Liu et al. [2009]). Table 2.1 summarises the currently known main DEA methods.

Liu et al. [2009]'s method was experimentally validated using a dual-source CT system and phantoms containing mixtures of water, hydroxyapatite and aqueous iron nitrate solutions. The advantage of this method in clinical situations is that it can determine the effective density, the effective atomic number and the mass fraction of two materials of a mixture using two image acquisitions.

The method quantifies the effective density of the mixture and the fractions of the sample components, from the same dual-energy CT images, in two steps. The first step is a post-reconstruction ρZ approach, and therefore determines the Z_{eff} and ρ_{eff}

2. Density and Ca/P ratio assessment using CT-DEA

Table 2.1: Summary of the studies of the main CT-DEA material decomposition algorithms.

Reconstruction Method	DEA approach	
	ρZ	Material basis
Prereconstruction	Alvarez and Mackovski (Alvarez and Macovski [1976])	Lehmann et al (Lehmann et al. [1981]) Kalender et al (Kalender et al. [1986])
Postreconstruction	Heismann et al (Heismann et al. [2003])	Liu et al (Liu et al. [2009])

of the sample. The second step, is a post-reconstruction material decomposition approach. The ρ_{eff} result produced in step one is used as known information in step two to obtain the fractions of the sample components. This approach is semi-analytical as it requires prior-knowledge of the sample components and an approximation of how a change in the component proportion affects X-ray attenuation.

A basis material decomposition method, similar to the one introduced by Liu et al. [2009], was used in this study and adapted for bone mineral decomposition. The Z_{eff} , ρ_{eff} of bone apatite and intact bone and the proportions of Calcium and Phosphorus are quantified in the two-step process.

2.4.4 CT-DEA for density and Ca/P ratio assessment in bone mineral content

In principle, CT-DEA cannot decompose more than two constituent materials in a mixture because it only provides two independent measurements. Bone is a complex structure, consisting of more than two components. Three of the main components in bone apatite, Ca, PO_4 and OH, are at the same time the three main X-ray attenuators in bone apatite. The rest of the elements in bone apatite are of reduced quantity, therefore their effect in X-ray attenuation is insignificant (Fountos [1997]) and bone apatite can be decomposed into these three components only.

For a three-material decomposition using two different spectral measurements, one additional condition must be provided to solve for three unknowns. One possible solution is the assumption of volume conservation in the mixture or sample, i.e. to assume that the sum of the volumes of three constituent materials is equivalent to the volume of the mixture (Burgess [1987]). However, this assumption is not always true. For example, the volume of a salt-water mixture is not equal to the sum of the individual volumes of salt and water. Instead, mass conservation can be assumed. This is based on the same principle i.e. to assume that the sum of the masses of three constituent materials is equivalent to the total mass of the mixture.

Two spectral measurements and a mass-conservation based, 3-material decom-

position CT-DEA algorithm were used to determine the material density of bone apatite ($BMD_{material}$, as defined in section 1.4.1) and the proportions of the three main components in bone apatite: Ca, PO_4 and OH (figure 2.1). This algorithm is mathematically described below.

Assuming a 100% efficient detector, the average linear attenuation coefficient, $\bar{\mu}$, is expressed by:

$$\bar{\mu}(Z_{\text{eff}}, \rho_{\text{eff}}, E) = \bar{m}(Z_{\text{eff}}, E)\rho_{\text{eff}} \quad (2.6)$$

where as defined above, E is energy and ρ_{eff} , Z_{eff} and \bar{m} are the effective density, effective atomic number and average mass attenuation coefficient of the sample, respectively. If the X-ray spectrum is known, the average mass attenuation coefficient \bar{m} can be calculated as:

$$\bar{m} = \frac{\int P(E).E.m(E).dE}{\int P(E).E.dE} \quad (2.7)$$

where P is the number of photons. At low (E_L) and a high (E_H) energies,

$$\bar{\mu}_L(Z_{\text{eff}}, \rho_{\text{eff}}, E_L) = \bar{m}_L(E_L, Z_{\text{eff}})\rho_{\text{eff}} \quad (2.8)$$

$$\bar{\mu}_H(Z_{\text{eff}}, \rho_{\text{eff}}, E_H) = \bar{m}_H(E_H, Z_{\text{eff}})\rho_{\text{eff}}. \quad (2.9)$$

The ratio of these two gives the fraction of the average linear attenuation coefficients, at the low and high energy, which will be referred to in the remainder of this study as ‘F’:

$$\frac{\bar{\mu}_L}{\bar{\mu}_H} = \frac{\bar{m}_L}{\bar{m}_H} = F(Z_{\text{eff}}). \quad (2.10)$$

For two particular spectra, the theoretical values of $\bar{m}_L(Z_{\text{eff}})$, $\bar{m}_H(Z_{\text{eff}})$ and $F(Z_{\text{eff}})$ can be calculated for a specific Z_{eff} . Therefore, based on the ratio of the effective linear attenuation coefficients, $F(Z_{\text{eff}})$, obtained from the CT image data, Z_{eff} , $\bar{m}_L(Z_{\text{eff}})$ and the effective density, ρ_{eff} of the sample can be determined (using equation 2.6).

Liu et al. [2009] constructed a numerical lookup table for the theoretical values of $\bar{m}_L(Z_{\text{eff}})$, $\bar{m}_H(Z_{\text{eff}})$ and $F(Z_{\text{eff}})$ (Liu et al. [2009]). All previous work has used the lookup table approach.

In this study, $\bar{m}_L(Z_{\text{eff}})$ was determined in two steps using mathematical relations of $F(Z_{\text{eff}})$ to Z_{eff} and Z_{eff} to \bar{m}_L . At present, these approximations of the mathematical relations are required in CT-DEA for bone material decomposition. This

2. Density and Ca/P ratio assessment using CT-DEA

is because the exact chemical composition of biological apatite is diverse and not known with sufficient accuracy to enable the construction of a precise look-up table of $F(Z_{\text{eff}})$ to Z_{eff} and Z_{eff} to \bar{m}_L .

These relations (figure 2.8) were approximated by second order polynomials (with $R^2 = 0.99$ each), using the chemical formulae of bone apatite phantoms of different Ca/P ratio (table 2.2) and the XMuDat software (Nowotny [1998]). The resulting relation of $F(Z_{\text{eff}})$ to Z_{eff} is

$$Z_{\text{eff}} = 0.3169F^2 - 1.4382F + 5.9591; R^2 = 0.99 \quad (2.11)$$

and of Z_{eff} to \bar{m}_L is

$$\bar{m}_L = 0.0138Z^2 - 0.2140Z + 1.231; R^2 = 0.99 \quad (2.12)$$

There is nothing physical to suggest what order of the polynomial is correct, therefore ideally the one that best gives the best fit to the data (the highest order polynomial) should have been chosen. However, the advantage of an approximated second order polynomial for $F(Z_{\text{eff}})$ to Z_{eff} and Z_{eff} to \bar{m}_L relations, compared to a higher order polynomial, is that for the second order polynomial there is a smaller error of propagation from $F(Z_{\text{eff}})$ to Z_{eff} to \bar{m}_L and finally to the assessed quantities (ρ_{eff} and Ca/P ratio). In this study, an order of polynomial higher than the second order propagated a significantly high error in the assessed quantities.

After determining ρ_{eff} using the knowledge of \bar{m}_L , found using the $F(Z_{\text{eff}})$ to Z_{eff} and Z_{eff} to \bar{m}_L mathematical relations, the fractions of the sample components can be quantified. Assuming that Ca, PO_4 and OH are the only components in bone apatite (equation 2.13), the fractions of Ca, PO_4 and OH can be determined by solving equations 2.13 - 2.15 below.

$$1 = f_{\text{Ca}} + f_{\text{PO}_4} + f_{\text{OH}} \quad (2.13)$$

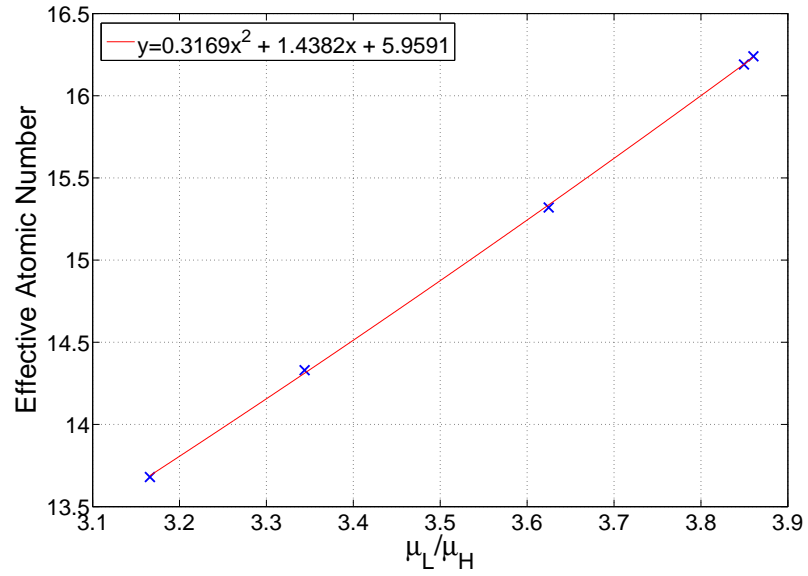
where f_i is the fraction by weight of each component i .

At the low, L, and high, H, energies the average linear attenuation coefficient, $\bar{\mu}_L$, H can be expressed by:

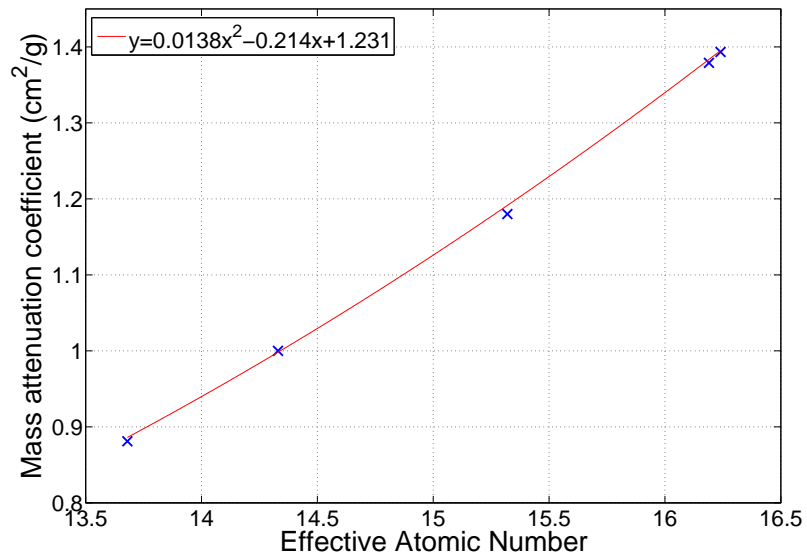
$$\frac{\bar{\mu}_L}{\rho_{\text{eff}}} = \bar{m}_{\text{Ca},L} f_{\text{Ca}} + \bar{m}_{\text{PO}_4,L} f_{\text{PO}_4} + \bar{m}_{\text{OH},L} f_{\text{OH}} \quad (2.14)$$

$$\frac{\bar{\mu}_H}{\rho_{\text{eff}}} = \bar{m}_{\text{Ca},H} f_{\text{Ca}} + \bar{m}_{\text{PO}_4,H} f_{\text{PO}_4} + \bar{m}_{\text{OH},H} f_{\text{OH}} \quad (2.15)$$

Finally, knowing f_{Ca} , f_{PO_4} and f_{OH} allows the Ca/P ratio to be calculated. The molecular weight ratio (PO_4/P) is 3.0679, and the ratio of the molar masses of Ca



(a)



(b)

Figure 2.8: Relations of (a) $F(Z_{\text{eff}})$ to Z_{eff} and (b) Z_{eff} to \bar{m}_L for bone mineral content composites of different Ca/P ratio.

and P is 1.2940, thus the atomic Ca/P ratio is given by:

$$\text{Ca/P ratio} = \frac{f_{Ca}}{f_{PO_4}} \frac{3.0679}{1.2940}. \quad (2.16)$$

The above algorithm was custom-built in MATLAB for the purposes of this study.

2.4.5 CT-DEA for density and Ca/P ratio assessment in intact bone

As shown in table 1.1, in addition to bone apatite, intact (with collagen) bone also contains mainly collagen. For the *in vivo* use of the technique, the presence of collagen also needs to be taken into account, due to its significant weight proportion ($\geq 15\%$ by weight) in bone.

However, using two energy beams the maximum number of sample constituents to be decomposed are three. The proportion of collagen is bigger than the proportion of OH in bone. Therefore, the third component of the mineral content of bone, OH, is replaced by collagen for intact bone.

As above, two spectral measurements and a mass-conservation based, three-material decomposition CT-DEA algorithm can be used to determine the proportions of Ca, PO₄ and collagen in intact bone.

The mathematical relations of $F(Z_{\text{eff}})$ to Z_{eff} and Z_{eff} to \bar{m}_L (figure 2.9), were approximated as above by different second order polynomials (with $R^2 = 0.99$ each), using the chemical formulae of the bone phantoms (table 2.2) and assuming collagen is also present in them in a weight proportion of 15%. The resulting relations are the following:

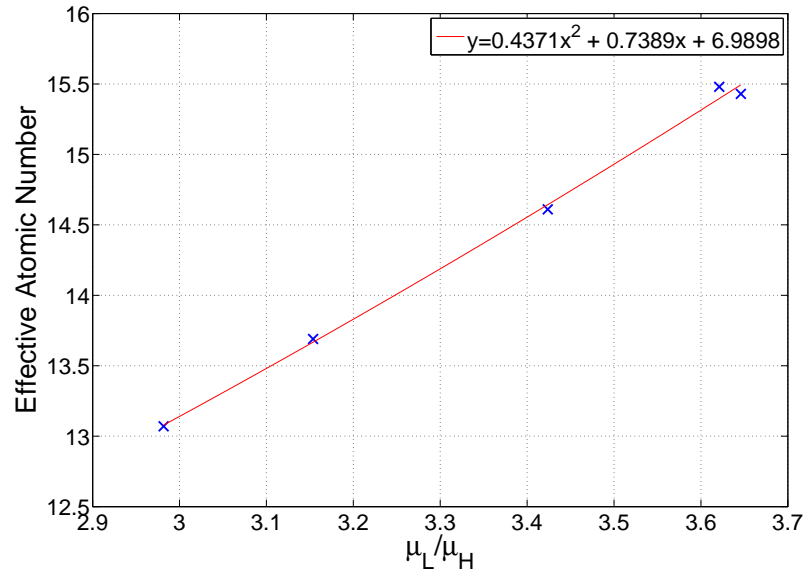
$$Z_{\text{eff}} = 0.4371x^2 - 0.7389x + 6.9898; R^2 = 0.99 \quad (2.17)$$

and for the low energy image the calibration equation is

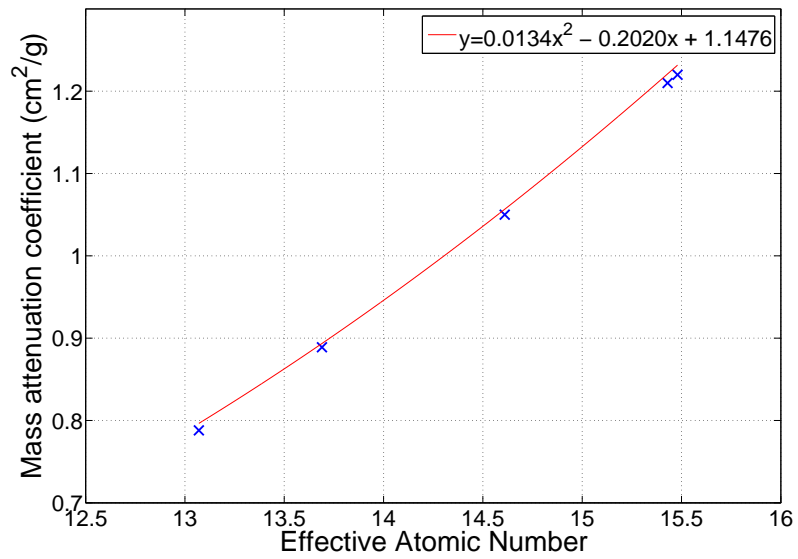
$$\bar{m}_L = 0.0134x^2 - 0.2020x + 1.1476; R^2 = 0.99 \quad (2.18)$$

ρ_{eff} can be determined using equation 2.13. Assuming that Ca, PO₄ and collagen are the only components in bone (equation 2.19), the fractions of Ca, PO₄ and collagen can be determined by solving equations 2.19 - 2.21 below.

$$1 = f_{Ca} + f_{PO_4} + f_{coll} \quad (2.19)$$



(a)



(b)

Figure 2.9: Relations of (a) $F(Z_{\text{eff}})$ to Z_{eff} and (b) Z_{eff} to \bar{m}_L for bone composites (85% mineral and 15% collagen by weight) of different Ca/P ratio.

where f_i is the fraction by weight of each component i .

$$\frac{\bar{\mu}_L}{\rho_{\text{eff}}} = \bar{m}_{Ca,L} f_{Ca} + \bar{m}_{PO_4,L} f_{PO_4} + \bar{m}_{coll,L} f_{coll} \quad (2.20)$$

$$\frac{\bar{\mu}_H}{\rho_{\text{eff}}} = \bar{m}_{Ca,H} f_{Ca} + \bar{m}_{PO_4,H} f_{PO_4} + \bar{m}_{coll,H} f_{coll} \quad (2.21)$$

Finally, the atomic Ca/P ratio is given by equation 2.16, as above.

The above algorithm was custom-built in MATLAB for the purposes of this study.

2.5 Samples

2.5.1 Di-potassium phosphate solutions

Di-Potassium Phosphate, K_2HPO_4 , has similar attenuation to bone apatite (Genant and Boyd [1977]) ($\bar{\mu}_{K_2HPO_4,L} = 2.50$, $\bar{\mu}_{HA,L} = 2.32$ and $\bar{\mu}_{K_2HPO_4,H} = 0.78$, $\bar{\mu}_{HA,H} = 0.64$). Five K_2HPO_4 solutions of different concentration (1-5 g/cm³) were prepared using de-ionised water and K_2HPO_4 powder (Sigma-Aldrich Ltd). These solution were used in the calibration of the CT grey value of the microCT system (section 3.6.2) and in the evaluation of the experimental precision of density of CT-DEA (section 4.3).

2.5.2 Bone phantoms

For the evaluation of the precision CT-DEA in density and Ca/P ratio assessment in bone apatite, ten bone phantoms of known Ca/P ratio were used. Commercially available Calcium Phosphate powder (Sigma-Aldrich Ltd), of five different chemical formulae, was compressed using a Specac hydraulic presser into small cylindrical pellets (of 8 mm diameter and 2-4 mm height) of different density_{total} (being equivalent to the mass over the total volume of the sample, not the mass over the volume of the material) (figure 2.10). Some of the samples had the same chemical formula, and thus the same Ca/P ratio. The reason they were all assessed was to test repeatability in Ca/P ratio assessment, when density_{total} is different, and thus $\mu(Z_{\text{eff}}, \rho_{\text{eff}}, E)$ is different. Table 2.2 shows details for the phantoms, including their purity, as provided by Sigma-Aldrich Ltd.

For the determination of the total density of a phantom its mass was measured using a weighting scale and its volume was found using the microCT image of the phantom (after thresholding, as will be discussed in section 4.3). For the determination of the Ca/P ratio of a phantom its chemical formula was used.



Figure 2.10: Typical bone phantoms.

Table 2.2: Details of phantoms used in CT-DEA precision evaluation.

Chemical Formula	Purity	Ca/P ratio	Density _{total}	CT-DEA decomposition
$\text{Ca}(\text{H}_2\text{PO}_4)_2(\text{H}_2\text{O})$	> 85.0%	0.5	2.54	Ca, PO4, H ₂ O
$\text{Ca}(\text{H}_2\text{PO}_4)_2(\text{H}_2\text{O})$	> 85.0%	0.5	2.39	Ca, PO4, H ₂ O
CaHPO_4	98.0%	1	2.97	Ca, PO4, H
$\text{CaHPO}_4 \cdot 2\text{H}_2\text{O}$	98.0%	1	2.95	Ca, PO4, H ₂ O
$\text{CaHPO}_4 \cdot 2\text{H}_2\text{O}$	98.0%	1	2.81	Ca, PO4, H ₂ O
$\text{Ca}_3(\text{PO}_4)_2$	96.0%	1.5	2.10	Ca, PO4
$\text{Ca}_3(\text{PO}_4)_2$	96.0%	1.5	2.21	Ca, PO4
$\text{Ca}_5\text{OH}(\text{PO}_4)_3$	99.9%	1.67	2.08	Ca, PO4, OH
$\text{Ca}_5\text{OH}(\text{PO}_4)_3$	99.9%	1.67	2.27	Ca, PO4, OH
$\text{Ca}_5\text{OH}(\text{PO}_4)_3$	99.9%	1.67	1.81	Ca, PO4, OH

2.5.3 Bone samples

Healthy and inflammation-mediated osteoporotic bone samples were used to: (i) evaluate the performance of CT-DEA on Ca/P ratio assessment in real bone apatite, using collagen-free bone samples (section 4.4), (ii) study the effect of density and Ca/P ratio on osteoporosis in bone apatite, using collagen-free bone samples (chapter 4), and intact bone (chapter 5).

Bone samples were obtained from the same animal species, female New Zealand white rabbits. For the purposes of this study 12 rabbits were housed in groups of two and were bred in natural conditions, allowed to freely take a diet of solids and tap water. Throughout the animal experiments, which were performed at Ioannina University, care was taken to minimise pain and discomfort. All study protocols were approved by the Ioannina University Institutional Animal Care and Use Committee.

In half of the animals, inflammation-mediated osteoporosis (IMO) was induced. The first animal model of generalised osteoporosis resulting from inflammation that closely resembled the chronic inflammatory bone loss seen in human patients was developed by Minne et al. [1984] in the rat. It is one of the five manipulations that have been used in experimental animals to induce excessive bone loss in order to produce a model for osteoporosis, since no mammalian species, other than humans, fractures when it loses bone. The other mechanisms are the immobilisation by plaster casting, nerve, or tendon sectioning leads to severe bone loss, ovariectomy induced bone loss and various dietary manipulations (Grynpas [1993]).

2. Density and Ca/P ratio assessment using CT-DEA

In IMO, the inflammation in the animals is provoked by injections of nonspecific irritants such as cotton wool or talkum (magnesium silicate solution of density 1 gram magnesium silicate per 2.5 grams physiologic saline), typically on the back of the rat at sites distant from the skeleton, to stimulate an acute phase response (Armour and Armour [2003]). In this study, the IMO model was applied using talkum (Sigma-Aldrich Ltd) on the rabbits. More details for the induction of IMO to the animals can be found in the protocol document of the model (Armour and Armour [2003]).

Very few attempts have been made to verify that in these models the bone that remained was indeed more fragile (Grynpas [1993]). However IMO bones have been used several times as representatives of osteoporotic bones and the results were characteristic of osteoporosis. Minne et al. [1984] observed a decrease in trabecular bone volume of the tibia in IMO rats of about 30%. Granulomatous reactions were noticed at the injection sites along with the accumulation of chronic inflammatory cells. In addition, significant decreases in osteoblast number and trabecular volume were observed at bone sites away from the inflammatory lesion. These are major features of inflammation-mediated osteoporosis (Pfeilschifter et al. [1987], Vukicevic et al. [1988], Krempien et al. [1988]). In rats, decreases in osteoprogenitor (cells from which osteoblasts arise) number and bone elongation were also found (Krempien et al. [1988]). Osteoclast numbers and osteoclastic resorption were found to be generally unchanged (or transiently decreased) in this model (Minne et al. [1984], Pfeilschifter et al. [1987], Vukicevic et al. [1988], Krempien et al. [1988]). This is in agreement with the observations in humans with chronic nonosseous inflammation (Ralston et al. [1990], Deodhar and Woolf [1996]).

Furthermore, a statistically significant decrease in Ca/P ratio in inflammation-mediated osteoporosis treated rabbit bones (Fountos [1997]) and aged/osteoporotic human bone (Fountos et al. [1999]) compared to healthy bone was reported. Similar results were found by Speller et al. [2005], Tzaphlidou et al. [2005] and Kourkoumelis et al. [2011]. Kounadi et al. [1998] results also showed an anarchic arrangement of rabbit bone fibrils and a disrupted architecture in IMO rabbits compared to control rabbits. Moreover, the diameters of the fibrils from treated rabbits varied, in contrast to the uniform size of normal ones.

All animals were euthanised under light ether anesthesia at 8 months of age. Titanium and glass tools were used to clean samples of soft tissues and blood. A titanium scalpel was used to cut cortical bone samples into 4-10 mm lengths. Cortical sections of all samples from the diaphysis of the bones were dissected and cleaned free of muscles and tendons (figure 2.11). No signs of metabolic alterations of the bone tissues were noted.

From each animal, sections were cut from three different bone sites of the rabbits;



Figure 2.11: A typical bone sample.

rear tibia (RT), front tibia (FT) and femur (F), giving 36 samples in total (table 2.3). Eighteen of the samples were heated at 350 °C for 48 hours to remove collagen (Miculescu and Ciocan [2011], Raspanti et al. [1994]), to limit any error its presence might introduce on the outcome of CT-DEA on bone apatite. After heating, the shape of the bone samples was preserved. As shown by Raspanti et al. [1994]), heat treatment at below 500 °C has no detectable effect on the size, crystallinity, or lattice spacing of the crystals of bone apatite while at the same time it effectively removes most of the organic part.

Table 2.3: Numbers of bone samples for each bone type and each bone site.

Bone Site	Collagen-free		Intact	
	Healthy	IMO	Healthy	IMO
RT	3	3	3	3
F	3	3	3	3
FT	3	3	3	3

The usage of the 36 bone samples is discussed in table 2.4. For the evaluation of the performance CT-DEA technique on real bone samples, collagen-free bone samples were used to limit any problems its presence might introduce in the SEM imaging, due to the non-conducting nature of collagen. Since for SEM imaging bone samples with flat and parallel surfaces are required, the eight (four healthy and four IMO) most parallel and flat-surfaced collagen-free samples (set 1a; part of set 1) were selected. The samples were carefully polished using a polishing paper of grit size $58.5 \pm 2 \mu\text{m}$, to make the surface even more flat and parallel. A diamond wheel saw could have been used instead; however, due to the high fragility of the collagen-free samples it was avoided.

Eighteen collagen-free bone samples (set 1) were used to study density and Ca/P ratio in bone apatite. Nine of them were healthy and nine of them IMO; three rear tibiae, three femurs and three front tibiae for each bone type. The exact analysis performed and the results of the study of set 1 are discussed in chapter 5.

Similarly, eighteen intact (nine healthy and nine IMO; three rear tibiae, three femurs and three front tibiae for each type) bone samples (set 2) were used to study density and Ca/P ratio in intact bone. Details on the analysis performed and the

results of the study of set 2 are discussed in chapter 6.

Table 2.4: Bone samples sets and usage.

Set	Samples number		Type	Usage
	Healthy	IMO		
1a	4	4	Collagen-free	Evaluation of CT-DEA on bone apatite
1	9	9	Collagen-free	Analysis of density and Ca/P ratio in bone apatite
1	9	9	Intact	Analysis of density and Ca/P ratio in intact bone

2.6 Summary

In this chapter the imaging system used for the application of CT-DEA in this study, X-Tek benchtop microCT, and for the evaluation of the precision in Ca/P ratio assessment by CT-DEA, SEM, were described. Two different CT-DEA mathematical algorithms were analysed for the assessment of density and Ca/P ratio: (i) applied to the mineral content of bone, *in vitro* for collagen-free bone samples (section 2.4.4); (ii) applied to intact bone, *in vitro* or *in vivo* (section 2.4.5). Finally, the preparation of the bone phantoms and samples used for the validation of the developed technique (chapter 3) and the study of Ca/P ratio effect in osteoporosis, using collagen-free (chapter 4) and intact (chapter 5) bone samples was described.

Chapter 3

CT-DEA optimisation

3.1 Overview

In this chapter the optimum conditions selected for the production of the density and Ca/P ratio bone results, in sufficient precision and resolution, are described.

In section 3.2, the method and the results of the optimisation of the magnification parameter, so that CT-DEA results are produced with sufficient resolution, are described.

In section 3.3, the method and the results of the selection of the energy spectral pair, so that CT-DEA results are produced with sufficient precision, are described.

3.2 Optimisation of the magnification parameter

An ‘optimum sample position’ in an imaging system is defined as the position of the sample along the line from the X-ray tube to the detector where the achieved resolution is at its maximum. For the developed technique to be potentially applied to trabecular bone, a minimum resolution of 150 μm is required, since, according to Ulrich et al. [1999], Majumdar et al. [1997] and Laib et al. [1997] the trabecular thickness varies between 150-500 μm . The corresponding sample position and magnification to achieve this resolution needed to be found.

A framework for the optimisation of the geometry of the system, accounting for the effects of both the focal spot and the detector, determined simultaneously from one set of measurements, was developed and applied to the microCT system to find the optimum sample position.

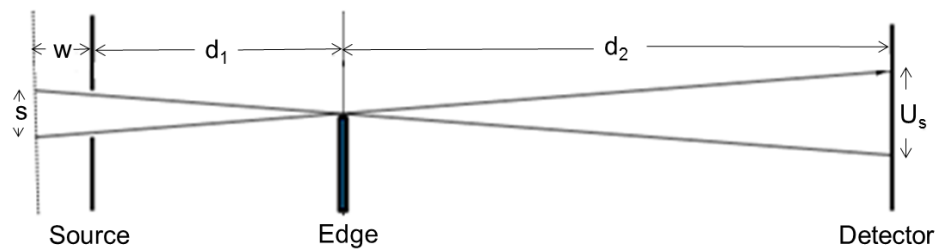


Figure 3.1: The geometric blurring or penumbra, U_f due to the focal spot.

3.2.1 Unsharpness

Unsharpness refers to the degree of blurring among the boundaries between different regions of the image. The components of an imaging system that contribute to unsharpness are the focal spot of X-ray tube, the detector and the sample/patient movement. In microCT *in vitro* experiments there is not any movement unsharpness, thus overall unsharpness in the image, U , is given by the sum of squares method (Webb [1988]).

$$U = \sqrt{U_s^2 + U_d^2} \quad (3.1)$$

where U_s is the geometric blurring or penumbra and U_d is the intrinsic detector resolution.

U_s , the geometric blurring (or penumbra), is caused by the finite area of the focal spot; the region of an X-ray tube from which the X-rays emanate. More precisely, the spatial distribution of the focal spot caused by electrons impinging onto the surface of the target. This can be kept to a minimum by employing a tube with a small focal spot. This requires the use of a small filament (producing the electrons) and a small area over which the electrons hit the target. However, the filament size cannot be too small as it may overheat and melt; and the area is restricted by the ability to keep the target cool.

The geometrical unsharpness is also dependent on the ratio of sample-detector distance, d_2 , to source-sample distance, d_1 (figure 3.1),

$$U_s = s \frac{d_2}{d_1 + w} = s.m \quad (3.2)$$

In the detector, the X-ray photons exiting the sample do not necessarily interact at the same point at which they enter the detector. The particles that form the image may spread inside the detector and be recorded at a distance from the interaction site. This is known as the intrinsic detector resolution or unsharpness, U_d .

For an object that is imaged under magnification the effect of the detector on unsharpness gets bigger with smaller magnification. This is because more pixels fit into the object when it is magnified. Thus, the further away the object is from the detector, the smaller the unsharpness due to the detector. But, then, the closer the object to the source the bigger is the geometric unsharpness. A compromise between the distance from the source and the distance from the detector has to be made to find the optimum sample position.

Therefore, the magnification, M (achieved using the conventional X-ray cone-beam), is expressed by:

$$M = \frac{d_1 + w + d_2}{d_1}. \quad (3.3)$$

Equation 3.1 can then be expressed as:

$$U = \sqrt{\frac{(s.m)^2}{M^2} + \frac{D^2}{M^2}} \quad (3.4)$$

or,

$$U = \sqrt{\frac{(s.(M-1))^2}{M^2} + \frac{D^2}{M^2}} \quad (3.5)$$

By demanding $\frac{dU}{dM} = 0$ the optimal magnification and thus the optimal position can be found (Gayer et al. [1990]).

3.2.2 Edge imaging

The common methods to determine the total, geometric or detector resolution are the slit and the edge methods (Beutel et al. [2000], Fujita et al. [1992], Samei et al. [1998]). The slit method assesses the response of the system to an impulse function by imaging a slit that represents a delta function. The response of the system, Line Spread Function (LSF) is thus given by the convolution of the Point Spread Function (PSF) with the slit. The edge method uses an edge and the pixel value versus distance from the edge is plotted to form the Edge Response Function (ERF).

One of the advantages of the edge method is its simplicity and easy access to an edge. Comparing the edge and slit methods, the edge method requires a much lower level of exposure for sufficient irradiation of the detector and it theoretically requires less precise alignment (Samei et al. [1998]). Also, for a system with an expected high resolution, very small slits are required, placing great demands on fabrication and alignment.

Several alternatives have been suggested for the quantification of unsharpness. The overall width of the LSF; which is the derivative of the ERF, could be used but in many cases it has no definite width. The FWHM of the LSF provides a good practical measure of the unsharpness especially when the LSF has a Gaussian form (Kandarakis [2001]). Unsharpness has also been defined as the distance over which the response goes from 16.5% to 83.5% of the maximum (Shuping and Judy [1978]). Additionally, the MTF, the Fourier transformed LSF, a typical method of describing resolution gives an indication of unsharpness at some specified spatial frequency (Day [1976], Lubberts and Rossmann [1967], Rossmann [1964]). This method of measuring the MTF has gained popularity recently, due to its simplicity and appropriateness especially for imaging (Cunningham and Reid [1992], Samei et al. [1998]).

In this study the edge method was used to quantify the total unsharpness and to separate the contributions of the focal spot and the detector. The edge unsharpness was quantified as the FWHM of the LSF of the edge. To find the unsharpness due the edge, it was required to acquire images of the edge, determine the orientation of the edge, apply appropriate sampling of the pixel data and process the resulting edge response function (ERF) to obtain the LSF.

As an edge, the International Electrochemical Commission (IEC) recommends using a 4 mm thick test object consisting of 1 mm of tungsten and 3 mm of lead. Several authors though have used test objects completely made of lead, completely opaque to X-rays (Koutaloni et al. [2008]). Blurring of the ERF obtained is thus kept to a minimum. However, complete opacity leads to the reduction of quantum noise in one tail of the ERF relative to that in the other. On the other hand, too high a transmission results in an unacceptably small signal to noise ratio. In this experiment a semi-opaque (transition measured to be about 50%), uniform density, 0.1 mm metallic titanium sharp edge was thus used.

The titanium edge was positioned parallel to the X-ray tube window surface and the detector, and its edge was imaged. Usually, the orientation of the edge is determined with the help of a laser beam (Samei et al. [1998]), but this was technically difficult to use within the microCT. Therefore, a titanium object whose top and bottom edges were sharp, straight and parallel, was tightly fixed in a holder. The holder was positioned parallel to the X-ray window surface by carefully measuring the distances from different places across it to the edge using a micrometer. The angle of misalignment, θ , of edge surface was later calculated using the image as 0.83 degrees. This was determined by finding the distances at which there is the maximum point of the line spread function at the two sites of the image, and subtracting these distances to find q (figure 3.2). The value of p was also calculated from the image and trigonometry was used to calculate θ .

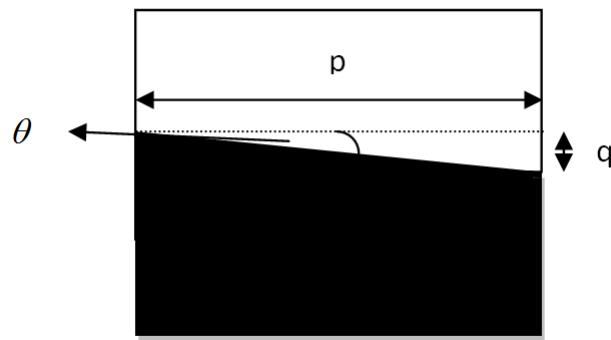


Figure 3.2: Method of calculation of the angle of missalignment θ .

For the acquisition of the edge images the microCT system tungsten source was operated at 55 kVp and 55 μ A. Images of the edge were captured at 26 different positions in a range of 0.60 mm to 130 mm from the X-ray tube window. For each position four images were captured. Distance and magnification of the edge in each position, were calculated using the manipulator position value, as given by Inspect X software.

The exact position of the focal spot within the X-ray tube was not known. The distance between the focal spot and the tube window, w (figure 3.1), could create a large error in focal spot calculation if not taken into consideration, especially when the edge was near the source. Calculation of w could not be conducted within the microCT because of practical limitations. Therefore, an isolated X-ray source (identical to the one in the microCT system) was used. It consisted of the electron drift tube, the target and the window assembly. A laser beam was passed through the path where the electrons normally pass, and a spot of light was produced at the same height on the target where the electrons normally hit. Knowing this point it was possible to measure using a micrometer the distance w and consider it in the calculation of the position and magnification. The distance from the focal spot to the window of the source, w was measured as 5.3 ± 0.7 mm.

3.2.3 Unsharpness analysis

Custom-built MATLAB codes processed images to extract the results. Flat-field corrections were applied to all of the images. Subtraction of the dark image (background) allows for correction of spatial inhomogeneities of the detector, while dividing by the white data allows for corrections of the spatial inhomogeneities of the X-ray beam. Flat fielding is expressed by the equation below (Moy et al. [1999]).

$$Image = \frac{Raw - Dark}{White - Dark} \quad (3.6)$$

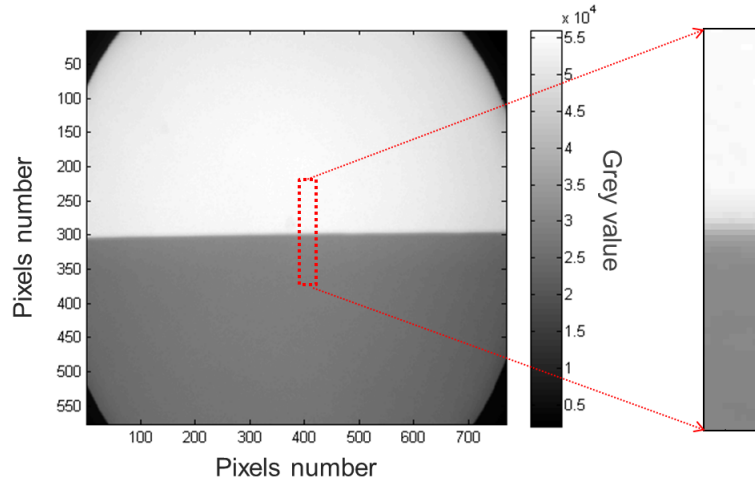


Figure 3.3: (a) The edge image at a magnification of 6. The selected area shows the area of interest ($20 \times \text{pixels} \times 150 \text{ pixels}$) used for the production of the ERF, and in (b) the magnified area of interest, showing the blurring at the edge.

The width of the area of interest in the edge images was selected to be 20 pixels in the middle of the image, in order to avoid the error in the misalignment of the edge. The length of the area of interest was chosen as 150 pixels so that it covers all the unsharpness area.

The grey value of the pixels for each of the 20 perpendicular lines in the area of interest was plotted versus the length of the area of interest for the formation of the ERF. The 20 ERFs were then averaged together. The length measurements given from this image in pixels were converted to mm using the measured detector pixel pitch ($168 \mu\text{m}$). Differentiating the ERF produced the LSF (figure 3.4) whose FWHM was used to define the unsharpness. The FWHM at each position was the average of the four FWHMs measured from the four images at that position.

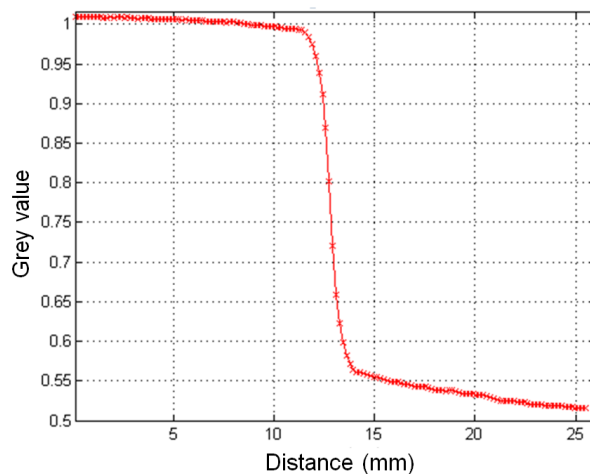
The quantified unsharpness due to the edge, U_e , at a position is given by the sum of the geometric unsharpness at that position and the intrinsic detector resolution (Shuping and Judy [1978]).

$$U_e = \sqrt{(s.m)^2 + U_d^2} \quad (3.7)$$

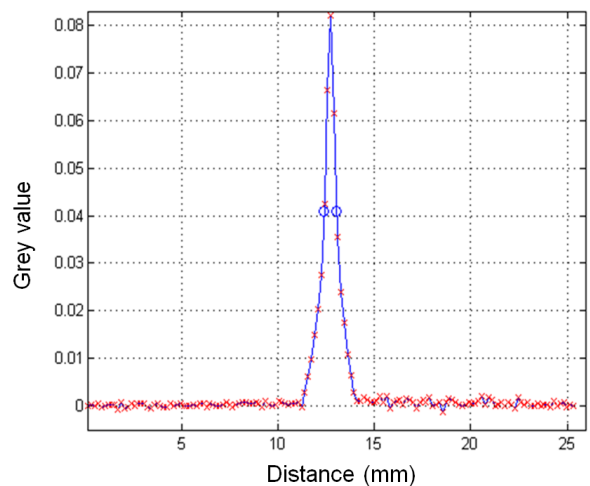
where all symbols have been defined previously.

Each FWHM was plotted versus the corresponding $\frac{d_2}{d_1}$ value. The chi-square, χ^2 , (equation 3.8), is usually used to define the agreement between the experimental and expected distributions (Taylor [1997]). It was used in reverse in this study to find the best or expected fit of (equation 3.7) on the plot of FWHM versus $\frac{d_2}{d_1}$.

$$\chi^2 = \sum_1^n \frac{FWHM - \sqrt{(s.m)^2 + U_d^2}}{\sigma_n^2}; n = 26 \quad (3.8)$$



(a)



(b)

Figure 3.4: (a) The profile of the edge object ERF. (b) Following differentiation, the LSF and thus the FWHM (given by the open circle points) can be found.

where σ_n is the standard deviation of the observed FWHM and n is the number of measurements (i.e. the number of positions at which the edge was imaged).

A MATLAB code was developed that fitted equation 3.8 with different values of s (between 1-100 μm) and U_d (between 100-900 μm), and for each combination the χ^2 factor was calculated. The combination of s and U_d that resulted in the minimum value of χ^2 and thus the minimum variation between the experimental and expected distribution, are the actual real s and U_d of the microCT system.

The intrinsic detector resolution was also quantified using the MTF to confirm the results of the χ^2 test. A direct measurement of the intrinsic detector resolution U_d can be made by imaging an object of very small thickness which is touching the detector, thus having magnification equal to one. The LSF was Fourier transformed to find the MTF that characterises the detector (Price et al. [2008]). The MTF was fitted to a Gaussian curve, resulting in a coefficient of determination R^2 of 99%.

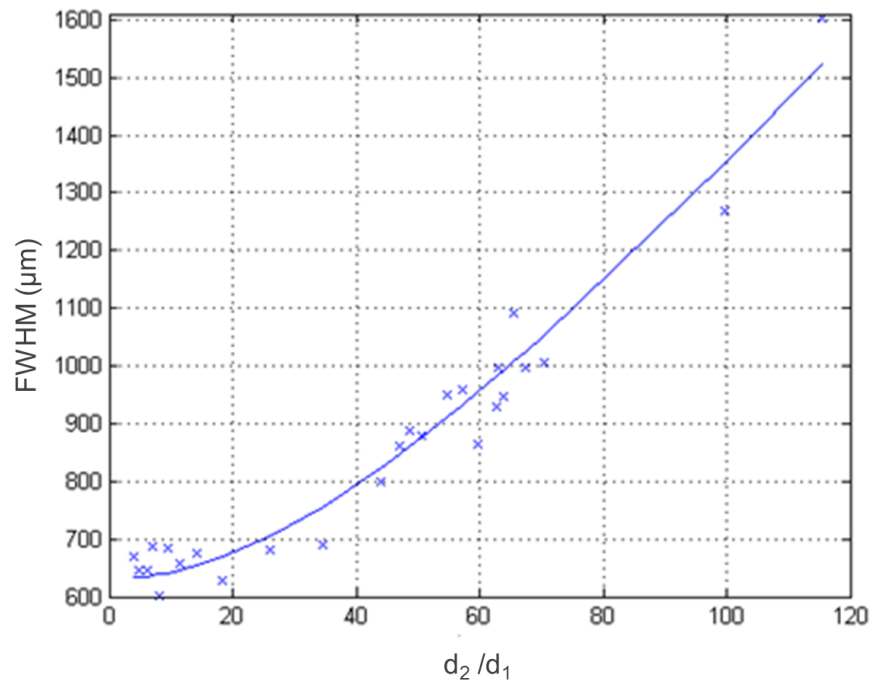


Figure 3.5: FWHM versus $\frac{d_2}{d_1}$. The crosses represent the measured FWHM values of the LSF of the edge, while the smooth line shows the fitting of equation 3.7 ($f = 12 \mu\text{m}$ and $U_d = 630 \mu\text{m}$, calculated using the χ^2 test) through these points.

Conventionally, the value of the spatial frequency which corresponds to an MTF of 0.1 is defined as the spatial resolution (Kandarakis [2001]). Some writers use the values which correspond to MTFs of 0.01-0.05 (Koutalonis et al. [2008]), but for the purpose of this study the threshold was considered 0.1.

Finally, using the values found for the focal spot size and the intrinsic detector resolution the total unsharpness of an object under magnification in our system was calculated using equation 3.4. A graph of total unsharpness, U , versus magnification, M , was plotted and the value of M which corresponds to the minimum total unsharpness is the optimum magnification, giving the optimum sample position in the microCT system.

3.2.4 Results: optimum sample magnification

The results of the edge unsharpness (FWHM) versus $\frac{d_2}{d_1}$ are represented in figure 3.5 by crosses. At small $\frac{d_2}{d_1}$ values (1 to 20) the unsharpness results are approximately constant due to the small effect of geometric unsharpness near the detector. Thus it can be concluded that U_d is around $630 \mu\text{m}$. As expected, as magnification value increases the FWHM increases too because the effect of the focal spot increases.

The smooth line in figure 3.5 shows the fitting of equation 3.7, with $s = 12 \mu\text{m}$ and $U_d = 630 \mu\text{m}$, through the points. In order to fit equation 3.7 through the points, the values of the intrinsic detector resolution (U_d) and of the focal spot

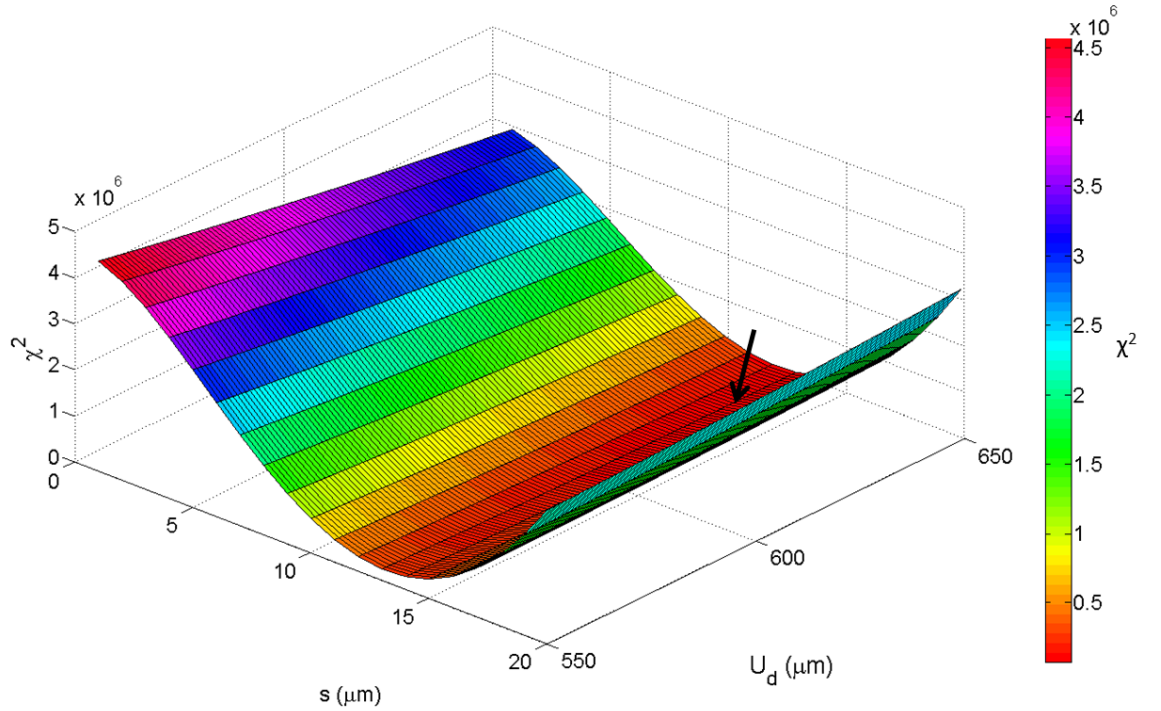


Figure 3.6: Plot of χ^2 value versus focal spot size versus intrinsic detector resolution. The black arrow represents the minimum χ^2 value which indicates the focal spot size and intrinsic detector resolution values that provide the best fitting of (equation 3.7), to the measured results of unsharpness (FWHM).

size (s) had to be found. These were determined by inputting different values of s and U_d in equation 3.7, until it best fitted through the points. A line that best satisfies equation 3.7, and takes into account the measured unsharpness results in all positions was produced using the χ^2 factor. Figure 3.6 shows the results of the χ^2 test for s being in the range of 1-20 μm and U_d in the range of 550-650 μm .

The focal spot size found ($s = 12 \mu\text{m}$) is an acceptable value for a microCT system (expected value was about 15 μm). Any uncertainty in the value of focal spot size suggests that there might be a systematic error in d_1 , d_2 or w measurements. It was technically difficult to accurately measure w because of its very small dimensions and the finite diameter of the spot of the laser beam produced on the target of the X-ray source.

The intrinsic detector resolution result ($U_d = 630 \mu\text{m}$), agrees to 3.2% with the direct measurement of the intrinsic detector resolution, 620 μm , given by the MTF. This validates the results given by the χ^2 test. The MTF of the detector, is shown in figure 3.7.

The propagation of $\frac{d_2}{d_1}$ error on focal spot and detector resolution calculation was analysed. Error in $\frac{d_2}{d_1}$ derived from errors in $d_2 + d_1$ (fixed X-ray source to detector distance), w and d_1 . A combination of these errors concluded in the error in $\frac{d_2}{d_1}$ for

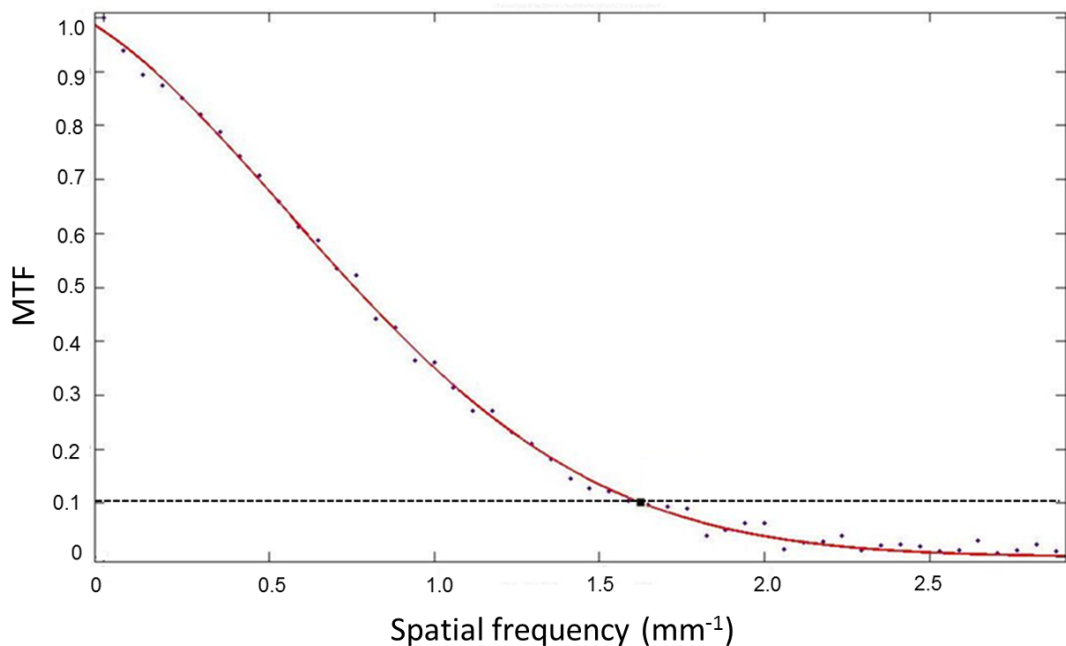


Figure 3.7: Detector MTF. The spatial frequency value which corresponds to 0.1 (dotted line) of the response of the detector represents the intrinsic detector resolution.

each position of the object. So, using again the χ^2 test it was found that taking into account the maximum $\frac{d\mu}{d_1}$ error the focal spot changed only by 1 μm and the detector unsharpness by 7 μm .

The total unsharpness, calculated using equation 3.5, was decoupled into focal spot and detector unsharpness versus magnification, M . This is shown in figure 3.8. Using this plot, the optimum position of a sample in the microCT system under magnification was defined. A magnification higher than 4.1 (corresponding to a source window-sample distance, d_1 of 161 mm) gives an effective system resolution higher than 150 μm . This is sufficient to visualise the trabecular network and to quantify morphological parameters (Ulrich et al. [1999]). An example of a microCT image of trabecular bone, acquired $M = 10$ (i.e. effective system resolution is 63 μm), is shown in figure 3.9.

3.2.5 Conclusions on the optimum magnification parameter

The χ^2 test successfully allowed for the development of a framework for the simultaneous calculation of the focal spot size ($s = 12 \pm 1 \mu\text{m}$) and intrinsic detector resolution ($U_d = 630 \pm 7 \mu\text{m}$). The result of U_d has been confirmed using the MTF of the detector resolution.

It has to be noted here though that this is the optimum position only at 55 kV and 55 μA (Power = 3.03 W). The focal spot size changes with voltage and current (Chaney and Hendee [1974]). For every 1 Watt the focal spot changes by 1 μm . The power of the X-ray source, at the conditions used throughout the remainder

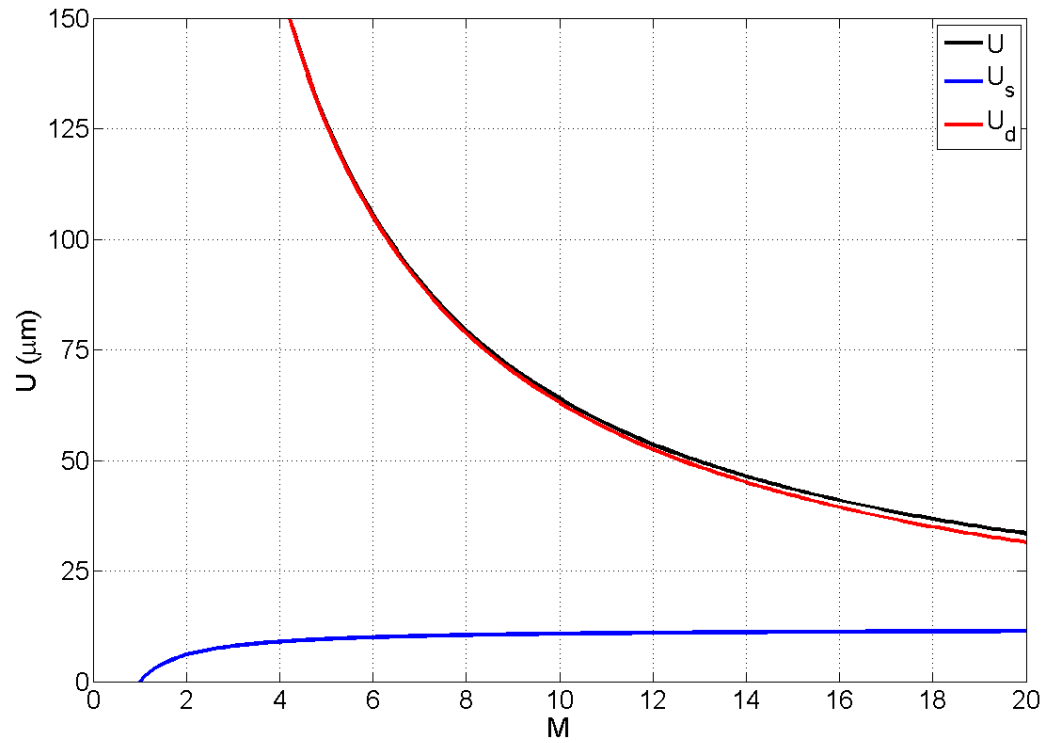


Figure 3.8: The total unsharpness (black) or effective system resolution, versus magnification, M , of an image of an object in the microCT. The effect of the focal spot (blue) and the detector (red) are shown separately. For a $U < 150 \mu\text{m}$ an $M > 4.1$ is required.

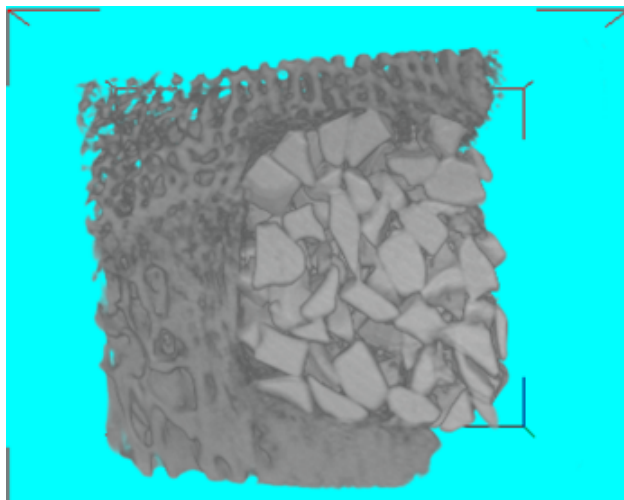


Figure 3.9: A microCT image of the femur of the hind leg of a sheep, implanted with 9 mm synthetic Hydroxyapatite (HA). The image was acquired at $M = 10$ (i.e. effective system resolution is $63 \mu\text{m}$). The trabecular structure of the bone can be resolved.

of the current study, differs by a maximum of 6.97 Watts (7.50 W and 10.0 W, section 3.7). This changes the focal spot size by 6.97 μm . However, this only affects the optimum magnification by less than 0.01, which is insignificant. Therefore, the sample position optimisation as described in this chapter remains valid.

These results were then used to calculate the effective resolution of the system at different magnifications. An effective resolution of 150 μm is sufficient to visualise the trabecular network and to quantify morphological parameters (Ulrich et al. [1999], Majumdar et al. [1997], Laib et al. [1997]). A magnification higher than 4.1 (which corresponds to a source window-sample distance, d_1 of 161 mm) give an effective system resolution higher than 150 μm . This averages the microCT system resolution is sufficient to study the microarchitecture of trabecular bone, and CT-DEA can be used for both cortical and trabecular bone.

Due to the a minimum distance between the X-ray source and sample, d_1 , of 1 mm for the filters and 4 mm for the sample rotation (maximum sample radius), the sample magnification selected to be used was $M = 10$.

3.3 Optimisation of the X-ray spectral pair

Measurements of X-ray attenuation at two different beam energies should allow the separation of the attenuation into its two or three basic components. However, as for any quantitative measurement, all possible sources of error have to be minimised to ensure that uncertainty on final results is not greater than the required accuracy in the measured quantity.

In planar DEA, assuming that the scattered radiation can be effectively removed, then the uncertainty in the measured quantity, σ_f , will be

$$\sigma_f = \sqrt{\sigma_s^2 + \sigma_{add}^2 + \sigma_{Res}^2} \quad (3.9)$$

where σ_s is the sum of the noise in the two original (logarithmic transformed) images, σ_{add} is the total additive electronic noise of the detector and σ_{Res} is the residual background noise, which is related to the two spectra separation (Arvanitis and Speller [2009]). In CT-DEA additional sources of uncertainty in the measured quantity include CT artefacts and image reconstruction.

The optimum imaging conditions have to be met in order to minimise the uncertainty of the above factors. These conditions include the selection of the spectra pair with the lowest σ_{Res} , sufficient beam filtering, high voltage and current for high output intensity and high integration time. In addition, the appropriate corrections are required for eliminating CT artefacts and the maximum number of projections for limiting reconstruction uncertainties.

However, experimentally there is a limit to each of the above conditions, usually introduced by the imaging system. Furthermore, usually most of the above conditions are related. For example, the energy spectra shape is related to SNR and SNR is related to system power limits. It is usually intuitive to choose the two average energies as far from each other as possible, but a too low energy would induce low SNR image. This can be overcome by increasing the X-ray source current, but the power of the source has an upper limit. In addition, the spectra shape is related to beam hardening, scatter reduction is related to SNR and SNR is related to imaging time. For application of the technique *in vivo*, the spectra shape, SNR, CT artefacts reduction are also related to patient dose.

Compromises are required to be made on the selection of the imaging conditions. Sometimes, ensuring that uncertainty on final results is not greater than the required accuracy in the measured quantity might be non reachable (Johnson et al. [2007]).

For the evaluation of the potential effectiveness of the CT-DEA technique, in the assessment of Ca/P ratio and density in bone, compromises were made on the imaging conditions. To make the right compromises all the different combinations of spectra could have been tested experimentally. To simplify this process, a simulation of DEA was initially used, to find σ_{Res} for different combinations of energies. The optimum average energies were prioritised and using the process of elimination, average energies that induced a significantly high uncertainty, due to CT artefacts, were rejected. Finally, the SNR of the raw images was tested and varied experimentally, until the required σ_f was reached. The steps followed were as follows:

1. Theoretical identification of the optimum combination of average energies, to minimise σ_{Res} . This was performed in a simulation, in which the relation of spectra shape to SNR was separated.
2. Identification and elimination of spectra of insufficient/unstable experimental flux, to eliminate CT ring artefacts. This was performed by experiment.
3. Identification and elimination of spectra that produce beam hardening artefacts. This was performed by experiment.
4. The consideration of reducing scattering in the sample.
5. The optimisation of the number of projections, to minimise image reconstruction uncertainty.
6. The optimisation of the number of frames, taking into account the required SNR in the original images, to minimise error in σ_s , and the acquisition time.

The total additive electronic noise, σ_{add} , was assumed to be small compared with the other sources of noise. Dose was not a compromising condition for the

application of the technique through the use of the microCT system. However, dose will need to be one of the most important factors that will affect the selection of optimum conditions, in the potential *in vivo* use of the technique.

3.4 Optimum average energies

3.4.1 Theoretical optimum average energies

The mathematical demonstration of the DEA optimum average energies pair selection method is described by Rebuffel and Dinten [2007], for a two-material decomposition and with monochromatic energy beams. This optimisation method was adapted in this study for a three material decomposition, and was applied to the Ca/P ratio calculation in bone apatite. This is described below.

The X-ray absorbance, S , at the detector, at a low, L , and a high, H , energy, E , after the attenuation of X-rays by bone apatite is expressed by:

$$S_L = \bar{\mu}_{Ca,L}t_{Ca} + \bar{\mu}_{PO_4,L}t_{PO_4} + \bar{\mu}_{OH,L}t_{OH} \quad (3.10)$$

$$S_H = \bar{\mu}_{Ca,H}t_{Ca} + \bar{\mu}_{PO_4,H}t_{PO_4} + \bar{\mu}_{OH,H}t_{OH} \quad (3.11)$$

where t_i is the thickness of a component i in the sample and $\bar{\mu}_{i,E}$ has been defined previously.

Substituting the total sample thickness equation

$$T = t_{Ca} + t_{PO_4} + t_{OH} \quad (3.12)$$

gives

$$S_L = \Delta\bar{\mu}_{Ca,L}t_{Ca} + \Delta\bar{\mu}_{PO_4,L}t_{PO_4} + \Delta\bar{\mu}_{OH,L}t_T \quad (3.13)$$

$$S_H = \Delta\bar{\mu}_{Ca,H}t_{Ca} + \Delta\bar{\mu}_{PO_4,H}t_{PO_4} + \Delta\bar{\mu}_{OH,H}t_T \quad (3.14)$$

where t_T is the total thickness of the sample.

$$\Delta\bar{\mu}_{i,E} = \bar{\mu}_{i,E} - \bar{\mu}_{OH,E} \quad (3.15)$$

Solving the equations 3.13 and 3.14 for t_{Ca}

$$t_{Ca} = \alpha.S_H - \beta.S_L - \frac{\Delta\bar{\mu}_{PO_4,H}.t_T.\bar{\mu}_{OH,H} + t_T.\bar{\mu}_{OH,H}}{\Delta} \quad (3.16)$$

where

$$\alpha = \frac{\Delta \bar{\mu}_{PO_4,L}}{\Delta} \quad (3.17)$$

$$\beta = \frac{\Delta \bar{\mu}_{PO_4,H}}{\Delta} \quad (3.18)$$

$$\Delta = \Delta \bar{\mu}_{Ca,H} \Delta \bar{\mu}_{PO_4,L} - \Delta \bar{\mu}_{PO_4,H} \Delta \bar{\mu}_{Ca,L} \quad (3.19)$$

and

$$S_{L,H} = -\log \frac{N}{N_o} \quad (3.20)$$

where N_o is the number of photons emitted by the X-ray source, and N is the number of photons reaching the detector.

The photon number, N , can be considered as a random variable that has a Poisson distribution of variance N . Variance of the thickness estimate can be derived by differentiating t_{Ca} with respect to the number of photons, N .

$$\sigma_{t_{Ca}} = \frac{(\Delta \bar{\mu}_{PO_4,H})^2 \sigma^2(S_L) + (\Delta \bar{\mu}_{PO_4,L})^2 \sigma^2(S_H)}{\Delta^2}. \quad (3.21)$$

The above equation gives the dependence of $\sigma_{t_{Ca}}$ on $\bar{\mu}_{Ca,L}$, $\bar{\mu}_{PO_4,L}$, $\bar{\mu}_{OH,L}$, $\bar{\mu}_{Ca,H}$, $\bar{\mu}_{PO_4,H}$ and $\bar{\mu}_{OH,H}$, and thus its dependence on the spectra pair, for a particular number of N_o at the low and high energy.

By omitting the error introduced due to 3D image reconstruction, equation 3.21 can also express the error in f_{Ca} , the measured quantity in CT-DEA. The same method can be used to calculate the absolute error in t_{PO_4} and f_{PO_4} . The error in the Ca/P ratio was calculated by propagating the errors of f_{Ca} and f_{PO_4} in equation 2.16, for different combinations of average energies.

By choosing typical material proportions for t_{Ca} (0.40), t_{PO_4} (0.57) and t_{OH} (0.03) present in hydroxyapatite, for each pair of energies, a 2D function of the two energy values was obtained. Figure 3.10 shows the absolute error in the Ca/P ratio as a function of the low-high energy combination, for an input N_o of 10^8 photons. Provided the initial number of photons, N_o , is the same for both the high and low average energies, the relative distribution of absolute error shown in figure 3.10 will remain constant. To simplify this process this optimisation method was performed under the assumption of N_o being the same at the low and high average energy.

From the plot the theoretical optimum imaging conditions were obtained. The theoretical optimum combination of energies is the one that gives the lowest $\sigma_{f_{Ca/P}}$

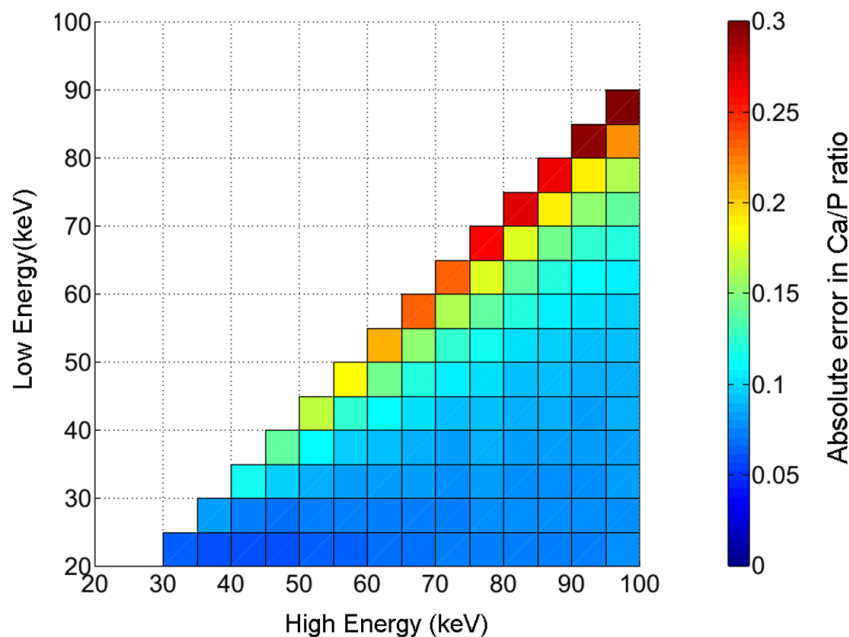


Figure 3.10: Absolute error in Ca/P ratio for different energy combinations.

(dark blue areas in figure 3.10), 25 keV for the low average energy and 40 keV for the high average energy.

However, in a conventional CT scanner the number of possible energy combinations is restricted. In the next sections, the compromises on the selection of the optimum energy pair are discussed.

3.4.2 Beam filtration

When using a polychromatic beam, beam filtration is required to produce a particular average energy. Furthermore, beam filtration has the advantage of reducing beam hardening.

The different possible filter combinations for DEA are described by Sorenson et al. [1989]. Filtration can be added to the high energy beam to remove lower energy photons, and/or to the low energy beam to lower the average energy and resulting in greater energy difference between the two spectra.

Advantage can be made of the different absorption K-edge of the filtering materials. For example, filters made of Tin (K-edge 29.2 keV), Caesium (K-edge 36.0 keV), Tellurium (K-edge 31.8 keV), Cerium (K-edge 40.4 keV), Samarium (K-edge 46.8 keV) and Gadolinium (K-edge 50.2 keV) can be used to absorb the photons in these energy ranges and thus increase the average energy of the spectrum. Lower energy photons can be eliminated using Copper (K-edge 9.0 keV) and Aluminium (K-edge 1.6 keV).

In some cases advantage can be made of the K-edge of the sample component of

3. Dual energy analysis optimisation

Table 3.1: Examples of filtration added to a 100 kVp beam using Samarium (Sm), Gadolinium (Gd), Tin (Sn) and Copper (Cu) of different thicknesses. The average energy (\bar{E}) is shown and the presence of ring artefacts is stated. In all cases the number of projections was 360 and the number of frames was 256.

Voltage (kVp)	Current (uA)	Filter	K-edge (keV)	t (mm)	\bar{E} (keV)	Ring artefact
100	200	Gd	50.2	0.35	86	Yes
		Sm	46.8	0.40		
		Sn	29.2	0.50		
100	200	Gd	50.2	0.10	78	Yes
		Sm	46.8	0.10		
		Sn	29.2	0.50		
100	100	Sn	29.2	0.5	71	No
100	100	Sn	29.2	0.2	67	No
100	100	Cu	29	0.2	63	No
		Cu	9	0.5		

interest. Filters of K-edges close to the K-edge of the sample component of interest can be used to produce two average energies, one below and one above the K-edge of the component of interest (Arvanitis and Speller [2009]). This approach though, could not be used for the purposes of this study because the K-edges of Calcium and Phosphorus are 4.04 keV and 2.15 keV respectively. This is much too low for diagnostic imaging.

There are some restrictions to the selection of the appropriate filters. The filter materials must be non-toxic, uniform, low-cost and easily accessible. Additionally, the fraction of incident intensity transmitted through the filter and the scatter signature of each filter have to be considered.

3.4.3 System power

An important constraint to the average energies to be used in DEA is set by the power limits of the imaging system. Using the microCT system, average energies lower than 30 keV were practically impossible to achieve due to insufficient flux for an image to be produced at these energies. Therefore, the theoretical optimum combination (figure 3.10) of energies, 25 keV for the low average energy and 40 keV for the high average energy, were rejected. The next optimum imaging average energies are 30 keV (as low as possible), and 100 keV (as high as possible).

The higher the average energy selected, the higher the X-ray source current or the longer the acquisition time required. This is due to the large amount of filtration required to achieve a high average energy. Examples of the amount of filtration, added in a 100 kVp beam, required to produce average energies higher than 63 keV, are presented in table 3.1.

3. Dual energy analysis optimisation

It was found that at current values above 200 μA , when the voltage was set at 90-100 kVp, the average energy produced by the X-ray source deviated significantly from the expected average energy. Figure 3.11 shows an example of the effect of current on the average energy. The measurement of average energy was made at 95 kVp and using 0.2 mm Samarium, 0.35 mm Gadolinium and 0.5 mm Tin, for filtration and an ion chamber for the measurement of Air Kerma (Gy). Ten Aluminium filters ($t = 1$ mm) were used for the calculation of the half-value layer and the average energy of the spectrum (Webb [1988]). At each current, five measurements of average energy were measured and averaged. The expected average energy at the above conditions was 81 keV, as calculated using a simulated spectrum by SpeKCalc software (Poludniowski et al. [2009]). However, at a current higher than 200 μA the average energy was decreased by 6%.

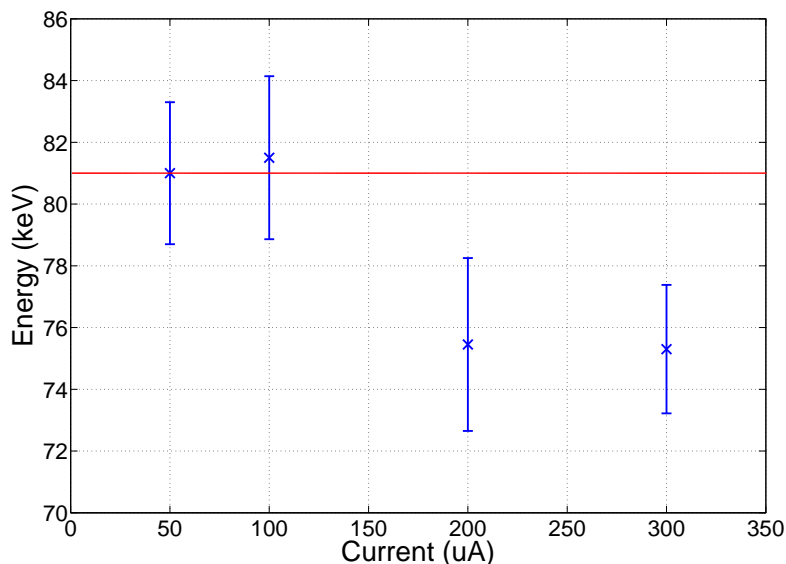


Figure 3.11: Example of the effect of current on the average energy. The measurement of average energy was made at 95 kVp and using 0.2 mm Samarium, 0.35 mm Gadolinium and 0.5 mm Tin for filtration. The expected average energy was 81 keV as shown by the red line. The errors represent the standard deviation.

It was found that a current value of 500 μA , when the voltage was set at 95 kVp, the microCT system source presented a decrease in dose with time. A possible reason for this phenomenon is that the characteristics of X-ray source might change with temperature. Figure 3.12 shows the measurements of dose made at 95 kVp and 500 μA and a beam filtration of 0.35 mm Gadolinium and 0.4 mm Samarium, using a dose meter, positioned just in front of the detector. The dose (in $\mu\text{Sv}/\text{hour}$) was measured every 5 seconds and the average of every successive 50 seconds was calculated for a period of 1000 seconds.

Additionally, it was found that at current values 200-500 μA , when the voltage was set at 90-100 kVp, the reconstructed microCT image included ring artefacts.

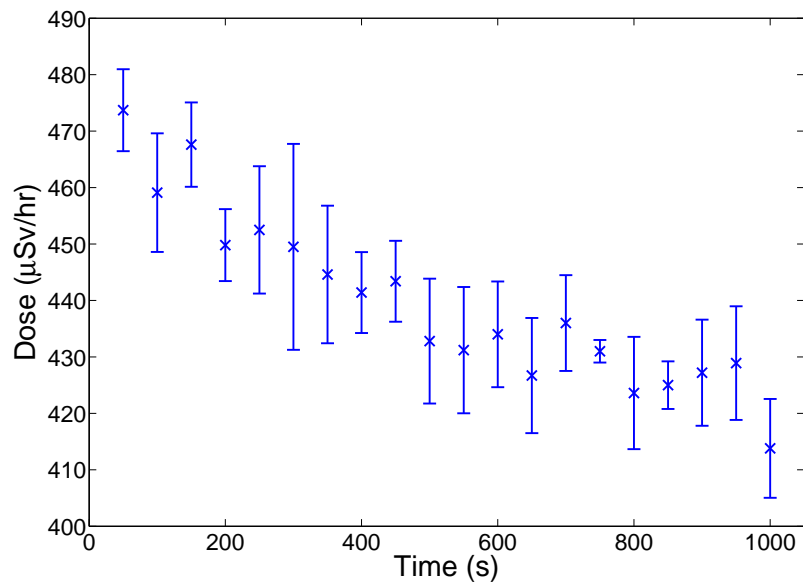


Figure 3.12: The average dose measurements, made every 50 seconds, at 95 kVp, 500 μA and a beam filtration of 0.35 mm Gadolinium and 0.4 mm Samarium. The plot demonstrates the instability in dose with time when the microCT is used at a high power. The error bars represent the standard deviation.

Figure 3.13 shows an example of an image of a bone phantom acquired at 95 kVp, 500 μA , 0.4 mm Samarium, 0.35 mm Gadolinium and 0.5 mm Tin.

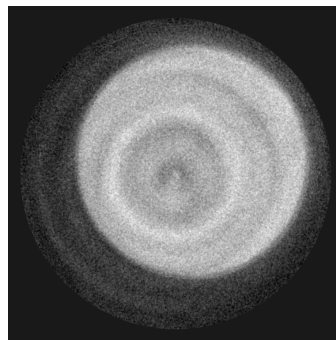


Figure 3.13: Example of a slice of a microCT image of a bone phantom, acquired at 95 kVp and 500 μA and with an external filtration to source window of 0.35 mm Gadolinium (Gd) and 0.5 mm Tin (Sn). Ring artefacts being present.

It was beyond the scope of this study to investigate further the source of the above problems. However, conditions needed to be found that eliminated them, since their presence could affect the CT grey value, at the low (G_L) and high energy (G_H).

It was concluded that at 90-100 kVp, a current higher than 100 μA could not produce a stable flux and/or images with no ring artefacts. Using a current lower than 100 μA ensured that the average energy remained stable (figure 3.11). However, the subsequent images then suffered from insufficient SNR because of low current and high filtration. The higher average energy that could be delivered, with a low

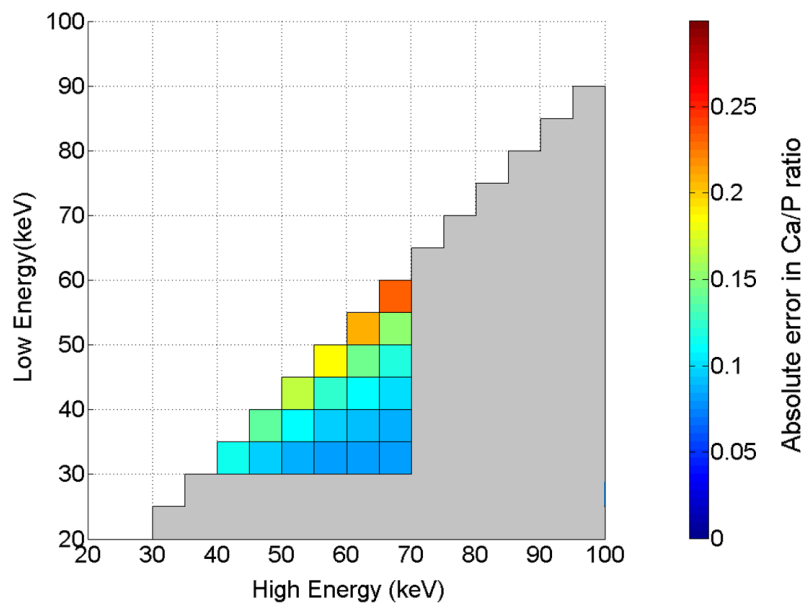


Figure 3.14: Absolute error in Ca/P ratio for different energy combinations. The highlighted light-grey areas represent the energies eliminated for practical reasons such as flux instability with time and the production of ring artefacts in the images.

current ($<100\mu\text{A}$), was 71 keV (table 3.1). At average energies lower than this, there was no error introduced on G_L and G_H due to flux/average energy instability and ring artefact.

In conclusion, the system power limited the range of possible average energies. average energies below 30 keV could not be delivered, while the high energy was limited to 71 keV because of a combination of current, flux stability and SNR. Deliverable energies, together with the necessary filtration, are defined in table 3.1. The restricted energy range has been highlighted in light-grey in figure 3.14.

3.4.4 Beam hardening

Beam hardening causes a decrease in the linear attenuation coefficient, $\bar{\mu}(E, \rho_{\text{eff}}, Z_{\text{eff}})$, with increasing sample thickness, due to more low energy photons being absorbed, narrowing the spectrum and causing a subsequent increase in the average energy. In a CT image of a cylindrical homogeneous sample, a decrease in the grey value appears in the centre of the sample, producing a ‘cupped appearance’ in the line profile of a CT slice. Figure 3.15 shows (a) a slice through a CT image of a bone phantom with a line profile selection, and (b) its corresponding profile plot.

The presence of beam hardening under different imaging conditions was tested experimentally. The lowest average energy was 30 keV, corresponding to a peak voltage of 50 kVp. As such, a cylindrical homogeneous bone phantom was imaged at 50 kVp and 60 kVp, for investigating the presence of beam hardening. Results showed that the average energy range 30-35 keV was affected by beam hardening

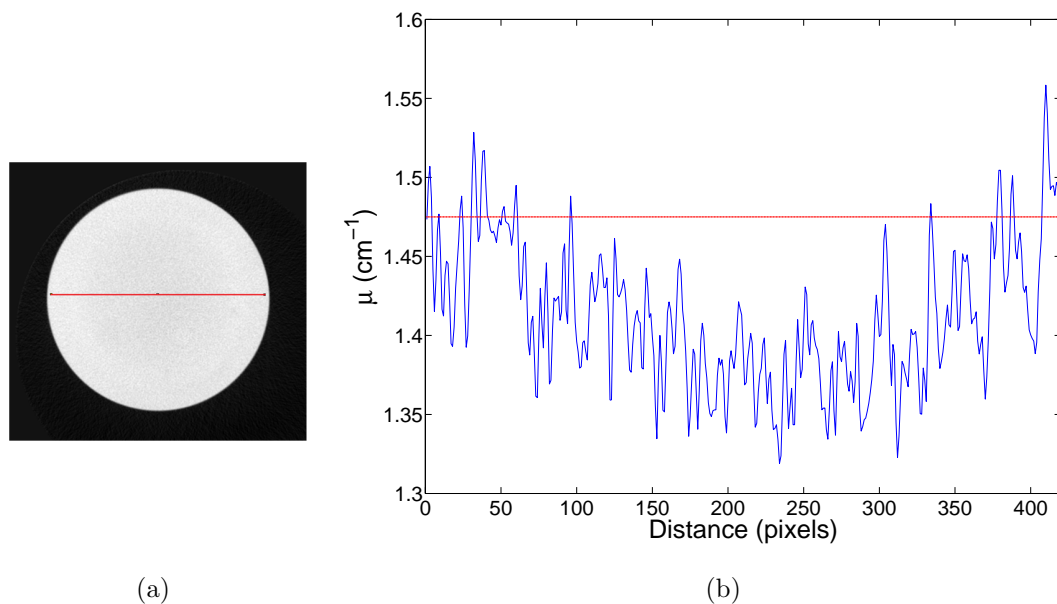


Figure 3.15: (a) A slice through a microCT image of a bone phantom with a line profile selection, and (b) its corresponding profile plot. Beam hardening is shown by the ‘cupped appearance’ of the line profile. The red line represents the expected appearance attenuation coefficient.

Table 3.2: Examples of filtration added to a 50 kVp and 60 kVp beam using Aluminium (Al) of different thicknesses, t . The average energy (\bar{E}) is shown and the presence of beam hardening is stated. In all cases the number of projections was 360 and the number of frames was 256.

Voltage (kVp)	Filter	K-edge (keV)	t (mm)	\bar{E} (keV)	Beam hardening
50	none	—	0	30	Yes
60	none	—	0	33	Yes
50	Al	1.6	3.00	35	Yes
50	Al	1.6	5.00	36	No
60	Al	1.6	5.00	40	No

artefacts, as shown in the first three rows of table 3.2. The highest average energy of 71 keV, produced by a peak voltage of 100 kVp, did not demonstrate any beam hardening because of the filtration.

For the reduction of beam hardening, filtration is usually used to pre-harden the X-ray spectrum. Alternative beam hardening corrections are calibration correction (Liu et al. [2009]) and beam hardening correction software. However, in this study, due to the use of quantified analysis of the images, the last two beam hardening correction methods were avoided.

As shown in table 3.2, beam hardening becomes negligible when sufficient external filtration (e.g. 5 mm Aluminium) is added to a 50 kVp beam, resulting in an average energy of 36 keV for the low energy beam. The effect of beam hardening

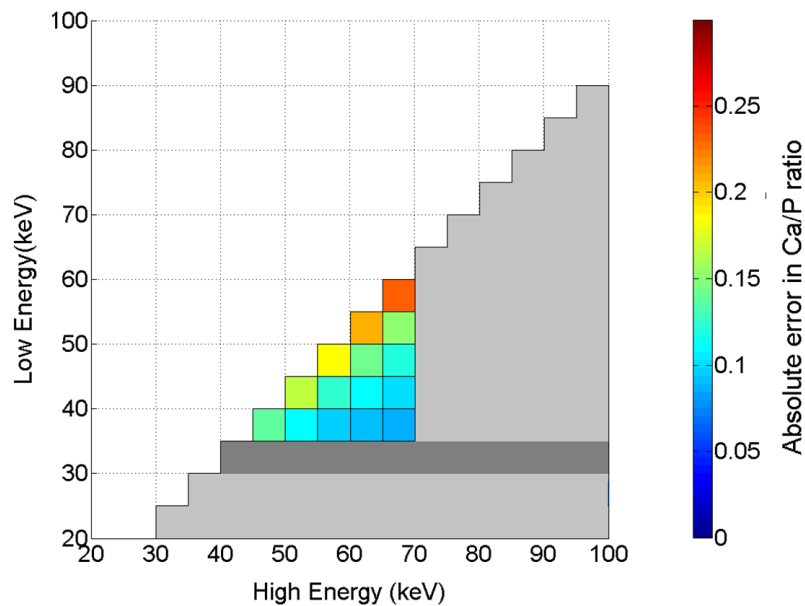


Figure 3.16: Absolute error in Ca/P ratio for different energy combinations. The highlighted light-grey areas represent the energies eliminated for practical reasons such as flux instability with time and ring artefacts in the images. The highlighted dark-grey areas represent the energies eliminated due to the presence of beam hardening in the microCT images.

therefore put some further restrictions on the possible average energies that could be used. These are shown in the bottom two rows in table 3.2 and are highlighted in dark-grey in figure 3.16.

3.5 Scattering

Scattering is unavoidable in imaging and makes quantification difficult (Dinten [2001]). If the sample is close to the detector, the scatter contribution may reach two or three times the direct flux (Rebuffel and Dinten [2007]).

Usually, for medical applications, anti-scattering grids are used to minimise scatter. This requires the estimation of scatter from a set of points (behind the grids) and then its subtraction from the sample image (Endo et al. [2001], Ning et al. [2004]). However, this requires an additional acquisition, increasing acquisition time (and dose to patient in any potential clinical application of the technique) and it does not fully eliminate scatter either. Usually compromises need to be made between the effect of scatter in the grey value of the image and the disadvantages introduced by the use of anti-scattering grids.

The scatter magnitude decreases as the sample to detector distance increases, until it reaches a point where the scatter continues plateaus. In this study the sample was placed at a distance as far as possible away from the detector (section 3.6.2), therefore scatter contribution was minimised and no anti-scattering grids were used.

3.6 Signal to noise ratio

3.6.1 Noise in CT dual energy imaging

The DEA experimental feasibility in decomposing a specific material, using a particular imaging system at particular imaging conditions, is dependent on the noise (σ_s) in the original low and high energy image (Fabbri et al. [2002]). The noise in the original low and high energy image would define the accuracy with which CT-DEA can assess the Ca/P ratio. As discussed in section 1.4.3 the ideal case would be to achieve a precision of better than 0.09 in the Ca/P ratio assessment, given that the min/max difference in the Ca/P ratio between healthy and IMO bone samples is 0.09/0.43 (Tzaphlidou et al. [2005], Speller et al. [2005], Kourkoumelis et al. [2011]).

At different average energies (and thus different $m_{i,L}$ and $m_{i,H}$) the maximum noise (minimum signal to noise ratio (SNR)) in the low and high energy images needed to achieve the required accuracy in the measured quantity is different. Once the average energies that introduce beam hardening and ring artefacts are eliminated, and a possible optimum spectral pair is known, a simple calculation can be performed to estimate the maximum noise and minimum SNR needed to achieve the required accuracy in the measured quantity. The minimum SNR can then be used to test the experimental feasibility of the technique at the optimum imaging conditions.

This calculation is a simulation process and is performed in two steps. In the first step a typical sample (of known chemical composition) is irradiated at the optimum imaging conditions, for the calculation of the linear attenuation coefficients at the low and high energies. The linear attenuation coefficients form the inputs of the second step, in which CT-DEA decomposes the sample into its material components. An uncertainty (noise) is added to the linear attenuation coefficient, and the error in the measured quantity is calculated.

A typical bone apatite sample, of known chemical composition ($\text{Ca}_6(\text{PO}_4)_{10}(\text{OH})_2$), Ca/P ratio (1.67) and density ($\rho_{\text{eff}} = 3.0 \text{ g/cm}^3$) was irradiated, at 50 kVp and 100 kVp, with filtration 5 mm Al and 0.5 mm Sn respectively (producing average energies of 36 keV and 71 keV). The low and high energy linear attenuation coefficients were calculated. The decomposition of the sample, using CT-DEA, was performed several times, each time introducing a different uncertainty (up to ± 0.06) in the variables (μ_L and μ_H).

Figure 3.17 shows the absolute error introduced in the Ca/P ratio of a typical bone apatite sample, by an uncertainty in μ_L and μ_H . The plot shows that the higher the deviation from the correct μ_L and μ_H value, the higher the error introduced in the measured quantity. The optimum number of projections and frames would

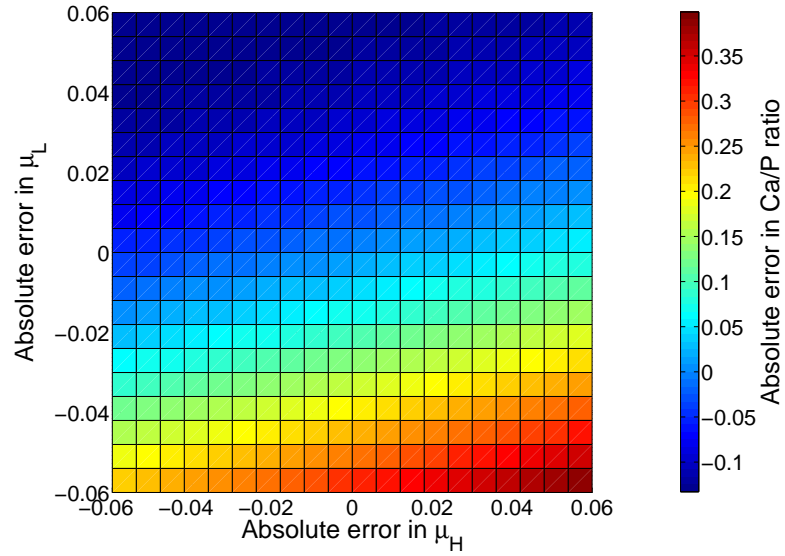


Figure 3.17: Absolute error in Ca/P ratio for different combinations of noise in μ_L and μ_H .

finally define the uncertainty in μ_L and μ_H , thus the error in Ca/P ratio. These are discussed below. But, firstly, the definition of the μ_L and μ_H as a function of the CT grey value had to be studied.

3.6.2 CT grey value calibration

To allow for the absolute Ca/P ratio quantification in bone, the experimentally-measured inputs ($\bar{\mu}_L$ and $\bar{\mu}_H$) to the DEA equations should have a realistic physical meaning. This required calibration of the CT grey value, at the low (G_L) and high energy (G_H).

This was calculated using five di-Potassium Phosphate (K_2HPO_4) solutions of different concentrations (1-5 g/cm³). These samples were chosen because of their uniformity and similar X-ray attenuation to bone apatite (Genant and Boyd [1977]) (section 2.5.1).

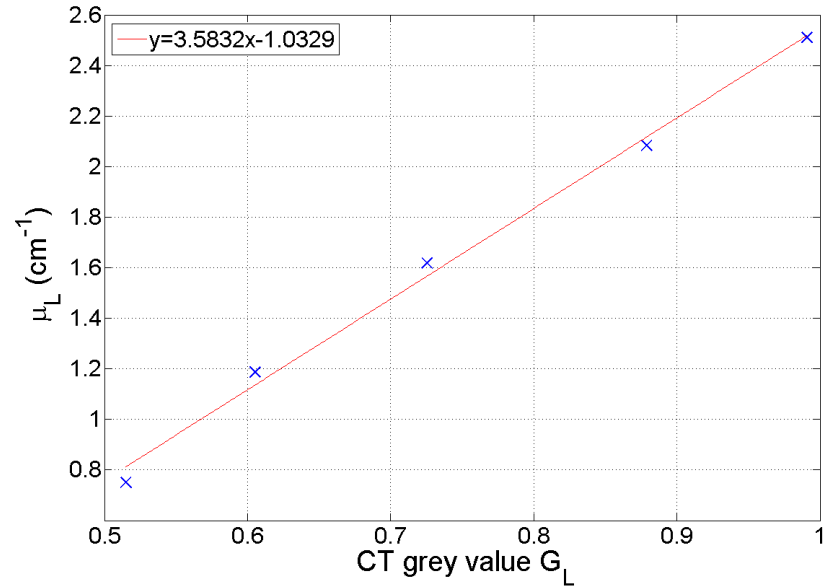
At the imaging conditions described above the theoretical linear attenuation coefficient, $\bar{\mu}$, of each solution was calculated (Burgess [1987]).

$$\bar{\mu}(E, \rho_{\text{eff}}, Z_{\text{eff}}) = \bar{m}_{K_2HPO_4}(E)c_{K_2HPO_4} + \bar{m}_{H_2O}(E)c_{H_2O} \quad (3.22)$$

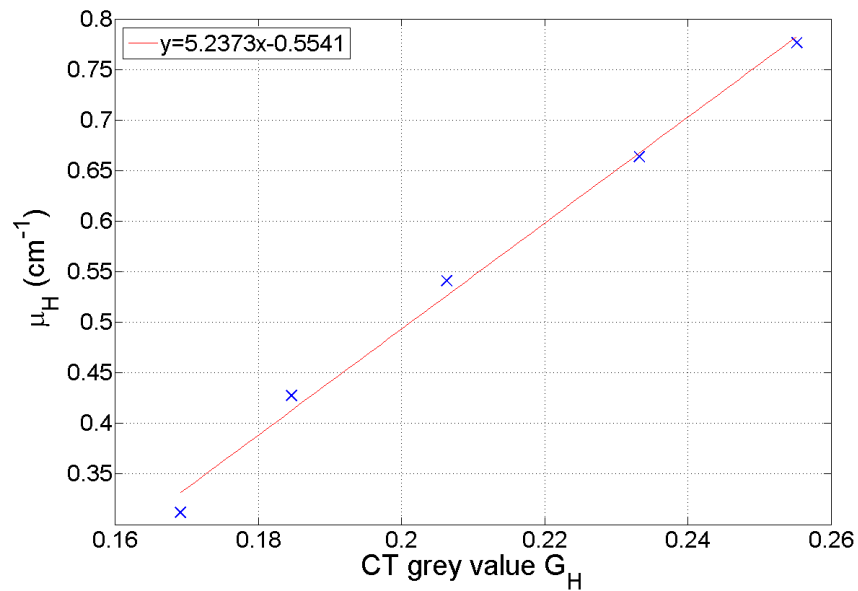
where \bar{m}_i and c_i are the average mass attenuation coefficient and concentration (in g/ml) of component i , respectively.

Linear relationships ($R^2 = 0.99$) were found between the theoretical and measured values of average linear attenuation coefficient and CT grey value.

Figure 3.18 shows calibration of the microCT grey value to the theoretical linear



(a)



(b)

Figure 3.18: Calibration of the microCT grey value to the theoretical linear attenuation coefficient (in cm^{-1}) at the (a) low energy and (b) high energy imaging conditions. The calibration was performed using five K_2HPO_4 solutions of different concentrations. The red line through the points represents the resulting equation of the calibration procedure.

attenuation coefficient (in cm^{-1}) at the (a) low energy and (b) high energy imaging conditions. The calibration curves provided a physical meaning to the CT grey value, with high correlation coefficient providing high confidence. The red line through the points represents the line of best fit. For the low energy image, the calibration equation is

$$\bar{\mu}_L = 3.58G_L - 1.03; R^2 = 0.99 \quad (3.23)$$

and for the high energy image the calibration equation is

$$\bar{\mu}_H = 5.24G_H - 0.55; R^2 = 0.99 \quad (3.24)$$

All images acquired for the purposes of this study were processed using the calibration equations above, before further analysis.

3.6.3 Number of projections

There is a minimum number of projections required to reconstruct a volume. At a minimum there is a requirement of one projection ray to pass through each voxel. At the centre of rotation this is not a problem. However, as the distance from the centre of the sample increases, less rays pass through the voxel. Therefore, the furthest point from the centre of rotation needs to be taken into account when calculating the minimum number of projections. The minimum number of projections in a CT acquisition, P_{min} can be calculated using

$$P_{min} = \frac{C}{V_d} \quad (3.25)$$

where C is the sample circumference and V_d is the voxel resolution.

Voxel binning ($6 \times 6 \times 6$ voxels) was used to increase the signal to noise ratio of the images and reduce image acquisition and processing time. This provided a voxel resolution of $96 \mu\text{m}$, sufficient to resolve trabecular structures (section 3.2). For a sample of radius 4 mm , voxel resolution of $96 \mu\text{m}$, the above equation gives a minimum number of projections of 262. Any number of projections bigger than this would require a compromise with image acquisition time, flux stability and in case of clinical use of the technique, patient dose. In this study 360 projections were used, a typical value for CT imaging.

3.6.4 Number of frames

The CT frame number is the number of images acquired and averaged at each projection during an image acquisition and it is proportional to the integration

time of an image acquisition. The optimum number of frames is dependent on the absolute deviation from the expected μ_L and μ_H , and the image acquisition time, as well as dose (if the technique is to be applied *in vivo*).

The K_2HPO_4 solutions (section 2.5.1), were imaged at the optimum low and high energies, using 360 projections and 128 frames. This number of frames was chosen as it has an acceptable acquisition time (35 minutes). The average μ_L and μ_H of 10 random volumes of $6 \times 6 \times 6$ binned voxels ($8.9 \times 10^{-4} \text{ mm}^3$), in the reconstructed microCT image, was calculated. The maximum deviation from the expected μ_L and μ_H was found. This was 0.06 for μ_L and 0.02 for μ_H . According to figure 3.17, the maximum absolute error in the Ca/P ratio with these deviations from the expected μ_L and μ_H is 0.12. This is considered sufficient for distinguishing between most of the healthy and IMO regions in bone.

3.6.5 Correction of the centre of rotation

The reconstruction algorithm expects the projections image to be perfectly centred on the rotation axis. If it is not a ring is produced around the sample in its reconstructed image. It is physically very difficult to align the centre of the sample with the X-ray central axis. The projection images need to be shifted to correct for this displacement before reconstructing the microCT image.

In this study, CT Pro software ‘automatic’ method was used to correct for the misalignment of the COR (Nikon Metrology, X-Tek, United Kingdom), which would affect μ_L and μ_H , and thus the Ca/P ratio precision. In this method, two selected slices, one near the top and one near the bottom of the sample, were reconstructed. The contrast of the sample with its background was assessed to determine the amount of correction needed in each. For each slice, the projections were then shifted to one side by one pixel, the reconstruction was repeated and contrast was reassessed. After many repetitions of the same procedure and iterative movement of the sample, the required shift was estimated once the slice reached its required quality. No details were provided in the system manual as to precisely how this was completed, but it was clear from visual assessment.

The two values of misalignment from the two slices at the top and bottom of the sample indicated the shift needed to correct all of the projections. CT reconstruction was then performed using the in-built X-Tek software (Nikon Metrology, X-Tek, United Kingdom).

Figure 3.19 shows an example of a reconstructed bone phantom microCT image (a) without and (b) with the correction of the COR. It worth noting that after the correction of the image using CT Pro software, there is an increase to the grey value of the image by a factor of 100. Therefore, in order to convert the grey value

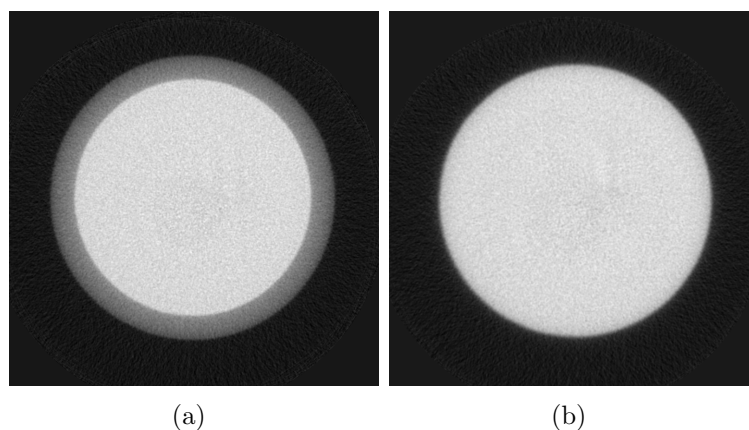


Figure 3.19: A reconstructed bone phantom microCT image (a) without and (b) with the correction of the COR, using CT Pro software.

coefficient to its usual unit, cm^{-1} , the grey value of the COR-corrected image needs to be divided by 100.

3.7 Conclusions on the optimum imaging conditions

After compromising between the theoretical optimum spectra and the ring and beam hardening artefacts of the microCT, the number of projections, the SNR in the low and high energy microCT images, image acquisition time and the required accuracy in the Ca/P ratio, the optimum average energies were found to be: 36 keV and 71 keV. These are produced with a tube voltage pair of 100 kVp and 50 kVp, and respective tube currents of $100 \mu\text{A}$ and $150 \mu\text{A}$, after filtering with 5.00 mm Al and 0.50 mm Sn. Figure 3.20 shows the simulated energy spectra used in the CT-DEA, calculated using the SpekCalc Software (Poludniowski et al. [2009]) and taking into account the inherent filtration (1.3 mm Aluminium) of the X-ray source. Scanning parameters were: magnification = 10, 360 projections. For each projection 128 frames were acquired and averaged. Dose is a subject of imaging conditions and imaged body part, and needs to be taken into account, but only when the developed technique is applied *in vivo*. The above conditions are expected to give an accuracy in the Ca/P ratio of 0.12 (section 3.6.4). With this accuracy the CT-DEA technique should identify most of the osteoporotic regions in bone.

Table 3.3 summarises the experimental imaging conditions, for the low and high energy images, used in this study. These conditions represent the optimum imaging conditions for the assessment of the Ca/P ratio in bone using the X-Tek benchtop microCT system (serial number: J0001). The optimum conditions will vary between different systems since they are a subject of system power. All the low and high

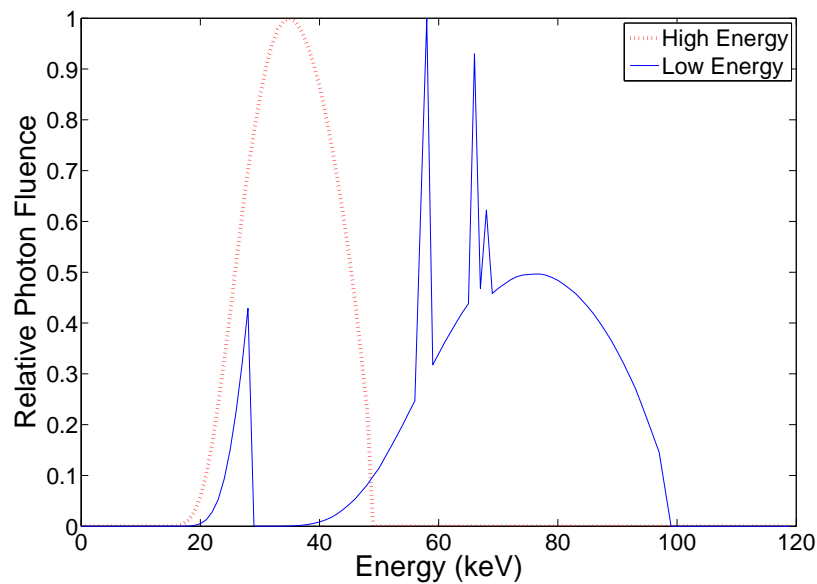


Figure 3.20: Simulated X-ray energy spectra used in CT-DEA.

energy images acquired for the purposes of the remainder of this study were produced at the conditions below, unless stated otherwise.

Table 3.3: Experimental imaging conditions used for all the imaging performed using the X-tek benchtop microCT system in this study.

Imaging Condition	Low E Image	High E Image
Voltage (kVp)	50	100
Current (μ A)	150	100
Filter material	Al	Sn
Filter thickness (mm)	5.00	0.50
Average energy (keV)	36	71
Magnification	10	10
Projections	360	360
Frames	128	128

3.8 Summary

Using the measurements of unsharpness (Full Width at Half Maximum (FWHM) of the Line Spread Function (LSF)) of the system from an edge at different positions along the source-detector line and the χ^2 factor (a factor that is usually used to define the agreement between the observed and expected distributions), the focal spot size and the intrinsic detector resolution of the microCT were calculated. The result of intrinsic detector resolution was confirmed using the Modulation Transfer Function (MTF). Using the focal spot size and the intrinsic detector resolution, the total unsharpness of an object under magnification at different positions along the

source-detector was calculated and the optimum sample magnification was identified. This was $M = 10$, corresponding to a system resolution of $63 \mu\text{m}$, sufficient to resolve the trabecular architecture.

Furthermore, the optimum spectra, for a sufficient precision in the Ca/P ratio calculation were identified. The optimum theoretical spectral pair was firstly identified. Then the X-ray spectra that produce CT artefacts were eliminated. The number of projections and frames that give an accuracy of 0.12 in the Ca/P ratio were chosen. All the imaging conditions that were selected for the purposes of this study, and will be referred to in the rest of this thesis, are summarised in table 3.3.

Chapter 4

Evaluation of CT-DEA

4.1 Overview

In this chapter the evaluation of CT-DEA for density and Ca/P ratio 3D assessment in bone are described.

In section 4.2 the theoretical precision of the technique in the calculation of density and Ca/P ratio was assessed in a simulation of CT-DEA. In section 4.3 the method and results of the experimental precision of CT-DEA, using di-Potassium Phosphate solutions and bone phantoms, of known density and/or Ca/P ratio, are discussed.

The feasibility of the technique on real bone apatite was tested using healthy and IMO rabbit collagen-free cortical bone samples. The quantitative abilities of the technique on real bone were assessed by comparing it with the a 2D Ca/P ratio assessment method, electron-dispersive X-ray spectroscopy. The methods used and the results are presented in section 4.4.

In section 4.5, a summary of the chapter is made.

4.2 Theoretical precision of CT-DEA

4.2.1 Simulation method

The simulation of CT-DEA was used to find its theoretical precision in density, and Ca/P ratio (as a result of an error in the weight fraction of Ca (f_{Ca}) and the weight fraction of P (f_P)).

The simulation included two steps: i) the irradiation process, and ii) the decomposition process. In the irradiation process, the X-ray attenuation by the ten different bone phantoms (section 2.5.2) was calculated. The chemical formula of each phantom and a range of densities of 1.81-2.95 g/cm³ (equal to the total sample

Table 4.1: Simulation results. Deviation from the expected density for ten phantoms of different Ca/P ratio. All phantoms of same chemical formula (but different density) had identical density errors.

Chemical Formula	Density _{total}	Density error (g/cm ³)
Ca(H ₂ PO ₄) ₂ (H ₂ O)	2.54	0.02
Ca(H ₂ PO ₄) ₂ (H ₂ O)	2.39	0.02
CaHPO ₄	2.97	0.03
CaHPO ₄ .2H ₂ O	2.95	-0.02
CaHPO ₄ .2H ₂ O	2.81	-0.02
Ca ₃ (PO ₄) ₂	2.10	-0.01
Ca ₃ (PO ₄) ₂	2.21	-0.01
Ca ₅ OH(PO ₄) ₃	2.08	0
Ca ₅ OH(PO ₄) ₃	2.27	0
Ca ₅ OH(PO ₄) ₃	1.81	0

density, assuming they are equal to the sample material density, table 2.2) were used to calculate the theoretical average linear attenuation coefficients, $\bar{\mu}(Z_{\text{eff}}, \rho_{\text{eff}}, E)$, at the two X-ray beam energies, used in CT-DEA, using equation 2.6.

In the decomposition process, the CT-DEA algorithm (section 2.4.4) was used for the calculation of density and Ca/P ratio in bone apatite. The theoretical $\bar{\mu}(Z_{\text{eff}}, \rho_{\text{eff}}, L)$ and $\bar{\mu}(Z_{\text{eff}}, \rho_{\text{eff}}, H)$ of each phantom was input to the CT-DEA algorithm and the phantom was decomposed into its heaviest materials (maximum three), as described in table 2.2. The actual density, f_{Ca} , f_P and Ca/P ratio of each phantom were compared to the CT-DEA theoretical density, f_{Ca} , f_P and Ca/P ratio results.

4.2.2 Results: theoretical precision

The theoretical precision in the calculation of density of ten bone phantoms, of five different chemical formula is shown in table 4.1. Two/three phantoms of the same chemical formula and different density have the same error in density calculation. The reason for this is discussed below. The density results suggest a mean/maximum precision in density of 0.01/0.03 g/cm³ or 0.63%/1.14%.

Similarly, the theoretical precision in the calculation of f_{Ca} and f_P , is shown in figure 4.1. The results suggest a mean/maximum precision of 0.01/0.02 or 3.71%/12.58% for f_{Ca} and 10.38%/24.41% for f_P . These errors are propagated into the calculation of Ca/P ratio. As can be seen in figure 4.2 phantoms of the same chemical formula but different density give the same error in Ca/P ratio calculation. This shows that the Ca/P ratio results are independent of the density results. The mean/maximum precision in Ca/P ratio calculation in bone phantoms is 0.10/0.28 or 14.21%/45.00%. This would be low enough to distinguish between some, but not all, healthy and osteoporotic bone samples, since in literature a minimum/maximum

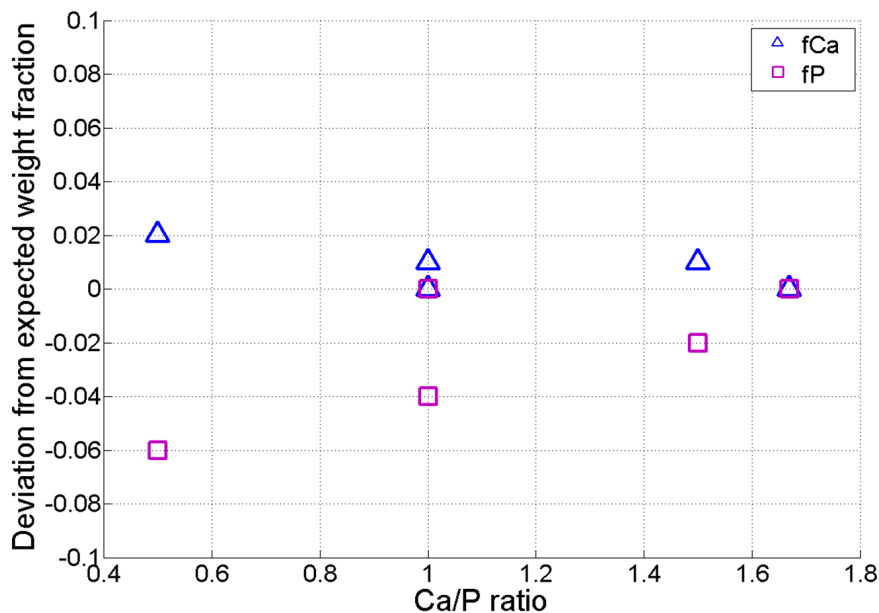


Figure 4.1: Simulation results. Deviation from the expected f_{Ca} (blue triangles) and f_P (pink squares) for phantoms of different Ca/P ratio. All phantoms of same Ca/P ratio had identical f_{Ca} and f_P errors.

difference of 0.09/0.43 in Ca/P ratio is reported between healthy and IMO bone samples Tzaphlidou et al. [2005], Kourkoumelis et al. [2011]).

In a simulation usually zero error is expected in the result of the measured quantity. One source of error in the Ca/P ratio is the presence of a fourth component in the bone phantoms (table 2.2). However, even phantoms that are made up of three components still give a non-zero error. This shows that the main source of the errors is the non-perfect fit of the relations of $F(Z_{\text{eff}})$ to Z_{eff} and Z_{eff} to \bar{m}_L of each of the phantoms. This is further supported by the fact that two phantoms of the same Ca/P ratio, but different density, and thus different $\bar{\mu}(Z_{\text{eff}}, \rho_{\text{eff}}, L)$ and $\bar{\mu}(Z_{\text{eff}}, \rho_{\text{eff}}, H)$, have the same errors in density (since density is a function of $F(Z_{\text{eff}})$ to Z_{eff} and Z_{eff} to \bar{m}_L relations). As shown in table 4.1 the error in density calculation by CT-DEA is independent of density, and it is a subject of the calibration of $F(Z_{\text{eff}})$ to the chemical formula of the sample.

At present, these approximations of the mathematical relations are required in CT-DEA for bone material decomposition. This is because the exact chemical composition of biological apatite is diverse and not known with sufficient accuracy to enable the construction of a precise look-up table of $F(Z_{\text{eff}})$ to Z_{eff} and Z_{eff} to \bar{m}_L .

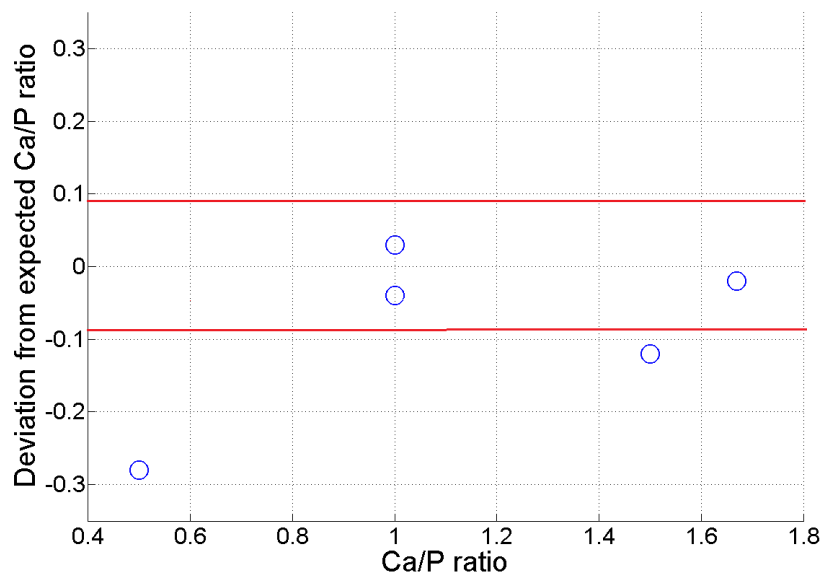


Figure 4.2: Simulation results. Deviation from the expected Ca/P ratio for phantoms of different Ca/P ratio. The red line represents the minimum difference between healthy and IMO bone samples found in literature.

4.3 Experimental precision of CT-DEA

4.3.1 Experimental methods

Five K_2HPO_4 solutions (section 2.5.1), of different, known (material) density, and ten bone phantoms (section 2.5.2), of known Ca/P ratio and total density, were imaged using the microCT system (2.2.3) at the optimum imaging conditions (table 3.3). The bone phantoms were used for the calculation of the experimental precision in density and Ca/P ratio, and the K_2HPO_4 solutions (section 2.5.1) were used for further testing the density precision result.

CT reconstruction was performed on the images using the in-built X-Tek software (Nikon Metrology, X-Tek, United Kingdom) at a slice thickness of $16 \mu\text{m}$. Any centre of rotation artefacts were corrected using CT Pro software (Nikon Metrology, X-Tek, United Kingdom). The microCT system grey values were converted to $\bar{\mu}(Z_{\text{eff}}, \rho_{\text{eff}}, E)$ values using the calibration equations (section 3.6.2). Finally, all K_2HPO_4 solutions and bone phantom images were binned into $6 \times 6 \times 6$ voxels, thus providing a resolution of $96 \mu\text{m}$ in all dimensions.

The density of the K_2HPO_4 solutions was assessed using CT-DEA to compare with their expected density, to assess the precision of the technique in the (material) density calculation. K_2HPO_4 solutions were chosen for the density validation as they have no air gaps, that would introduce errors in the calculation of the expected (material) density.

Similarly, the density and Ca/P ratio of the bone phantoms was assessed by CT-

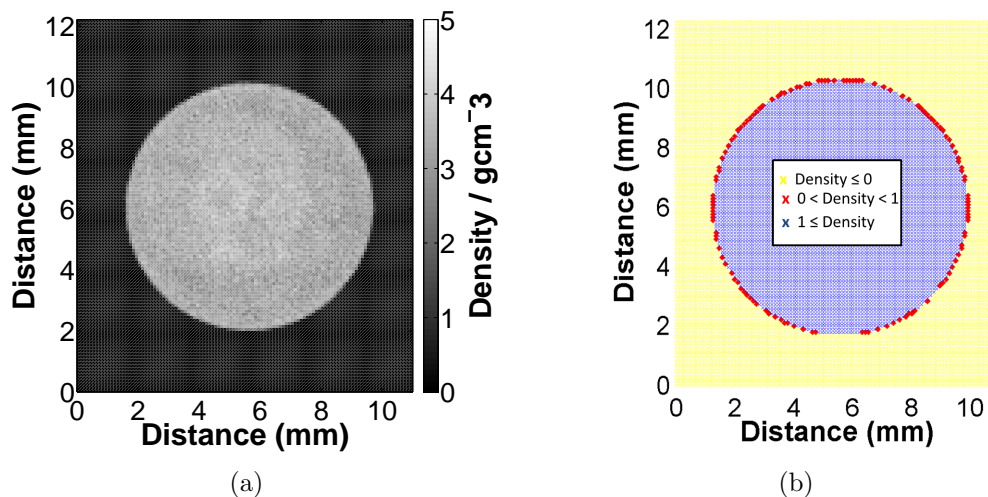


Figure 4.3: (a) Density colour map, and (b) its corresponding density map after thresholding, produced after the analysis of a phantom ($\text{Ca}(\text{H}_2\text{PO}_4)_2(\text{H}_2\text{O})$) CT slice for phantom volume and density calculations. The yellow and red voxels were rejected from further analysis.

DEA. The first step of CT-DEA provided results for the density of the phantoms. Threshold limits were applied to the density values of the CT-images to reject all background voxels and sample-edge voxels. The threshold density limits applied were; background: density $< 0 \text{ g/cm}^3$, phantom-edge: density = $0-1 \text{ g/cm}^3$ and phantom: density $> 1 \text{ g/cm}^3$. Density colour maps were plotted for each phantom. Figure 4.3 shows (a) a density colour map, and (b) its corresponding density map after thresholding, produced after the analysis of a phantom ($\text{Ca}(\text{H}_2\text{PO}_4)_2(\text{H}_2\text{O})$) CT slice. The yellow and red voxels were rejected from further analysis. The average density of each phantom was found using CT-DEA and was compared to the actual total density of the phantom (table 2.2).

Each phantom was decomposed using CT-DEA into its heaviest materials (maximum three), as described in table 2.2. The Ca/P ratio of a volume of 4.5 mm^3 ($32 \times 32 \times 5$ voxels), away from possible cracks and non-homogeneities, in each phantom was averaged for Ca/P ratio quantification. The CT-DEA Ca/P ratio results were compared to the expected Ca/P ratios of the phantoms (table 2.2).

4.3.2 Results: experimental precision

Plots of density colour maps of the five K_2HPO_4 solutions, with a resolution of $96 \mu\text{m}$, are shown in figure 4.4 at a given slice. All maps have the same colour scale to allow direct comparison. The higher the density in the phantom, the lighter the colour in the density maps.

Figure 4.5 shows the results of the densities of the five K_2HPO_4 solutions versus their CT-DEA measured densities. An overestimation of 0.01 g/cm^3 in the calcu-

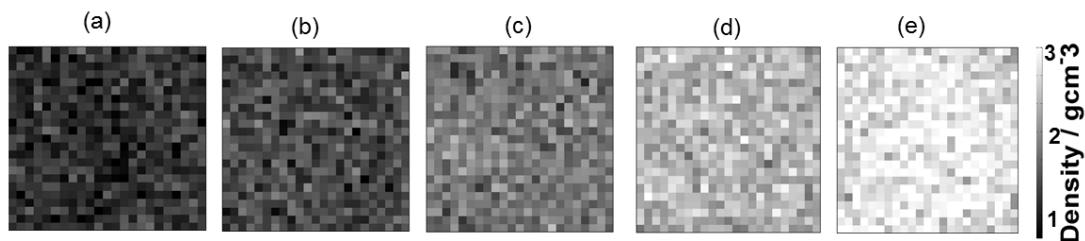


Figure 4.4: Density colour map plots extracted from five K_2HPO_4 solutions of known density of (a) 1.39, (b) 1.59, (c) 1.94, (d) 2.36 and (e) 2.68 g/cm^3 . All maps are $2.3\text{ mm} \times 2.3\text{ mm}$. Each voxel is $96\ \mu\text{m}^3$.

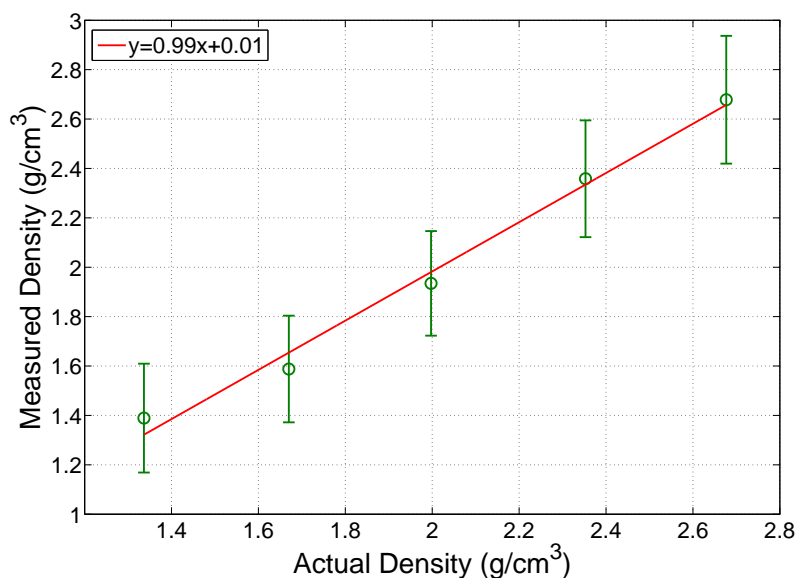
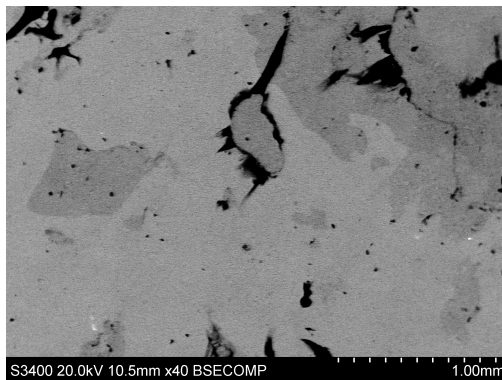


Figure 4.5: Experimental results. CT-DEA average density results of K_2HPO_4 solutions shown in green circles. The red line expresses the relation of a CT-DEA density result to the actual density of the sample. Error bars represent the standard deviation.

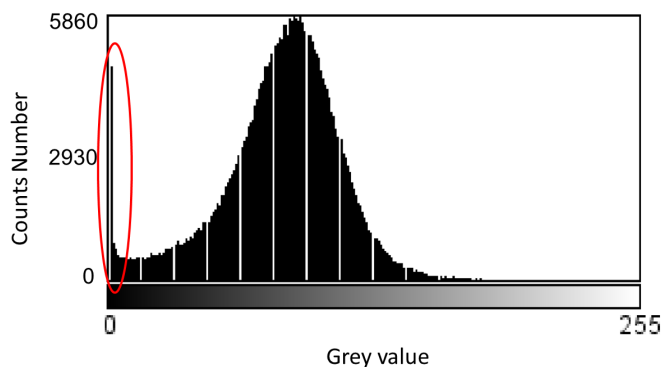
lation of density is made, with $R^2 = 0.99$. The mean/maximum precision of in the apparent density of the K_2HPO_4 solutions was $0.04/0.08\ \text{g}/\text{cm}^3$. Assuming perfect solubility of K_2HPO_4 powder in water, with no non-uniformities in its distribution, the standard deviation reflects the noise in the the low and high energy microCT images, propagated in density.

The experimental results of the bulk density of bone phantoms were plotted versus their total densities (figure 4.7). The coefficient of determination, calculated using linear regression analysis, is equal to $R^2 = 0.88$, for a linear fit of points with a gradient of 0.98 and a y-intercept of 1.08.

The explanation of the $1.08\ \text{g}/\text{cm}^3$ offset is the presence of air pockets in the phantoms. When compressing the phantoms it is difficult to remove all air pockets, between powder granules. The presence of air in the phantom is shown in the histogram of the grey values from a backscatter electron image of a phantom



(a)



(b)

Figure 4.6: (a) SEM backscatter image of a phantom ($\text{CaHPO}_4 \cdot 2(\text{H}_2\text{O})$), and (b) the histogram produced for the whole surface. The peak at ~ 0 grey value shows the presence of air.

($\text{CaHPO}_4 \cdot 2(\text{H}_2\text{O})$) surface, acquired using the SEM system (figure 4.6).

The impact the presence of air has, is explained as follows. The grey value of the system was calibrated with a liquid (K_2HPO_4 solutions), which assumes there are no air pockets. It only considers the amount of attenuating material present. In the calibration procedure, the grey value, changed only when the amount of attenuating material changed, with no consideration of air. When a phantom containing air is imaged, the grey value is lower, therefore the estimations of $\mu(Z_{\text{eff}}, \rho_{\text{eff}}, \text{L})$ and $\mu(Z_{\text{eff}}, \rho_{\text{eff}}, \text{H})$ are underestimated. At a lower energy, $\mu(Z_{\text{eff}}, \rho_{\text{eff}}, \text{E})$ is more affected by the presence of air, so $\mu(Z_{\text{eff}}, \rho_{\text{eff}}, \text{L})$ is underestimated more than $\mu(Z_{\text{eff}}, \rho_{\text{eff}}, \text{H})$. Therefore, $F(Z_{\text{eff}})$ is underestimated. This leads to an underestimation of Z_{eff} and \bar{m}_E . Density is calculated as $\mu(Z_{\text{eff}}, \rho_{\text{eff}}, \text{E})/\bar{m}_E$, both of which are underestimated, but in equal proportions. As such, density is almost unaffected by the presence of air, if air proportion is less than 15% by weight (case of cortical bone). This conclusion was validated in a simulation with different weight proportions of air in a given voxel, with results in table 4.2. This shows that for a bone of (material) density $\sim 1.9 \text{ g/cm}^3$, the deviation from the expected density increases, with the proportion of air increasing in the voxel. For a weight fraction of air less than 15%

Table 4.2: Simulation results. Deviation from expected density with different weight proportions of air in a given voxel of bone.

Air proportion (%)	Density error (%)
15	5.08
30	7.88
50	13.87

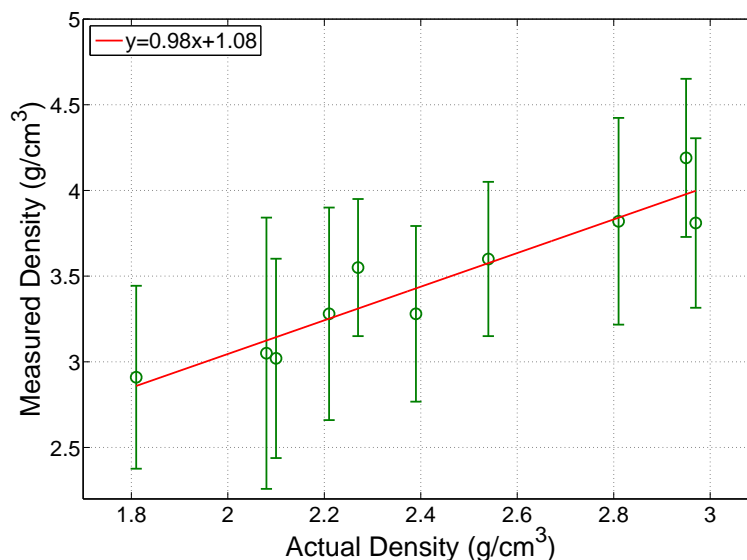


Figure 4.7: Experimental results. CT-DEA average density results of bone phantoms shown in green. The red line expresses the relation of a CT-DEA density result to the actual density of the sample. Error bars represent the standard deviation.

the density is within 5%.

The CT-DEA density represents the density of the attenuating material only, as detailed in section 1.4.1. So, in the phantom studies, where the granules have not been packed sufficiently well, the relevant volume in the CT-DEA density measurement is the volume of the granules only. This lower volume produces a higher density than the total density of the phantom.

Plots of Ca/P ratio maps of four phantoms, of different Ca/P ratio, with a resolution of $96 \mu\text{m}$, are shown in figure 4.8 at a given slice. All maps have the same colour scale to allow direct comparison. The higher the Ca/P ratio in the phantom, the lighter the colour in the Ca/P ratio maps.

The expected results of Ca/P ratio for all ten phantoms are plotted versus the measured average values in figure 4.9. The average Ca/P ratio results of the ten samples show a mean/maximum deviation from the expected of 0.24/0.35. As discussed above, this is low enough to distinguish between some, but not all, healthy and osteoporotic bone samples. The coefficient of determination, calculated using linear regression analysis, is equal to $R^2 = 0.92$, for a linear fit of points with a gradient of 1.14 and a y-intercept of -0.36.

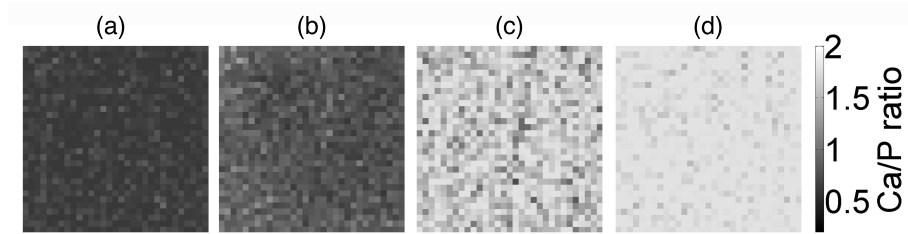


Figure 4.8: Ca/P ratio maps plots extracted from phantoms of known Ca/P ratio of (a) 0.5, (b) 1.0, (c) 1.5 and (d) 1.67. All maps are $3\text{ mm} \times 3\text{ mm}$. Each voxel is $96\ \mu\text{m}^3$.

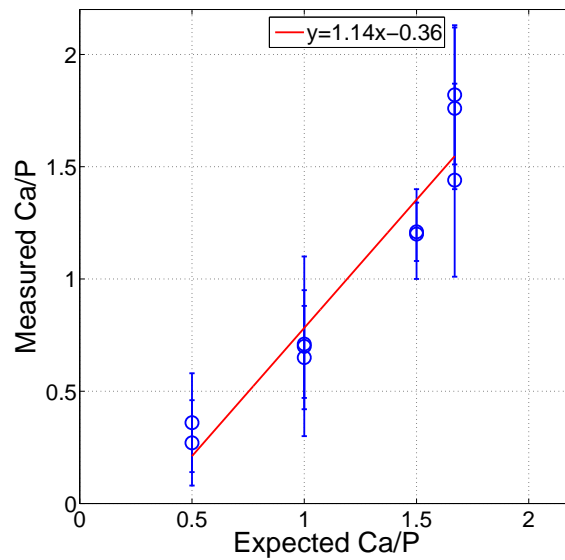


Figure 4.9: Experimental results. Phantom CT-DEA average Ca/P ratio results shown in blue circles. The red line expresses the relation of a CT-DEA density result to the actual density of the sample. Some samples had similar/identical results, therefore they overlap of the graph: there are two results at 0.70 and 0.71, and two results at 1.21. Error bars represent the standard deviation.

The increased error in the experimental results compared to the simulated results could be due to an error in the measured CT numbers and thus in $\bar{\mu}(E, \rho_{\text{eff}}Z_{\text{eff}})$. CT systems of increased power and more efficient detectors might allow different optimum imaging conditions and thus higher accuracy in results. The X-Tek reconstruction algorithm is expected to be trivial as it is part of the trivial error found in the CT grey value calibration (3.6.2). A possible source of error in the Ca/P ratio is an error in the expected Ca/P ratio due to the uncertainty of maximum 15% in chemical formula of the phantoms (table 2.2).

4.4 Evaluation of CT-DEA performance for Ca/P ratio assessment in bone apatite

Further to the evaluation of the precision of CT-DEA using bone phantoms there was the requirement to assess its precision when used on real bone apatite. However, unlike a bone phantom, the variation of the value and distribution of the Ca/P ratio in a bone is unknown. Therefore, Ca/P ratio measurements made using the developed technique were compared to measurements made using EDX, which is regularly used for Ca/P ratio measurements on bone surfaces (Kourkoumelis et al. [2011]).

SEM (section 2.3) was used to determine the composition of areas of interest in eight (four healthy and four IMO) rabbit tibia cortical bone samples (set 1a, table 2.4). The Ca/P ratios of these areas were calculated and were compared to the Ca/P ratios of the same areas found using CT-DEA.

In this section, the methods of the experiments are described and the results and presented and discussed.

4.4.1 CT sample imaging and CT-DEA analysis

The eight collagen-free bone samples were imaged using the microCT system (section 2.2.3) at the same conditions, and processed in the same way, the phantoms in section 4.3 were imaged and processed.

By analysing all acquired images using CT-DEA (section 2.4.4), 2D Ca/P ratio colour maps were produced for all slices in all samples, to allow visual differentiation of areas of low and high Ca/P ratio (figure 4.10). A total of 58 regions of interest (ROIs) from all the sample surfaces, that covered a wide range of Ca/P ratio, were selected for validation using Energy Dispersive X-ray Spectroscopy (EDX). The average Ca/P ratio for each ROI was calculated.

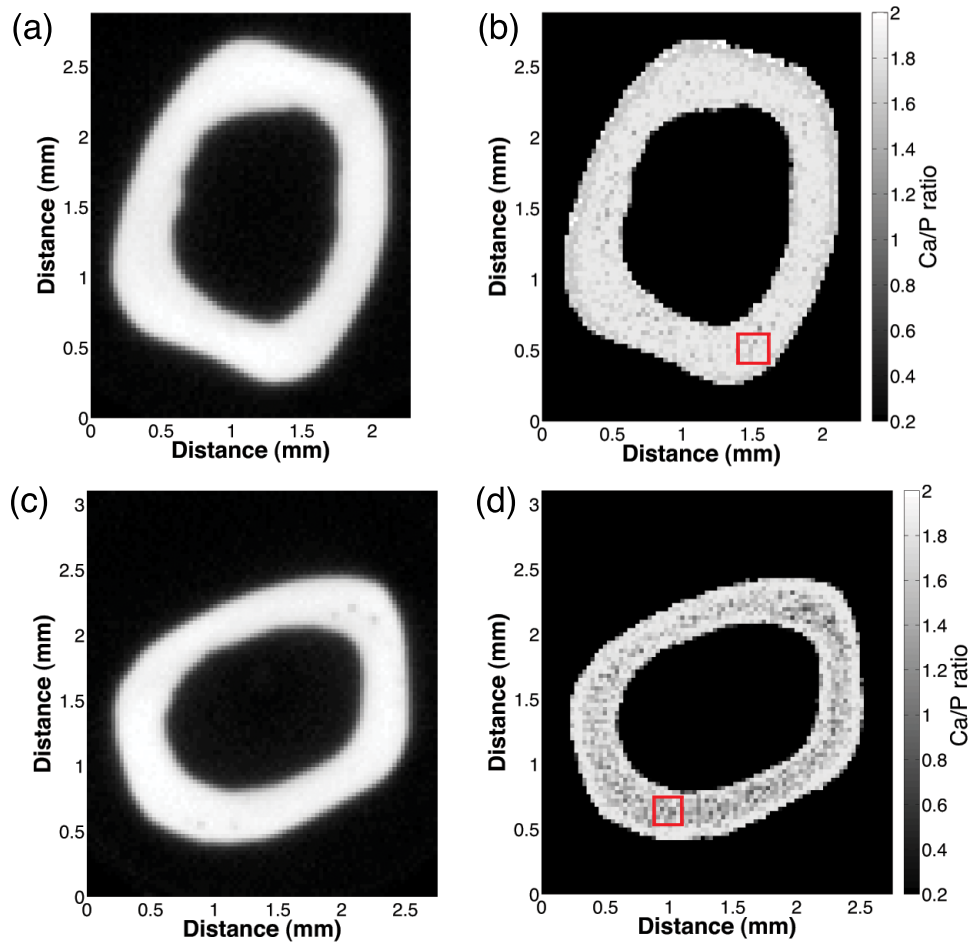


Figure 4.10: Original low energy CT images ((a) and (c)) and the corresponding Ca/P ratio 2D maps ((b) and (d)) for rear tibia rabbit bone samples. The samples are healthy ((a) and (b)) and IMO ((c) and (d)). The selected areas represent ROIs in the samples.

4.4.2 SEM sample imaging and EDX analysis

The eight collagen-free bone sample surfaces were imaged using a scanning electron microscope system (Hitachi model S-3400N, Japan); serial number: 340621-04. The imaging conditions for all samples were: 20 Volts, emission current 128 μA and magnification $\times 27$. At the same conditions, three bone phantoms (section 2.5.2) of different, known Ca/P ratio were imaged for the validation of EDX measurements.

Backscatter SEM image of the surface of interest in each bone phantom and sample was acquired. The regions of interest (ROIs) of each bone surface, as selected on the Ca/P ratio colour maps, produced using CT-DEA, were identified on the SEM backscatter images.

The chemical composition information of the ROIs was accomplished by a ‘selected area analysis’. The electron beam was stopped and positioned on the ROI, which had been selected (in a rectangle) on the SEM screen, while the image was still being displayed. The spectrum of the selected area was produced by the software, together with a table showing quantitative information of the sample composition. Finally, results for the atomic Ca/P ratio were produced using

$$\text{Ca/P} = \frac{\alpha_{Ca}}{\alpha_{PO_4}} \quad (4.1)$$

where α_{Ca} and α_{PO_4} are the atomic fraction of Ca and P respectively.

4.4.3 Image registration and analysis

For a more accurate mapping of the CT-DEA Ca/P ratio map to the SEM image, image registration was performed. This is a process of transforming different sets of data into one coordinate system. NifTK, a translational imaging platform, developed at the centre for medical image computing (CIMIC) of University College London, was used. In particular, NiftyReg software package was used via the viewer NiftyView. NiftyReg contains programs to perform rigid, affine and non-linear registration of medical images. NiftyView is a cross platform graphical user interface, providing an entry point to NifTK packages, and in addition, many of the usual features one would find in any medical image viewer.

The Ca/P ratio map image and the SEM image of the same sample produced from the two imaging systems were of different magnification, pixel size and sometimes orientation. Initially, manual mapping was required for the two images. The necessary scaling, rotation and translation amendments were made to the CT-DEA Ca/P ratio map image until its geometry mapped sufficiently well on top of the SEM image. In the next step, the images were mapped more precisely by Nifty software (figure 4.11).

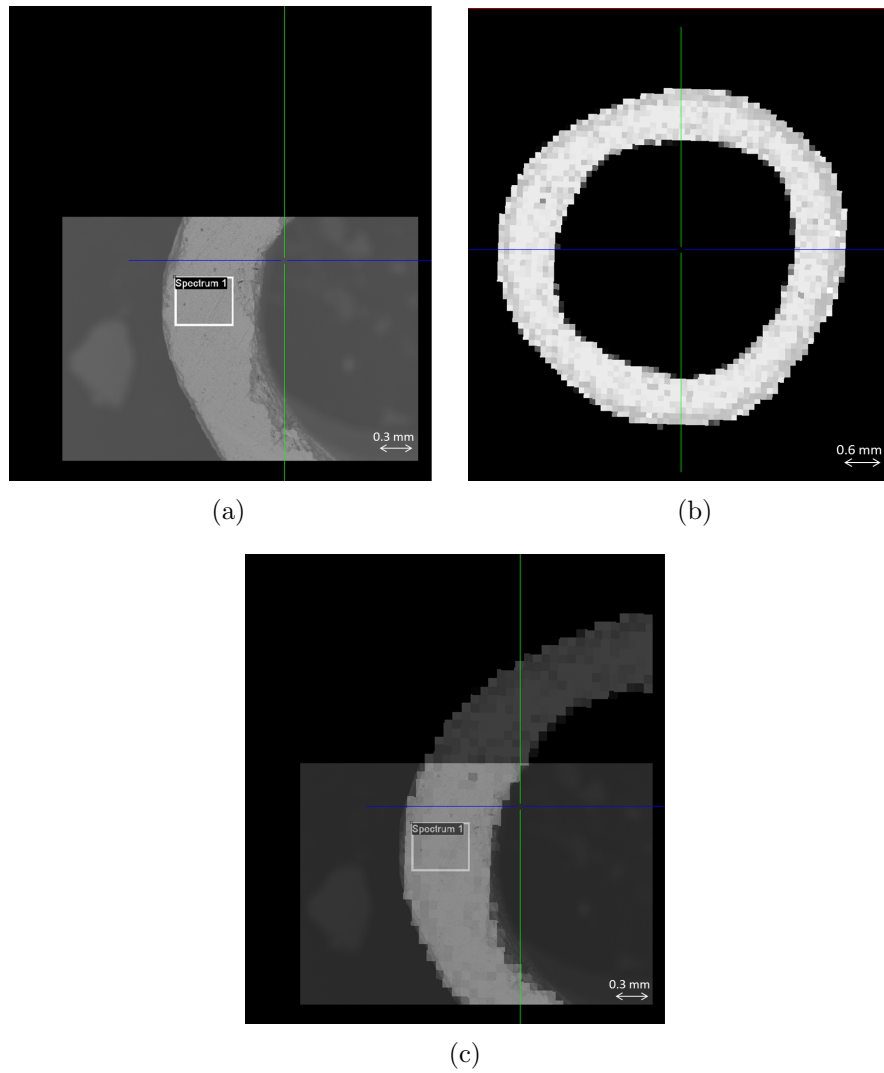


Figure 4.11: (a) Backscatter SEM image, (b) CT-DEA Ca/P ratio colour map of the surface of an IMO bone sample. The mapping of the two images in NifTK is shown in (c).

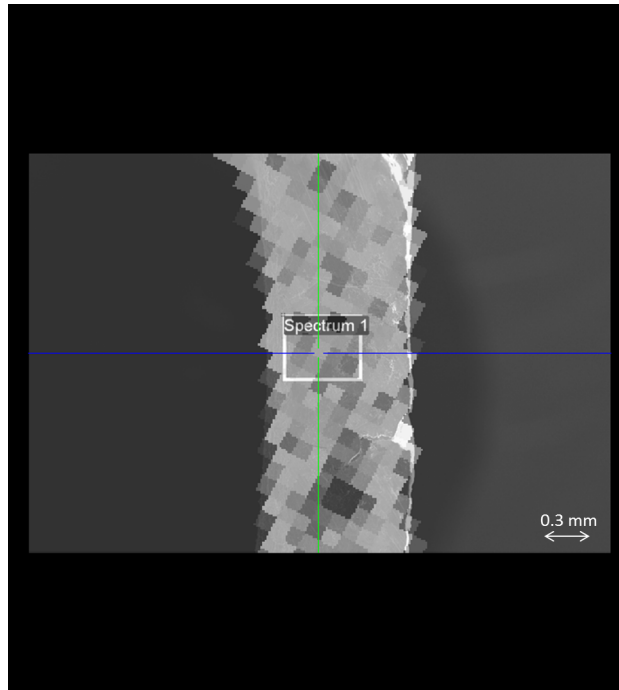
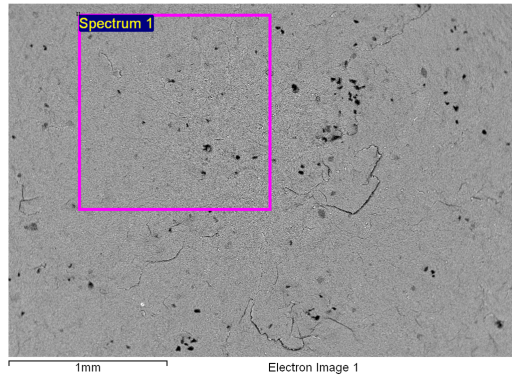


Figure 4.12: A case where there was a misalignment of the pixels of CT image to the pixels of the SEM image, due to the different orientation of the sample to the detector in the two systems.

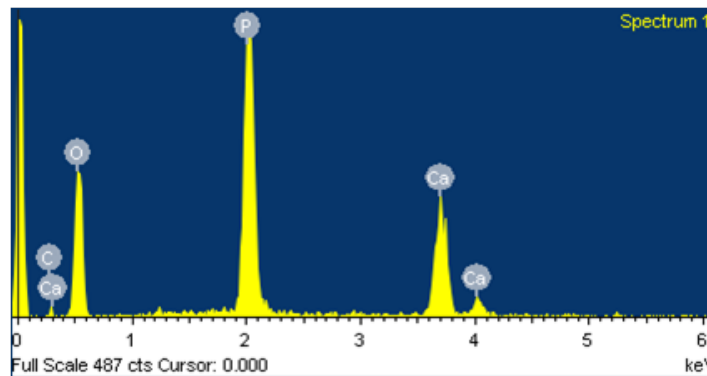
Image registration reproduced the CT-DEA Ca/P ratio map with the grey values of the original CT-DEA Ca/P ratio map image and the SEM pixel size and coordinates. The coordinates of each ROI were determined on the registered Ca/P ratio map image and the corresponding coordinates were found on the original Ca/P ratio map. The average Ca/P ratio by CT-DEA of the ROI was calculated.

In some cases, the coordinates of the CT-DEA Ca/P ratio map registered image were only an approximation to the CT-DEA Ca/P ratio map original image (figure 4.12). This was due to the different alignment of the pixels with respect to the sample, which resulted from the different orientation of the sample to the detector in the two imaging systems. In these cases, the selection of the CT Ca/P ratio map original image ROI coordinates was made such that it includes all the pixels falling within ROI, plus the minimum number possible extra pixels around it.

The eight sample images were analysed, giving a total of 26 ROIs from four healthy bone samples and 32 ROIs from four IMO bone samples. The average Ca/P ratio of the ROIs was compared to the corresponding SEM Ca/P ratio, using linear regression analysis. Furthermore, a two-sample Student's t-test was used to investigate the statistical significance in the difference of the Ca/P ratios of the healthy and IMO areas, using the two different techniques. For the Student's t-test a one tail normal distribution and unequal variance were assumed for the Ca/P ratio of the samples.



(a)



(b)

Figure 4.13: (a) SEM backscatter image, with a selection of the ROI, and (b) its corresponding EDX spectrum, acquired using a bone phantom of Ca/P ratio = 0.5.

4.4.4 Results: Areal Ca/P ratio assessment using EDX

Three bone phantoms were used for the validation of the EDX Ca/P ratio assessment. A typical example of an SEM backscatter bone phantom (of Ca/P ratio = 0.5) image is shown in figure 4.13(a), with a selection of the ROI. Its corresponding spectrum, is shown in figure 4.13(b). The height of the peaks in the spectrum is proportional to the atomic fraction of each element present in the sample. The presence of Calcium, Phosphorus and Oxygen can be observed as expected. Carbon is also present in this sample spectrum, same as in all other phantom spectra. This is probably due to residual carbon in the SEM system from earlier coated samples, carbon contamination of the sample or from carbonates present in the sample.

The precision in the assessment of f_{Ca} , f_P in phantoms, by EDX, is shown in figure 4.14. In all phantoms f_P was overestimated more than f_{Ca} . A possible reason for this is fluorescence. X-rays or high energy electrons emitted from the sample may subsequently hit other areas of the sample and excite X-rays by fluorescence from these regions. Fluorescence is one of the effects which make accurate quantitative analysis difficult. It is not a very efficient process, since only a few per cent of

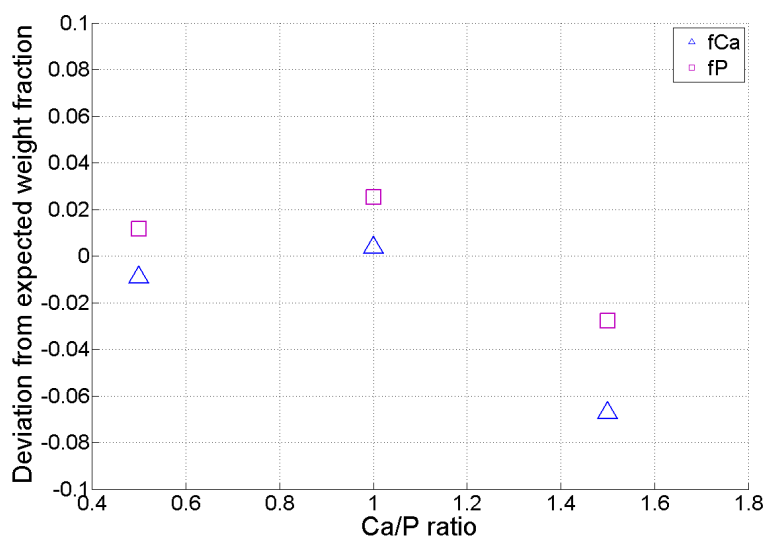


Figure 4.14: EDX measurements. Deviation from the expected f_{Ca} (blue triangles) and f_P (pink squares) for phantoms of different Ca/P ratio.

the higher energy rays will successfully excite the lower energy radiation. However, it may significantly alter the relative amounts of characteristic radiation coming from alloys or compounds, particularly when elements with quite similar atomic numbers are present ($P = 15$, $Ca = 20$) (Goodhew et al. [2001]). For example, in a bone phantom the Calcium K_α X-rays (energy 4.04 keV) can excite extra Phosphorus K_α X-rays whose energy is less (2.15 keV). This produces misleading analysis. Fluorescence is particularly important for rough samples (Goodhew et al. [2001]).

The errors in f_{Ca} and f_P are propagated into the calculation of the Ca/P ratio. Due to an overestimation f_P in comparison with f_{Ca} , an underestimation is always made on the calculation of the Ca/P ratio, resulting in a mean/maximum precision of -0.07/-0.11 to the Ca/P ratio (figure 4.15). The correlation of the measured to the expected Ca/P ratios gave an $R^2=0.96$, reflecting a high confidence in the Ca/P ratio calculation by the SEM system.

Figure 4.16 shows an example of a backscatter SEM image of one bone sample and the ROIs selected on it. Figure 4.17 shows examples of the spectra acquired from (a) a healthy bone sample and (b) an IMO bone sample. EDX shows the presence of the chemical components in the sample; Calcium, Phosphorus, Carbon, Oxygen, Magnesium and Sodium are all expected to be present in bone apatite (table 1.1).

The Ca/P ratio in a healthy bone apatite is expected to be around 1.67. The Ca/P ratio results in healthy bone samples using EDX were within the range of 1.39-1.62. This underestimation of Ca/P ratio by the SEM system is not surprising since, as shown by the bone phantom results of EDX, f_P is overestimated due to fluorescence. Bone samples Ca/P ratio underestimation is higher than the underes-

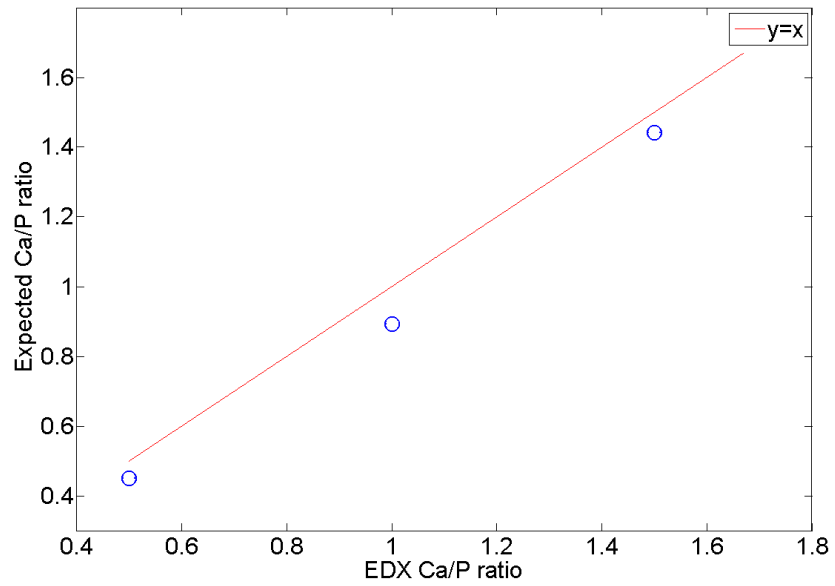


Figure 4.15: Experimental results. Expected phantom Ca/P ratio versus EDX-measured average Ca/P ratio. The red line expresses the expected relationship.

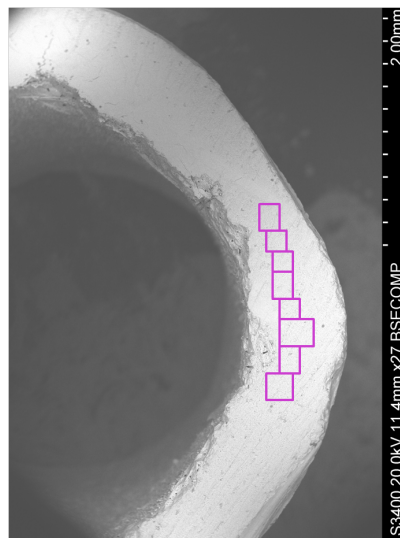
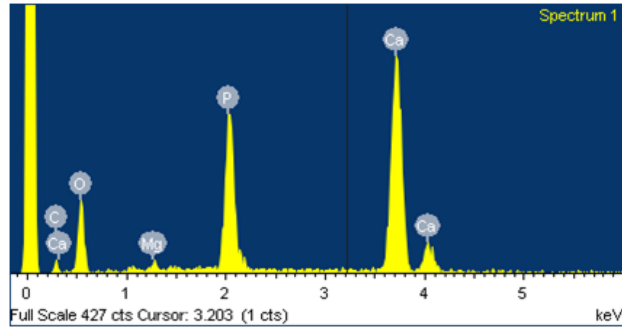
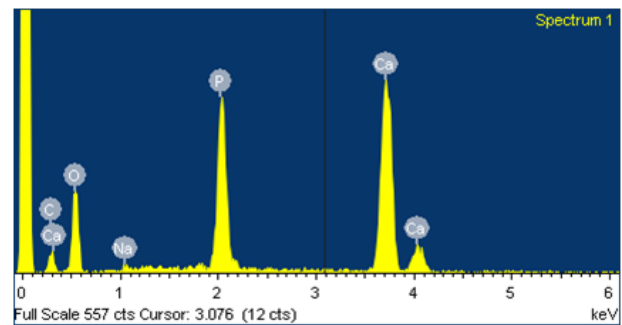


Figure 4.16: SEM backscatter image of a healthy bone sample. The rectangular selections represent the selected areas analysed in this sample.



(a)



(b)

Figure 4.17: Examples of the spectra acquired from (a) a healthy bone sample and (b) an IMO bone sample.

timation made in phantoms. This is possibly due to the more rough surfaces of the bone samples, compared to bone phantoms, causing increased fluorescence and thus f_P overestimation.

Another possible reason for observing Ca/P ratio values lower than 1.67 ratio is the non-perfectly uniform mineralised bone. Ca and PO_4 move where they are needed in the body. For example, carbonate groups replace a fraction of phosphates and/or hydroxyl groups in the mineralised hydroxyapatite ($Ca_{10}(PO_4)_6(OH)_2$), thus varying its crystallinity (Wilson et al. [2005], Pasteris et al. [2008], Wopenka and Pasteris [2005]), which depends on the stage in the mineralisation process and age (Rauch and Schoenau [2001]). In IMO bone samples the Ca/P ratio range (1.20-1.52) was lower than the healthy samples Ca/P ratio range.

Comparing the difference of the Ca/P ratios of the healthy and IMO areas, using a Student's t-test, a p-value of < 0.05 (table 4.3) was given. From this it can be concluded that there is a statistically significant difference in the Ca/P ratios of the healthy and IMO bone sample areas. These results are in agreement with other studies, where a statistically significant difference was found in the Ca/P ratio between healthy and IMO bones (Tzaphlidou et al. [2005], Kourkoumelis et al. [2011]).

4.4.5 Results: CT-DEA performance for Ca/P ratio assessment in bone apatite

The Ca/P ratio results using CT-DEA were within the range of 1.43-1.77 and 1.24-1.59 (y-axis of plot in figure 4.18) for healthy and IMO bone samples respectively. Comparing with the EDX results; 1.39-1.62 for healthy samples and 1.20-1.52 for IMO samples, it can be concluded that an overestimation is made by CT-DEA. This systematic error is due to the approximations used for the $F(Z_{\text{eff}})$ to Z_{eff} and Z_{eff} to \bar{m}_L relations as discussed in section 4.2.

CT-DEA gave correct Ca/P ratio values within an average deviation from the EDX Ca/P ratio of 0.11 ± 0.08 ($8 \pm 6\%$ deviation of the CT-DEA 58-regions average Ca/P ratio from the EDX 58-regions average Ca/P ratio). Linear regression analysis in the plot of CT-DEA Ca/P ratio results versus EDX Ca/P ratio results of the same areas, provided the value for the coefficient of determination; $R^2 = 0.69$. This means that 69% of the samples express a linear relation between the CT-DEA Ca/P ratio to EDX Ca/P ratio of gradient 1.17 and y-intercept of -0.13.

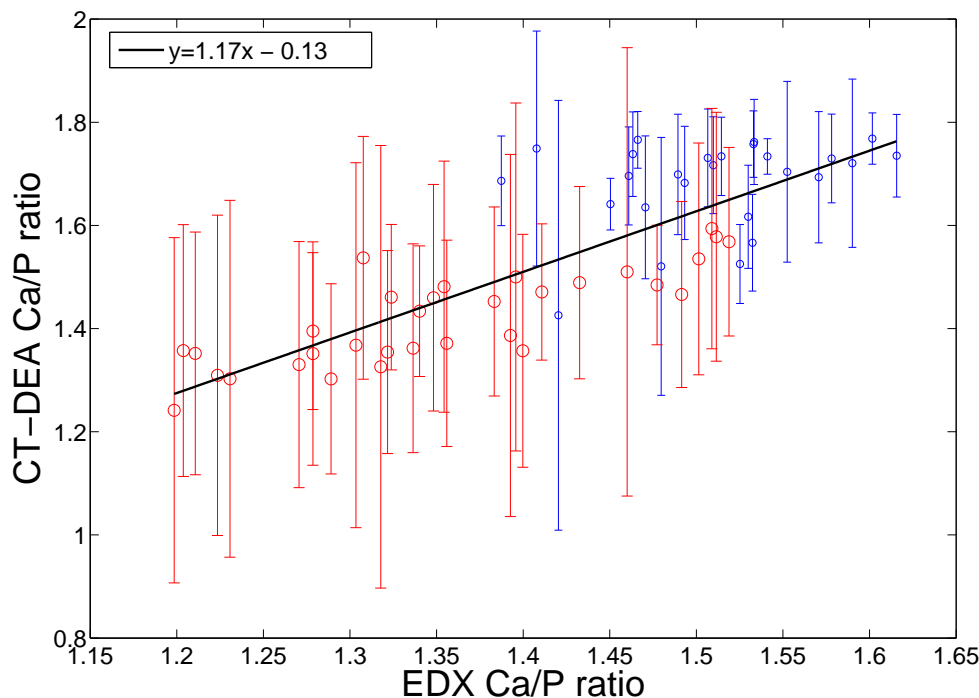


Figure 4.18: CT-DEA Ca/P ratio versus EDX Ca/P ratio of 58 regions of interest in 8 samples; 4 healthy (blue) and 4 osteoporotic (red).

The noise in CT-DEA low and high energy images, introduces an error in the Ca/P ratio results. This error partly expresses the error bars in figure 4.18. The error bars magnitude is also expressed by the non-homogeneities of Ca/P ratio in bone. As can be observed on the graph, in IMO bone sample areas (red) the variation of

Ca/P ratio is larger than that in healthy bone areas (blue). This suggests a higher non-homogeneity of Ca/P ratio in IMO areas, which agrees with previous studies (Tzaphlidou et al 2005).

The results of the precision of CT-DEA of Ca/P ratio measurements in bone apatite were very dependent on the successful mapping of the images from the two imaging systems. Therefore, one of the causes of the lack of 0.31 in the coefficient of determination of the plot in figure 4.18, is the non-perfect mapping of the images. It was not possible to evaluate the error the non-perfect mapping introduced on the CT-DEA precision calculation. In addition, it is unknown to what sample depth the EDX Ca/P ratio results correspond to. The volume which is being analysed, and the fraction of the X-rays which are emitted from the sample depend critically on (a) the energy of the electron beam, (b) the energy (wavelength) of the X-rays being studied and (c) the local atomic weight of the sample. Therefore, it was difficult to predict the depth of X-ray interaction in EDX and compare it with the CT-DEA X-ray interaction depth (96 μm). If the interaction depths were different in the two systems, their results are expected to be different.

Table 4.3 shows the results of a Student's t-test on the assessment of the statistical significance the two imaging systems can provide in distinguishing healthy and IMO areas in bone apatite. Both systems show that they can differentiate a healthy from an IMO bone sample, with a statistical significance (defined as $p < 0.05$). CT-DEA p-value is sufficiently low to distinguish the same healthy and IMO areas that EDX does.

Table 4.3: Details of collagen-free bone samples.

Variable	SEM		CT	
	Healthy	IMO	Healthy	IMO
average	1.51	1.36	1.68	1.42
Observations	26	32	26	32
p-value	<0.0001		<0.0001	

In conclusion, due to the undetermined uncertainties introduced in the analysis by fluorescence in EDX, image mapping and depth interaction of electrons, it cannot be concluded to what absolute precision the Ca/P ratio can be measured in real bone apatite using CT-DEA. However, a value of $R^2=0.69$ in the fit of CT-DEA Ca/P ratio versus EDX Ca/P ratio and an average difference in the Ca/P ratio between the two techniques of 0.11 ± 0.08 suggests sufficient confidence in the experimental capabilities of the developed technique.

CT-DEA compared with the EDX method has the advantage of non-invasively assessing a bone sample in 3D. The 3D capabilities of the technique will be presented and discussed in the next chapters.

4.5 Summary

The evaluation of CT-DEA for the quantification of density and Ca/P ratio was performed using bone phantoms and bone samples.

In a simulation of the developed technique on bone phantoms, the theoretical density and Ca/P ratio mean/maximum accuracy were found to be 0.01/0.03 g/cm³ or 3.71%/1.14%, and 0.10/0.28 or 14.21%/45.00% respectively. These errors are the result of the uncertainty of the relations of $F(Z_{\text{eff}})$ to Z_{eff} and Z_{eff} to \bar{m}_L used in CT-DEA.

In the experimental application of CT-DEA on bone phantoms, of known density and Ca/P ratio, concluded on a mean/maximum precision of in the apparent density of the sample of 0.04/0.08 g/cm³ and a mean/maximum precision of 0.24/0.35 in the Ca/P ratio assessment. The increased error compared to the theoretical accuracy is a result of the uncertainty in the grey value and in the reconstruction of the microCT low and high energy images, as well as in the uncertainty of the actual chemical composition of the samples. This accuracy would be enough to distinguish between some, but not all, healthy and osteoporotic bone samples.

The Ca/P ratio in 58 bone sample surfaces, from four healthy and four IMO bone collagen-free samples were assessed with EDX and CT-DEA and compared. A value of $R^2=0.69$ in the fit of CT-DEA Ca/P ratio versus EDX Ca/P ratio and an average deviation of 0.11 ± 0.08 ($8\pm 6\%$) from the EDX results in the CT-DEA Ca/P ratio suggests sufficient confidence in the experimental capabilities of the developed technique. The sources of this error is the imperfect mapping of the images from the two imaging systems, as well as an uncertainty in CT-DEA and EDX Ca/P ratio calculation.

Chapter 5

Density and Ca/P ratio assessment in healthy and osteoporotic cortical bone apatite

5.1 Overview

In this chapter the results of the application of CT-DEA on bone apatite are presented.

Set 1 samples (table 2.4), eighteen collagen-free healthy (nine) and inflammation-mediated osteoporotic (nine) rabbit bone samples were imaged using the microCT system and analysed using CT-DEA. The density and Ca/P ratio results of the two bone types were compared to investigate the difference in magnitude and distribution of density and Ca/P ratio in healthy and IMO bones. A secondary aim was to investigate different analysis methods, providing different density and Ca/P ratio parameters, in a given set of data. In this chapter the quantitative and qualitative results of different analysis methods, of set 1 samples, as well as their statistical analysis are presented and discussed.

In section 5.2, information on the experimental and analytical methods is provided. In section 5.3 the results of different density and Ca/P ratio parameters in the bone samples are presented. Bulk density and bulk Ca/P ratio results are shown. Slice by slice density and Ca/P ratio maps and 3D Ca/P ratio maps are presented, together with quantitative analysis of density and Ca/P ratio. Statistical analysis on the comparison of the different density and Ca/P ratio parameters between healthy and IMO bone samples are presented. In section 5.4, comparison is made between the density and Ca/P ratio parameters in different bone sites. In section 5.5, statistical analysis of each bone site separately are shown. In section 5.6, a summary of the chapter is given and the advantages and disadvantages of

the different analysis methods of density and Ca/P ratio, in collagen-free bone are discussed. Conclusions are made on how the magnitude and distribution of density and Ca/P ratio in cortical bone apatite, change in osteoporosis.

5.2 Experimental methods

5.2.1 Collagen-free bone imaging

Set 1, cortical collagen-free rabbit, nine healthy and nine IMO bone samples (table 2.4) (three rear tibiae (RT), three femurs (F) and three front tibiae (three FT) for each bone type) were prepared as described in section 2.5.3. All 18 bone samples were imaged using the microCT system (section 2.2.3) at the optimum imaging conditions found (table 3.3). CT reconstruction was performed on the images using the in-built X-Tek software (Nikon Metrology, X-Tek, United Kingdom) at a slice thickness of $16 \mu\text{m}$. Any centre of rotation artefacts were corrected using CT Pro software (Nikon Metrology, X-Tek, United Kingdom) (section 2.2.3). Figure 5.1 shows a typical low-energy CT image of one rear tibia healthy bone sample, of cortical wall thickness $\sim 1\text{mm}$ and length $\sim 8\text{mm}$.

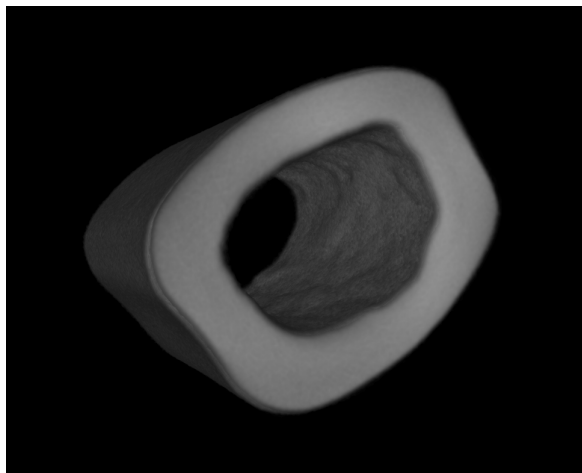


Figure 5.1: A typical 3D image of one healthy rabbit rear tibia bone sample, acquired using the microCT system.

The microCT system grey values were converted to $\bar{\mu}_L$ and $\bar{\mu}_H$, using the calibration equations (section 3.6.2). Finally, all phantom images were binned into $6 \times 6 \times 6$ voxels, thus providing a resolution of $96 \mu\text{m}$ in all dimensions. CT-DEA (section 2.4.4) provided simultaneous results on the density (bone material density, section 1.4.1) and Ca/P ratio for each voxel in the sample images. The different methods of analysis performed are described in detail in the next section.

5.2.2 Qualitative and quantitative analysis

CT-DEA was used to provide qualitative and quantitative information for healthy and IMO bone samples. For qualitative analysis, 2D and 3D colour maps of density and Ca/P ratio for all samples were produced, which allowed visual differentiation of possible healthy and IMO areas.

For quantitative analysis, density and Ca/P ratios were assessed in different volumes in the samples. Threshold limits were applied to the Ca/P ratio values of the CT-images to reject all background voxels and sample-edge voxels, subject to partial volume effect. The threshold Ca/P ratio limits applied were; background: Ca/P ratio ≤ 0 , sample-edge: $0 \leq \text{Ca/P ratio} < 1.00$ and bone sample: $1 \leq \text{Ca/P ratio} < 1.80$. There were no voxels with Ca/P ratio bigger than 1.80. Furthermore, low Ca/P ratio range was defined as 1.00-1.49, according to Fountos et al. [1999], who found that low Ca/P ratio in an osteoporotic or aged bone is expected to be in that range. Figure 5.2 shows (a) a Ca/P ratio colour map, and (b) its corresponding Ca/P ratio map after thresholding, produced after the CT-DEA analysis of an IMO rear tibia bone sample microCT slice.

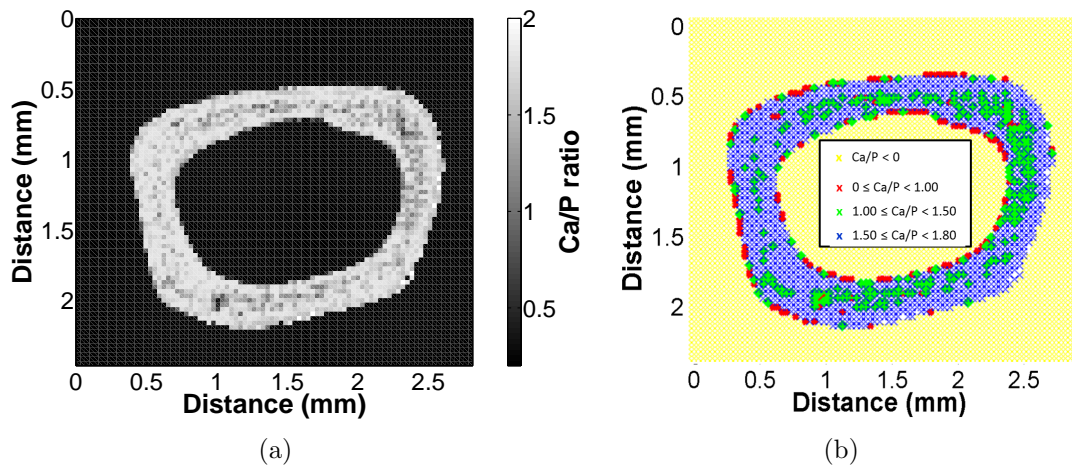


Figure 5.2: (a) Ca/P ratio map of a rear tibia bone sample, and (b) its corresponding Ca/P ratio map after thresholding. Yellow (Ca/P ratio ≤ 0) and red ($0 < \text{Ca/P ratio} \leq 1.00$) areas were rejected, while green ($1.00 < \text{Ca/P ratio} \leq 1.49$) and blue ($1.50 < \text{Ca/P ratio} \leq 1.80$) were used for bone analysis.

3D analysis allows the selection of regions of interest in the 3D volume. Different quantitative analysis methods of both density and Ca/P ratio were performed in different scales in all samples. Each analysis method provided the quantification of a different parameter. These are described below:

1. The average density and Ca/P ratio across the whole bone sample (volume varies between 61-172 mm³ in the 18 collagen-free bone samples). These parameters will be referred to as to as bulk density and bulk Ca/P ratio.

2. The average density and Ca/P ratio in volumes of possible healthy and osteoporotic regions, of volume 0.03 mm^3 ($6 \times 6 \times 1$ voxels), located using the density and Ca/P ratio maps.
3. The proportion of voxels with a low Ca/P ratio (1.00-1.49).
4. The interconnected-low Ca/P ratio proportion, quantified using a region growing technique. The region growing technique is a 3D image segmentation method, which was used to assess the distribution of low Ca/P ratio in the bone samples and identify the regions of interconnected-low Ca/P ratio. The region growing technique examined the neighbouring voxels of an initial seed voxel of low Ca/P ratio. Iteratively, all voxels within the Ca/P ratio range of 1.24-1.25 (the middle of the defined low Ca/P ratio range) were selected as the seed voxel. The region grew if the neighbouring voxels were in the range 1.00-1.49. The biggest region grown in each sample (by testing different seed voxels) was used for the quantification of the interconnected-low Ca/P ratio volume.
5. The degree of low Ca/P ratio homogeneity, defined as the ratio of the interconnected low Ca/P ratio volume to the low Ca/P ratio volume of the whole bone sample.

5.2.3 Statistical analysis

All the above listed parameters were compared between healthy and IMO bone samples. The Student's t-test was used to determine the significance of any differences of the studied parameters between all healthy and all IMO samples. Any differences in Ca/P ratio and density parameters between healthy and IMO bone samples would support the use of these parameters as possible osteoporosis indicators. For the Student's t-test a one tail normal distribution and unequal variance were assumed for the density and Ca/P ratio of the samples.

The Student's t-test was also used to study the difference of the studied parameters between different bone sites (rear tibia, femur, front tibia). The significance of this analysis lies in the context of comparing the density and/or Ca/P ratio parameters in one possible osteoporotic bone site to the corresponding healthy bone site, to diagnose osteoporosis. As discussed by Kanis and Glu [2000], the comparison between different bone sites for osteoporosis diagnosis should be avoided, since there is a biological and mechanical (Cowin [1984]) variability between sites. The reflection of this variability in density and Ca/P ratio parameters, was investigated in section 5.3 of this chapter.

Finally, the Student's t-test was used to analyse all the parameters, between healthy and IMO, in each bone site separately. A summary of the statistical analyses performed, using the Student's t-test, on all parameters of collagen-free bone samples, described in this chapter, is presented in table 5.1.

Table 5.1: Statistical analyses, using the Student's t-test, performed on the studied parameters of collagen-free bone samples (set 1) and their corresponding sections, where the results can be found.

Statistical analysis	Section
Difference in parameters between all healthy and all IMO	5.3
Difference in parameters between bone sites	5.4
Difference in parameters between healthy and IMO of different bone sites	5.5

5.3 Results: comparing healthy and IMO bones

5.3.1 Density and Ca/P ratio bulk results

Figure 5.3 shows the bulk density measurements, in g/cm^3 . The average density, across the whole sample, of the healthy bones (blue, filled circles) varies within the range 2.22-2.45 g/cm^3 . This range is realistic as it is within the range of ashed (at 600 °C) and hydrated hydroxyapatite density (2.05 g/cm^3) and ashed, non-hydrated hydroxyapatite density (3.20 g/cm^3) (Robinson [1975]). As shown by Robinson [1975] the density of ashed and hydrated bones varies with the degree of hydration.

In the IMO samples the bulk density results (red, open circles) varies within the range 1.93-2.33 g/cm^3 . Comparing the healthy with the IMO density results, it is clear that osteoporotic bone has on average a lower density than healthy bone. A decrease in bone density has also been observed with age (Wall et al. [1979]), a factor that contributes to the risk of fracture due to osteoporosis.

The Student's t-test was used to determine the significance of any differences between the bulk density of the healthy and IMO samples (table 5.2). A statistically significant difference, defined as $p < 0.05$, was thus found between the healthy and the IMO bone samples. This difference supports that osteoporosis affects the density of the apatite of the bone. This is in agreement with Wagner et al. [2011], who has shown that bone material density is related to Young's modulus and thus bone quality.

What is worth noting here, as well as in similar results in subsequent sections, is that the statistical significance found using the Student's t-test does not provide any information on the confidence in a single measurement. To obtain a confidence level

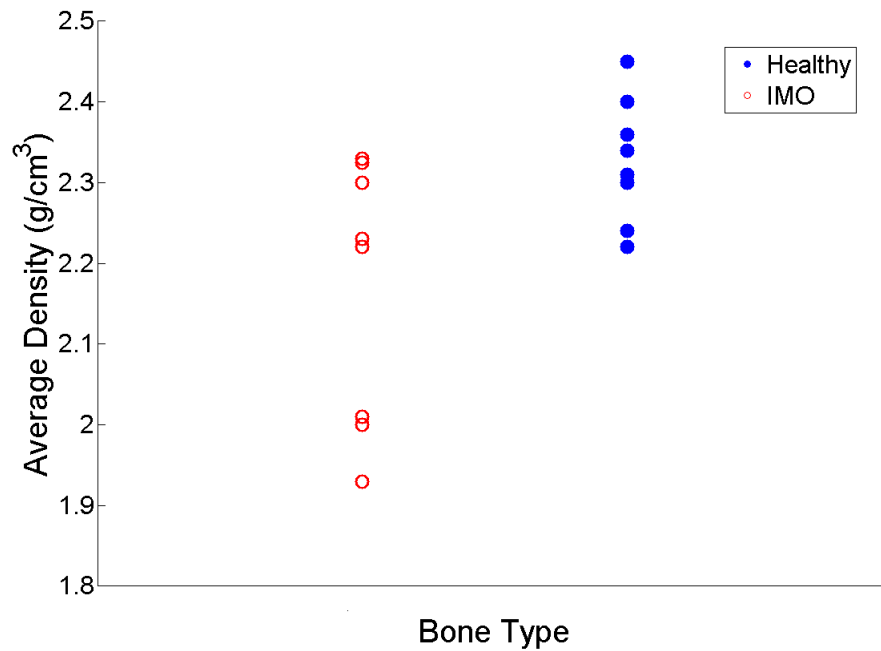


Figure 5.3: The bulk densities of 18 collagen-free bone samples, with healthy samples in red and IMO samples in blue, filled circles. Error bars have been excluded, for clarity, as the standard error <0.002 . Some samples had identical results: for IMO samples there are two results at 2.23; for healthy samples there are two results at 2.24.

Table 5.2: Student's t-test results of the bulk density and bulk Ca/P ratio, of the nine healthy and nine IMO bone samples.

Variable	Density (g/cm ³)		Ca/P ratio	
	Healthy	IMO	Healthy	IMO
Mean	2.32	2.18	1.67	1.66
Observations	9	9	9	9
p-value	0.0143		0.0250	

in a single measurement a bigger number of measurements is required as well as a threshold level in the density (or Ca/P ratio, for sections below) that will separate healthy and osteoporotic bone. The identification of a threshold level requires further studies in bones of different quality (strength). The number of samples should provide confidence in the distribution and variation of the density (or Ca/P ratio, for sections below) for a particular bone site.

Figure 5.4 shows the bulk Ca/P ratios of the collagen-free healthy (blue, filled circles) and IMO (red, open circles) bone samples. The average Ca/P ratios, of the healthy bones vary within the range 1.65-1.69. These results are within realistic limits, as the stoichiometric ratio gives Ca/P ratio = 1.67 for healthy bone hydroxyapatite (Tzaphlidou and Zaichick [2003]). Several authors have found Ca/P ratio results in the range 1.62-1.77 for non-collagenous and/or defated (ashed or acid-digested) bone: Aitken [1976]; Dickerson [1962] and Quelch, K et al. [1983] and Woodart [1964].

In the IMO samples the Ca/P ratio was slightly lower (1.63-1.68), also in agreement with previous studies (Tzaphlidou et al. [2005], Speller et al. [2005], Kourkoumelis et al. [2011]). A possible explanation of a lower Ca/P ratio is given by Zaichick and Zaichick [2010] and was discussed in section 1.4.2.

Table 5.2 shows the results for the statistical significance in the difference in the bulk Ca/P ratio of the nine healthy and nine IMO bone samples, determined using the Student's t-test. A p-value of 0.0250, confirms there is a statistically significant difference (defined as $p < 0.05$), supporting the use of Ca/P ratio in bone apatite as a possible osteoporosis indicator. As in the case of bone density, the Ca/P ratio measurement could be correlated to bone apatite quality, through its correlation to the Young's modulus of the bone apatite.

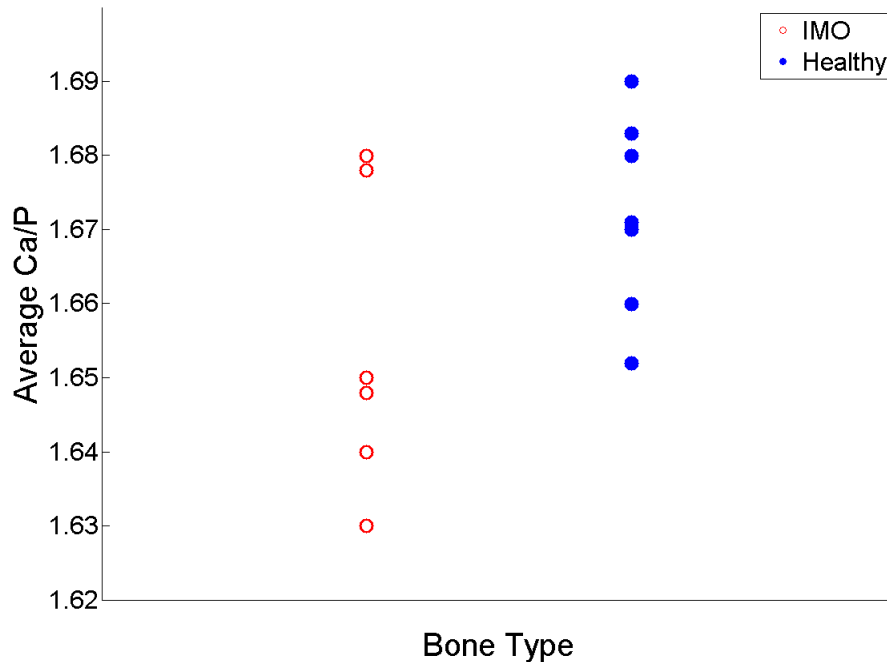


Figure 5.4: The bulk Ca/P ratios of 18 collagen-free bone samples, with healthy samples in red, open circles and IMO samples in blue, filled circles. Error bars have been excluded for clarity, as the standard error < 0.001 . Some samples had identical results: for IMO samples there are three results at 1.65 and two at 1.68; for healthy samples there are three results at 1.67.

Bulk density and Ca/P ratio measurements are easy to perform and are representative of the whole bone sample. The disadvantage of the bulk measurements is that the signal from the low Ca/P ratio areas is 'washed out', therefore no information is provided on where the osteoporotic regions are located.

5.3.2 Density and Ca/P ratio in volumes of interest

The main advantage of a CT image is the ability to visualise a volume. The additional advantage provided of a quantified CT image is the volume quantification. Slice-by-slice CT-DEA analysis can provide useful qualitative and quantitative results.

Going through the slices of the density and Ca/P ratio colour maps of the bone samples, possible osteoporotic areas can be visually identified. The effect of ρ_{eff} and Z_{eff} on $\bar{\mu}_L$ and $\bar{\mu}_H$, is decomposed. This is not possible to achieve using the original low and high energy microCT images. Figure 5.5 shows the (a) high energy and (b) low energy images from a single microCT slice of a collagen-free, IMO, rabbit rear tibia bone sample. The osteoporotic areas are not immediately obvious. The CT-DEA decomposition on the given slices provides the density colour map, (c), and the Ca/P ratio colour map, (d). Osteoporotic areas (selected region) are very clearly visible as low density in (c) and low Ca/P ratio in (d).

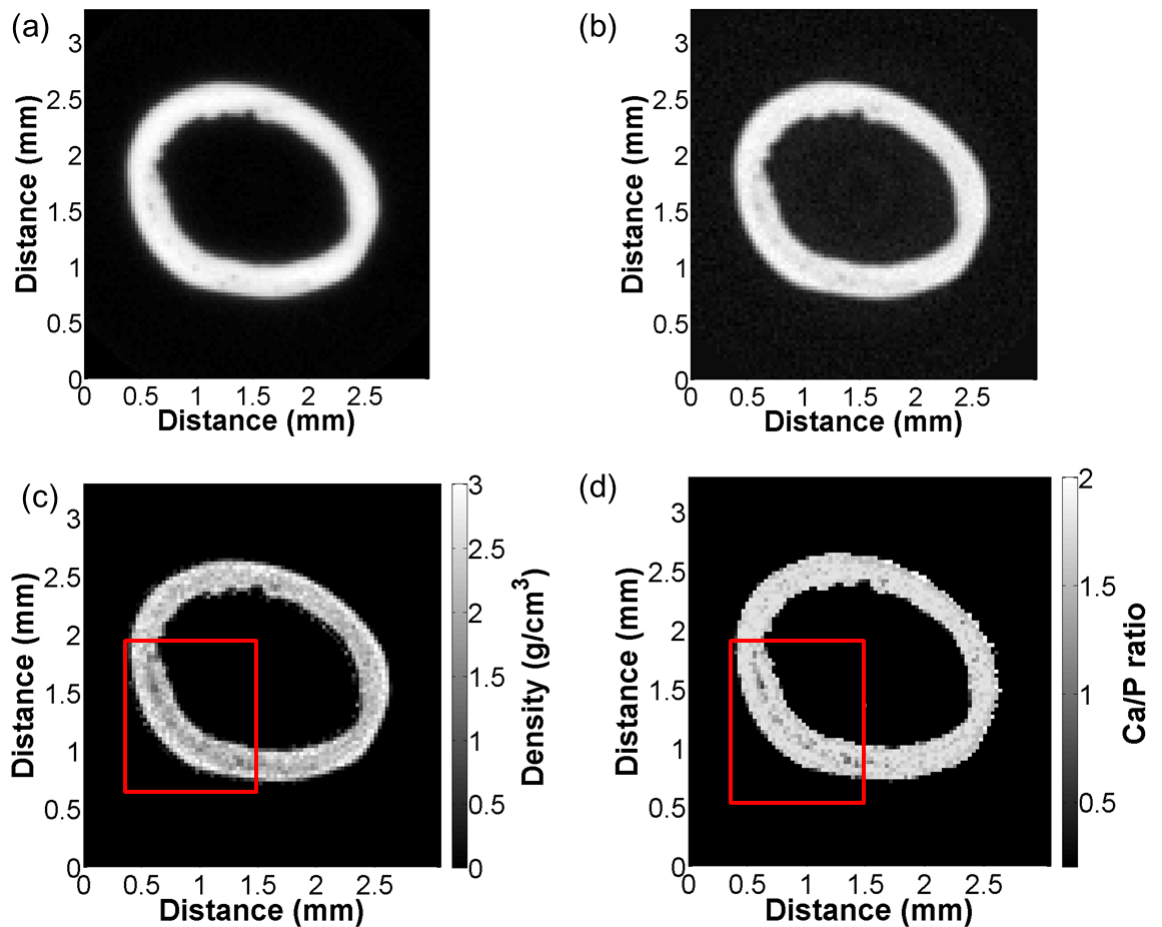


Figure 5.5: One image slice of a front tibia bone sample at (a) low energy and (b) high energy. The corresponding density colour map (c) and Ca/P ratio colour map (d) are products of CT-DEA. Each voxel is $96 \mu\text{m}^3$.

Going through the density and Ca/P ratio colour-maps of healthy samples, it

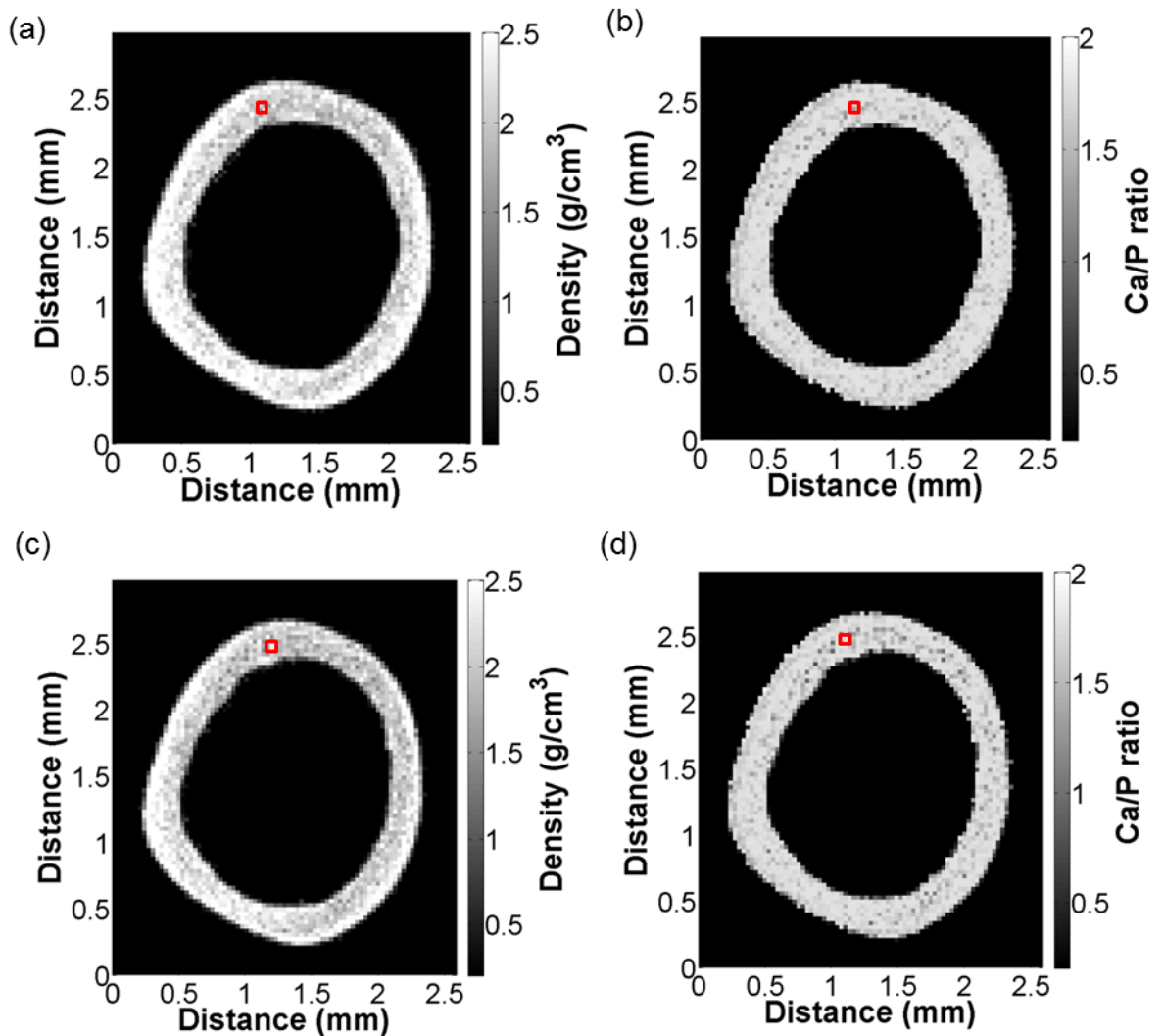


Figure 5.6: Ca/P ratio colour maps ((a) and (c)) and their corresponding density colour maps ((b) and (d)), extracted from two different positions within a healthy rear tibia sample image. The resolution of all colour maps is $96 \mu\text{m}$. The red squares illustrate VOIs, of volume 0.03 mm^3 analysed quantitatively in table 5.3.

is clear that Ca/P ratio is not homogeneous everywhere. A possible reason is the non-perfectly uniform mineralised bone. Bone undergoes dynamic mineralisation to maintain stable plasma electrolyte levels and to allow Calcium to be moved to where it is needed in the body. For example, carbonate groups replace a fraction of Phosphates and/or hydroxyl groups in the mineralised hydroxyapatite ($\text{Ca}_{10}(\text{PO}_4)_6(\text{OH})_2$), thus varying its crystallinity (Wilson et al. [2005], Pasteris et al. [2008], Wopenka and Pasteris [2005]). However, the variable crystallinity depends on the stage in the mineralisation process and age (Rauch and Schoenau [2001]).

Figure 5.6 shows two Ca/P ratio maps ((a) and (c)) and their corresponding density maps ((b) and (d)), extracted from two different positions within a healthy femur sample image. Lower density and Ca/P ratio can be seen in the more inferior slice ((c)-(d)), compared to the more superior slice ((a)-(b)).

Quantitative analysis was performed in VOIs, with a volume of 0.03 mm^3 ($6 \times 6 \times 1$ voxels), as illustrated by the red squares in figures 5.6(a)-(d). Such a small VOI size was selected, since the ideal case would be to identify osteoporosis before a large bone region is affected by it. Specifically, a VOI size of 0.03 mm^3 was selected as it is in the order of the voxel size of a clinical CT scanner (section 1.3.3). Table 5.3 shows the average density (in g/cm^3) and Ca/P ratio of the VOIs. As Ca/P ratio decreases density decreases too. Furthermore, the lower the density and the lower the Ca/P ratio in the VOI, the higher the standard deviation, showing possible increased non-uniformity in its distribution, due to variable crystallinity in the apatite form.

Table 5.3: Average density and Ca/P ratio results of the selected VOIs of a healthy rear tibia, shown in figure 5.6.

Fig 5.6	Density (g/cm^3)		Ca/P ratio	
	Mean	SD	Mean	SD
(a)-(b)	2.12	0.16	1.76	0.03
(c)-(d)	1.96	0.32	1.59	0.27

Going through the density and Ca/P ratio colourmaps of IMO samples, it can be concluded that in IMO samples, osteoporosis does not appear homogeneously in the sample. Figure 5.7 shows three Ca/P ratio maps ((a), (c) and (e)) and their corresponding density maps ((b), (d) and (f)), extracted from three different positions of an IMO femur sample image. As can be visualised there is a strong variability in the density and Ca/P ratio along the bone. Slice 1 (a-b) looks almost completely homogeneous in density and Ca/P ratio. Slice 2 (c-d) shows a decreased density and Ca/P ratio compared, to slice (a-b). In slice 3 (e-f) there is an even more decreased density and Ca/P ratio, as well as decreased cortical thickness. In previous studies it has been shown that decreased cortical thickness could be a sign of osteoporosis (Louis et al. [1995], Cohen et al. [2009]).

Quantitative analysis was performed in VOIs in these slices, all of volume 0.03 mm^3 , illustrated by the red squares in figures 5.7(a)-(f). Table 5.4 shows the results of the average density and Ca/P ratio of the VOIs. As Ca/P ratio decreases density decreases too. The standard deviation increases the lower the density and the Ca/P ratio in the VOI are. This suggests variable crystallinity in the apatite form and increased non-uniformity in the Ca/P ratio and density distribution (Tzaphlidou et al. [2005]).

The analysis of VOIs could be used in CT-DEA to assess the density and Ca/P ratio to understand how they change in the particular region. For example, volumes of interest could be potentially identified using the CT image in a fractured region in a bone, and analysed using CT-DEA, to investigate how density and Ca/P ratio vary in that region. However, VOI density and VOI Ca/P ratio measurements are

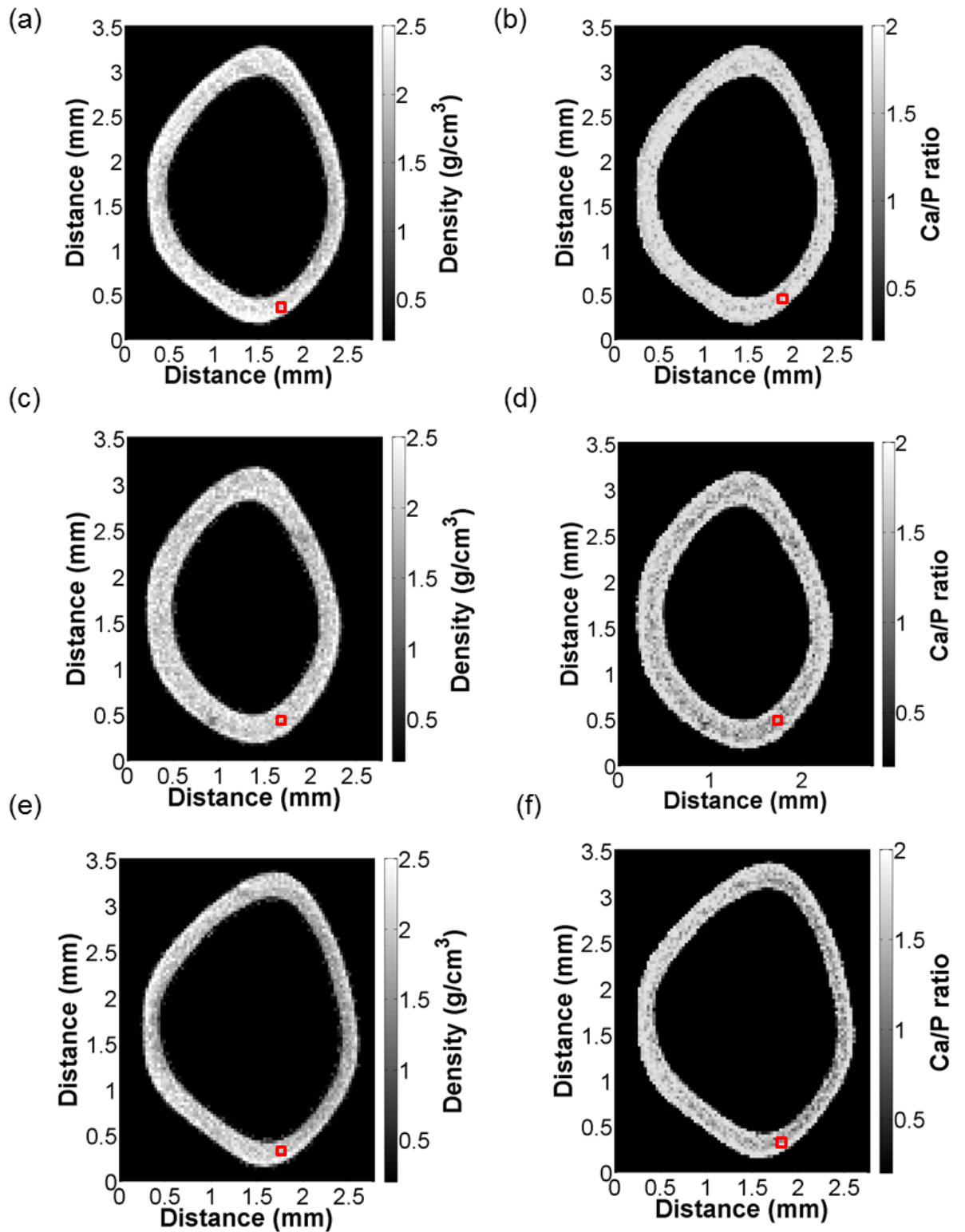


Figure 5.7: Ca/P ratio colour maps ((a), (c) and (e)) and their corresponding density maps ((b), (d) and (f)), extracted from three different positions of an IMO femur sample image. The resolution of the colour maps is $96 \mu\text{m}$. The red squares illustrate VOIs, of volume 0.03 mm^3 , analysed quantitatively in table 5.4.

Table 5.4: Average density and Ca/P ratio results of the selected VOIs, of an IMO femur, shown in figure 5.7.

Fig 5.7	Density (g/cm ³)		Ca/P ratio	
	Mean	SD	Mean	SD
(a)-(b)	2.22	0.12	1.70	0.14
(c)-(d)	1.98	0.13	1.30	0.17
(e)-(f)	1.90	0.18	1.29	0.24

not fully reliable for consistent diagnosis. This is because VOIs might not be representative of the whole bone and the selection of the volume of interest is subjective.

5.3.3 Low Calcium/Phosphorus ratio proportion

The low Ca/P ratio range in bone was defined as 1.00-1.49, in accordance with a study by Fountos et al. [1999]. Utilising such a threshold, the low Ca/P ratio proportion across each bone sample was calculated. Figure 5.8 shows the results of healthy (blue, filled circles) and IMO bone (red, open circles) samples. The results showed a general increase in low Ca/P ratio proportions in IMO samples.

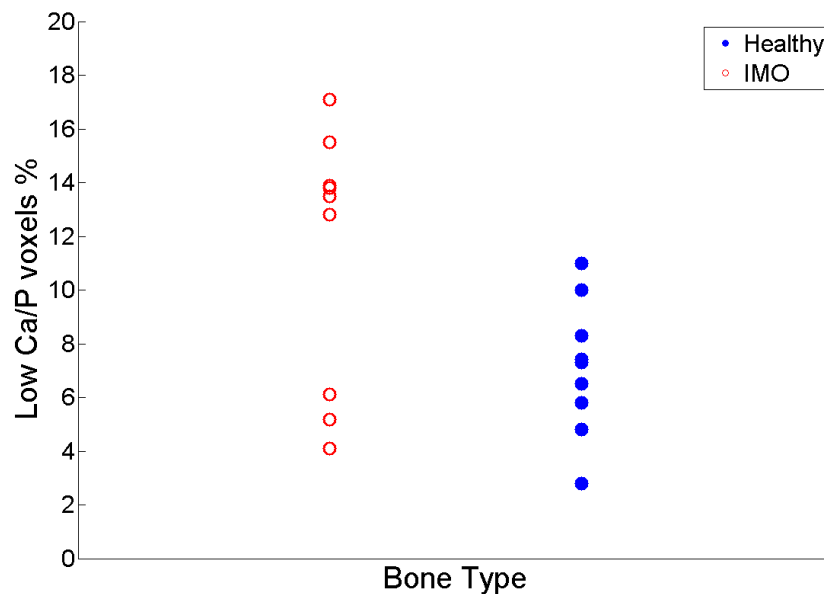


Figure 5.8: The low Ca/P ratio proportion of the 18 collagen-free bone samples. The healthy samples are shown in blue, filled circles and the IMO samples in red, open circles.

Voxels within the low Ca/P ratio limits were present in both healthy (in the range of 2.8-11.0%) and IMO (in the range of 4.1-17.1%) bone samples. As discussed previously, a possible reason for the presence of low Ca/P ratio in healthy samples, is the non-perfectly uniform mineralised bone, due to its variable crystallinity. This is also a contributing factor for the IMO samples, but inflammation-mediated osteoporosis

induces an increased number of low Ca/P ratio regions.

A statistically significant difference was found between the low Ca/P ratio proportion of nine healthy and nine IMO bone samples (table 5.7), with a p-value of 0.0193. It can thus be concluded that low Ca/P ratio proportion could be used as a possible osteoporosis indicator, since its p-value, in the statistical difference of healthy and IMO samples (table 5.7), is lower than 0.05.

Table 5.5: Student's t-test results of the low Ca/P ratio proportion, of the nine healthy and nine IMO bone samples.

Variable	Low Ca/P ratio proportion	
	Healthy	IMO
Mean	7.10	11.33
Observations	9	9
p-value	0.0193	

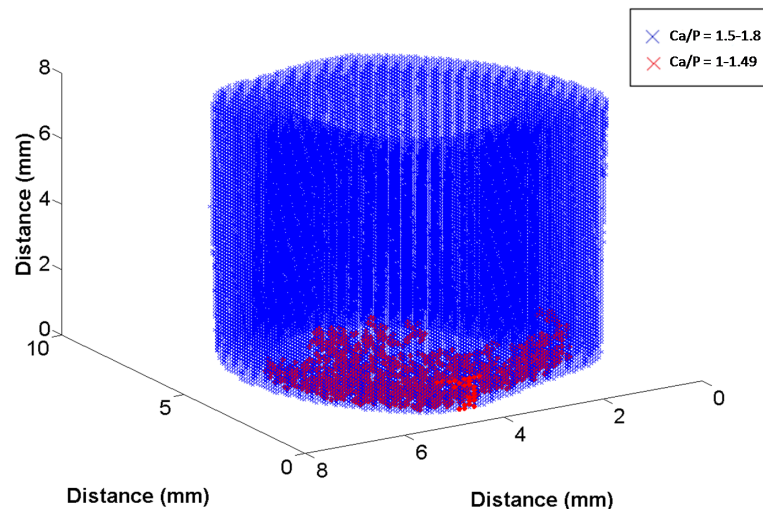
The low Ca/P ratio proportion is an easy parameter to quantify. In addition, it has the advantages of representing the whole bone sample, and at the same time being volume specific.

5.3.4 3D region-grown low Ca/P ratio

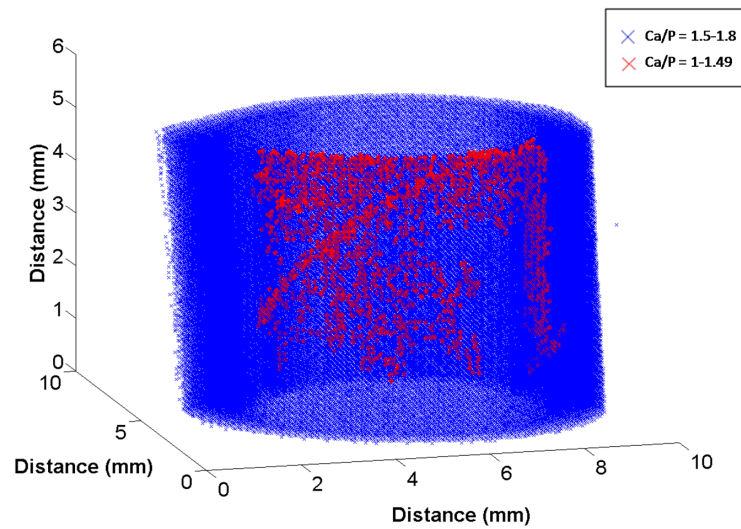
For the identification of possible osteoporotic areas and the assessment of the distribution of the low Ca/P ratio, a 3D region growing technique was applied to all collagen-free bones samples.

The 3D region growing technique provided 3D Ca/P ratio maps in which the interconnected low Ca/P ratio regions can be visualised. Figure 5.9 shows examples of low Ca/P ratio grown regions for healthy rear tibia (a), femur (b) and front tibia (c) bone samples, respectively. Voxels are shown by crosses, with the 'low' (1-1.49) Ca/P ratio range in red and the 'high' (1.5-1.8) Ca/P ratio range in blue. Interconnected-low Ca/P regions are present in all healthy samples, possibly due to the non-perfectly uniform mineralised bone. Similarly, figure 5.10 shows examples of low Ca/P ratio grown regions for IMO rear tibia (a), femur and front tibia (c) bone samples respectively. The larger low Ca/P ratio interconnected regions in IMO (figure 5.10) samples, compared to healthy (figure 5.9) samples, can be clearly seen, especially for rear tibia and femur. Front tibia presents a limited number of low Ca/P ratio interconnected regions.

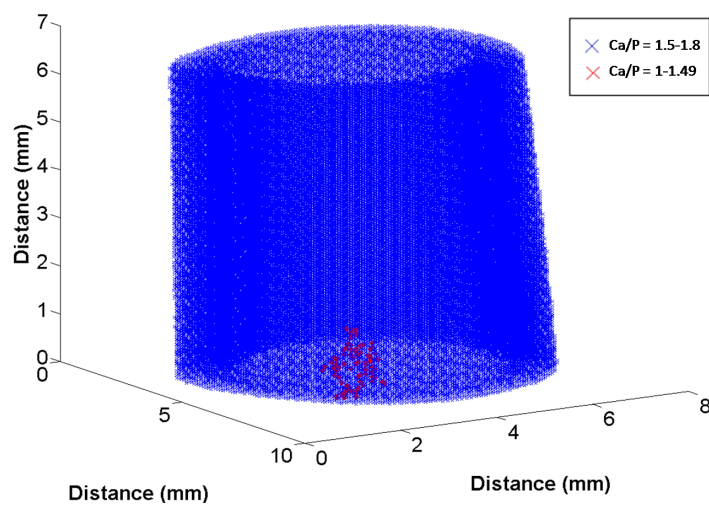
Figure 5.11 shows the region-grown low Ca/P ratio proportion in the collagen-free nine healthy and nine IMO bone samples. There is a trend of increased region-grown low Ca/P ratio proportion in IMO samples (0.7-15%) compared to healthy samples (0-7.6%).



(a)



(b)



(c)

Figure 5.9: Low Ca/P ratio grown regions for healthy rear tibia (a), femur (b) and front tibia (c) bone samples. Voxels are shown by crosses, with the 'low' (1-1.49) Ca/P ratio range in red, and the 'high' (1.5-1.8) Ca/P ratio range in blue.

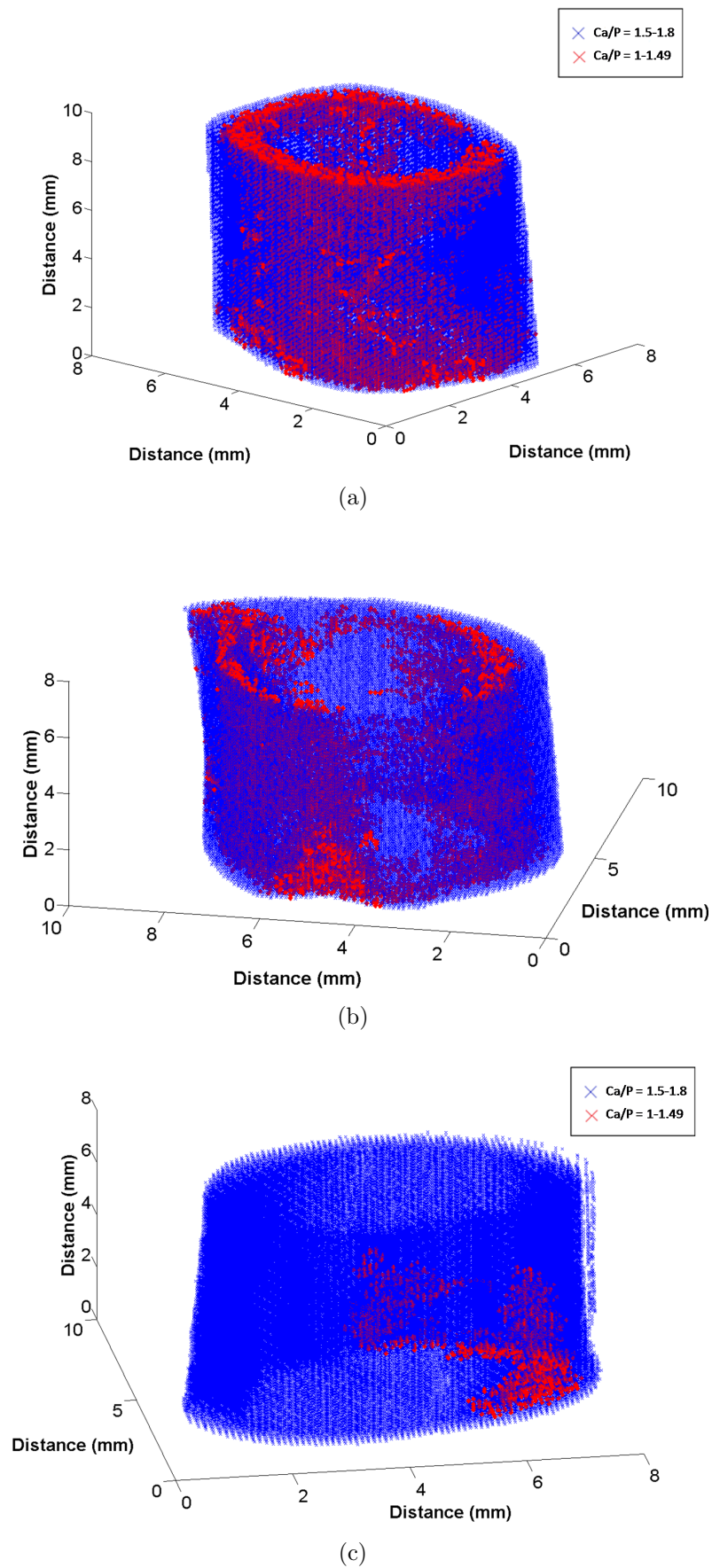


Figure 5.10: Low Ca/P ratio grown regions for IMO rear tibia (a), femur (b) and front tibia (c) bone samples. Voxels are shown by crosses, with the 'low' (1-1.49) Ca/P ratio in red, and the 'high' (1.5-1.8) Ca/P ratio range in blue.

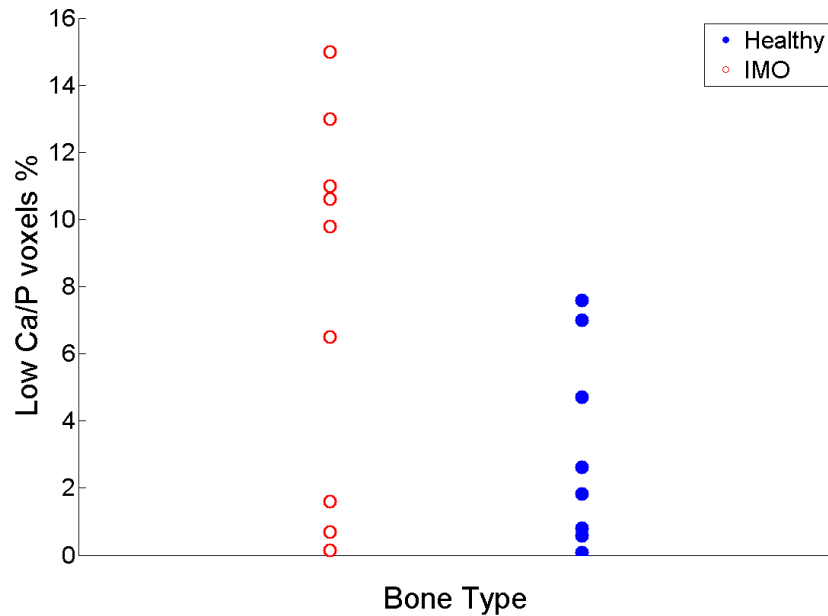


Figure 5.11: The region-grown low Ca/P ratio proportion of the 18 collagen-free bone samples. The healthy samples are shown in blue, filled circles and the IMO samples in red, open circles. Some samples had similar results, overlapping on the plot: for IMO sameples there is one result at 0 and one at 0.07.

Table 5.6: Student's t-test results of the region-grown low Ca/P ratio proportion, of the nine healthy and nine IMO bone samples.

Variable	Low Ca/P ratio proportion	
	Healthy	IMO
Mean	2.80	7.59
Observations	9	9
p-value	0.0209	

A Student's t-test showed a statistically significant difference between the region-grown low Ca/P ratio proportion of nine healthy and nine IMO bone samples (table 5.6), with a p-value of 0.0209. This means that a higher volume of low Ca/P ratio voxels in IMO samples is interconnected, compared with healthy samples. Interconnected-low Ca/P ratio proportion can indicate osteoporosis.

Region-growing technique is a useful tool for the application of CT-DEA on collagen-free samples. Interconnected possible osteoporotic areas can be identified through visualisation as well as quantified analysis. The disadvantage of region growing technique is the long processing time required, because (in theory) each low Ca/P ratio voxel should be tested as a seed voxel. To reduce processing time in this study, only voxels with Ca/P ratio in the middle of the low Ca/P ratio range (1.24-1.25) were tested as possible seed voxels.

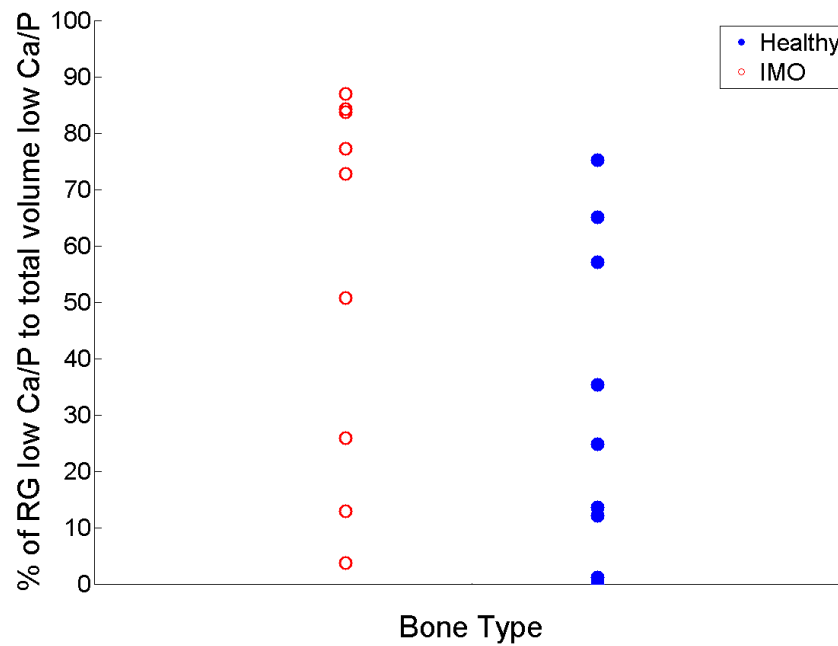


Figure 5.12: The low Ca/P ratio homogeneity (region-grown (RG) low Ca/P ratio volume to low Ca/P ratio total sample volume), of the 18 collagen-free bone samples. The healthy samples are shown in blue, filled circles and the IMO samples in red, open circles.

5.3.5 Low Ca/P ratio homogeneity

For the investigation of the homogeneity of the low Ca/P ratio in bone, the region-grown low Ca/P ratio volume was compared to the total sample low Ca/P ratio volume. The proportion of the region-grown low Ca/P ratio volume to the whole bone low Ca/P ratio volume was found for all bone samples. Figure 5.12 shows the results for all 18 samples separated into healthy (blue, filled circles) and IMO (red, open circles). It is difficult to find any clear difference between healthy and IMO bone samples in this figure, but it is more clear if analysis is made on a site by site basis, with details provided in section 5.5. A slightly decreased proportion of region-grown to total volume low Ca/P ratio was found in healthy (31.6 ± 28.2) samples, compared to IMO (55.3 ± 33.1) samples.

A Student's t-test gave a p-value of 0.0608, suggesting a non-statistically significant difference. However, this p-value still suggests a low probability of the difference in healthy and IMO bone samples being by chance, suggesting it is still worth investigating the difference in the low Ca/P ratio homogeneity in healthy and IMO bone samples further.

5.4 Results: comparing different bone sites

The density and Ca/P ratio parameters were compared between different bone sites to find out if there are any differences between them and conclude on the importance

Table 5.7: Student's t-test results of region grown low Ca/P ratio volume to the whole bone low Ca/P ratio volume, of the nine healthy and nine IMO bone samples.

Variable	Low Ca/P ratio homog.	
	Healthy	IMO
Mean	31.6	55.3
Observations	9	9
p-value	0.0608	

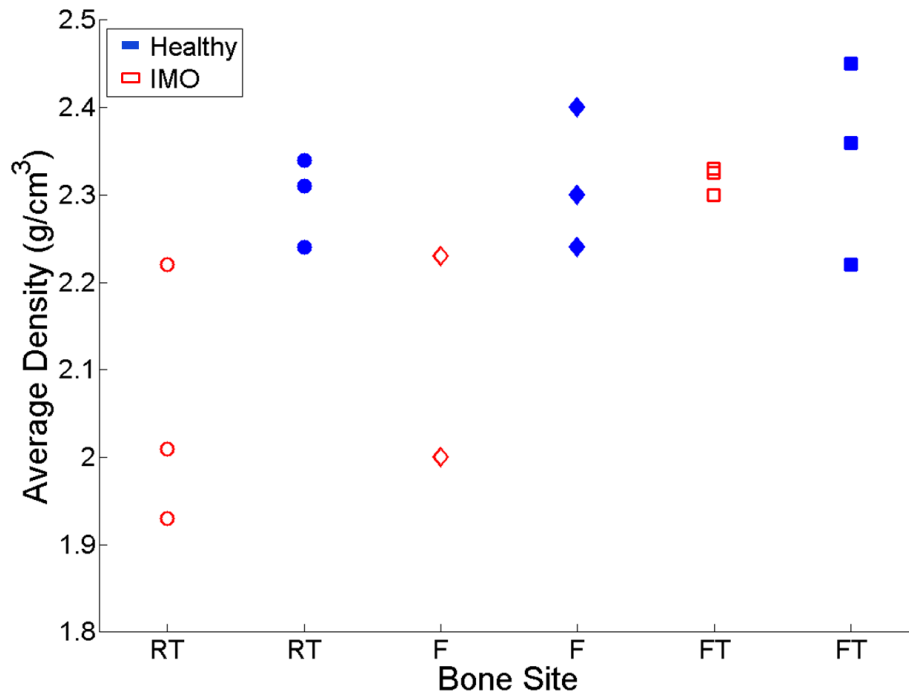


Figure 5.13: The bulk densities of the collagen-free 6 rear tibiae (RT), 6 femurs (F) and 6 front tibiae (FT); healthy (red) and IMO (blue) samples. Error bars have been excluded, for clarity, as the standard error < 0.002 . Some samples had identical results: for IMO samples there are two results at 2.23; for healthy samples there are two results at 2.24.

of the analysis of each bone site separately, when diagnosing osteoporosis in bone apatite (using density and/or Ca/P ratio as indicators). Figure 5.13 shows the bulk densities for six rear tibiae, six femurs and six front tibiae (three healthy and three IMO bone samples for each site). Healthy rear tibiae ($\rho = 2.30 \pm 0.05$), femurs ($\rho = 2.31 \pm 0.08$) and front tibiae ($\rho = 2.34 \pm 0.12$) all have similar densities. In the IMO samples, front tibiae presented increased bulk density results ($\rho = 2.32 \pm 0.02$), compared to rear tibiae ($\rho = 2.05 \pm 0.15$) and femurs ($\rho = 2.15 \pm 0.13$). The average values of each bone site are presented in table 5.9 for a more direct comparison.

The bulk density was compared, between the three different healthy bones sites, individually, using a Student's t-test (table 5.8). For healthy bone, results show that there is not any statistically significant difference in density between the bone sites. However, for IMO bones, there are statistically significant differences between rear

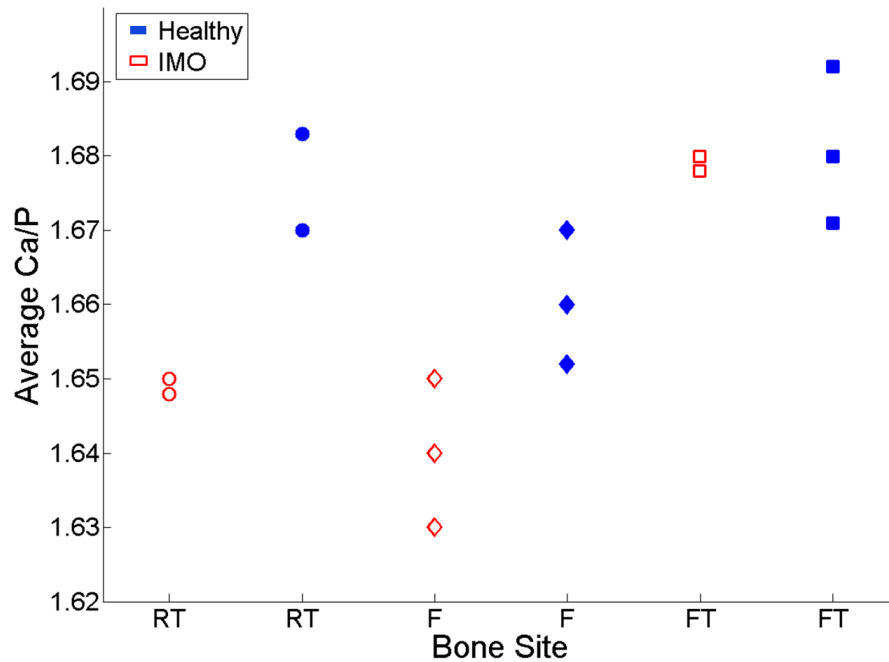


Figure 5.14: The bulk Ca/P ratios of the collagen-free 6 rear tibiae (RT), 6 femurs (F) and 6 front tibiae (FT); healthy (red) and IMO (blue) samples. Error bars have been excluded, for clarity, as the standard error < 0.001 . Some samples had identical results: for IMO samples there are three results at 1.65 and two at 1.68; for healthy samples there are three results at 1.67.

tibia/femur and front tibia.

Similarly, figure 5.14 shows the bulk Ca/P ratio results of all animal bone sites, analysed separately. The healthy front tibiae showed the highest values ($1.68 \pm < 0.001$), then rear tibiae ($1.67 \pm < 0.001$), then femurs ($1.66 \pm < 0.001$). In a study by Speller et al. [2005] rear tibiae also showed increased average Ca/P ratio compared to femurs. Additionally, IMO front tibiae show a higher bulk Ca/P ratio ($1.68 \pm < 0.001$) compared to IMO rear tibiae ($1.65 \pm < 0.001$) and femurs ($1.64 \pm < 0.001$). This is in agreement with Kourkoumelis et al. [2011], who found using EDX that the Ca/P ratio in femurs is affected the least by the inflammation-mediated osteoporosis, compared to the other two bone sites.

For healthy bone, the Student's t-test showed a statistically significant difference between rear femur and front tibia. For IMO bone, a statistically significant difference was found between rear tibia/femur and front tibia.

The average low Ca/P ratio proportion in healthy bone samples was as follows: femurs ($9.4 \pm 1.9\%$), rear tibiae ($7.1 \pm 1.2\%$) and front tibiae ($4.7 \pm 1.8\%$). Similarly, in IMO bone samples: femurs ($15.3 \pm 1.8\%$), rear tibiae ($13.6 \pm 0.3\%$) and front tibiae ($5.1 \pm 1.0\%$). Figure 5.15 demonstrates the results. As in the case of bulk Ca/P ratio, for healthy bone, low Ca/P ratio proportion was only different between front

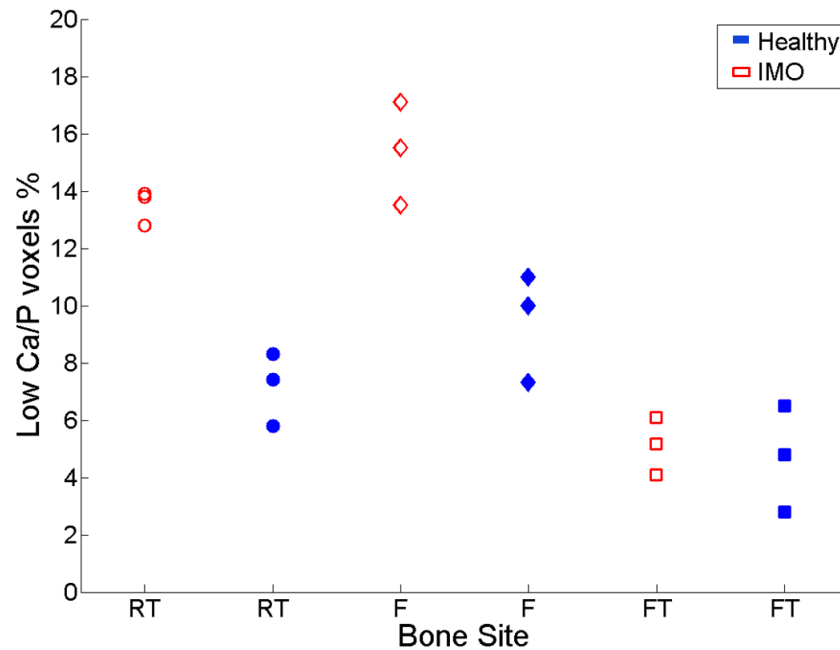


Figure 5.15: The low Ca/P ratio proportion of the collagen-free six RT, six F and six FT; healthy (red) and IMO (blue) samples.

tibia and femur. In the case of IMO bone, the low Ca/P ratio proportion in both rear tibia and femur was different from that in front tibia.

Figure 5.16 presents the results of the region-growing technique. Healthy femurs, rear tibiae and front tibiae showed $5.4 \pm 3.1\%$, $2.7 \pm 1.9\%$ and $0.2 \pm 0.3\%$ region-grown low Ca/P ratio proportion, respectively. IMO femurs, rear tibiae and front tibiae showed $12.6 \pm 2.6\%$, $9.3 \pm 2.4\%$ and $0.8 \pm 0.7\%$, respectively. The statistical analysis of the difference in the region-grown low Ca/P ratio between different bone sites, concludes that it varies significantly between healthy front tibia and femur, and between IMO rear tibia/front tibia and femur.

Statistically significant differences between the same bone sites were found in their low Ca/P ratio homogeneity. The average values of low Ca/P ratio homogeneity in healthy femurs, rear tibiae and front tibiae were $55.1 \pm 26.7\%$, $35.3 \pm 21.7\%$ and $4.4 \pm 7.5\%$, respectively. In IMO healthy femurs, rear tibiae and front tibiae, the low Ca/P ratio homogeneity results were $81.2 \pm 7.5\%$, $70.7 \pm 17.6\%$ and $14.1 \pm 11.0\%$, respectively. IMO bones,

In conclusion, results suggest a statistically significant difference in all the Ca/P parameters between femur and front tibia. This might be due to femur and front tibia located at different areas in the animal body (femur at the back leg, front tibia at the front leg), therefore experiencing different loadings to which there might be adaptations (Cowin [1984], Frost [1990]). Differences in the Ca/P ratios in different rabbit bone sites could be explained by the evolutionary adaptation of each species'

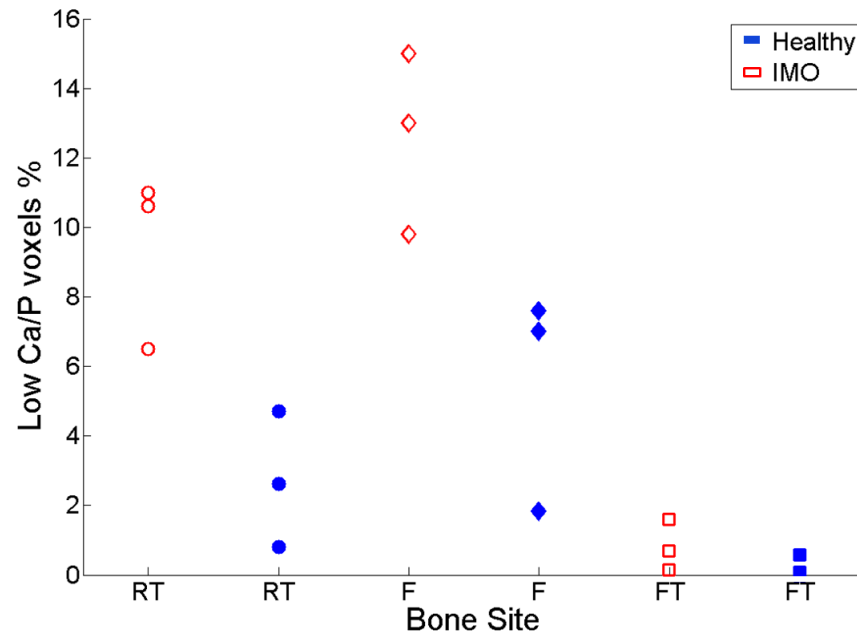


Figure 5.16: The region-grown low Ca/P ratio proportion of the collagen-free six RT, six F and six FT; healthy (red) and IMO (blue) samples. There is an overlap in healthy samples results: one at 0 and one at 0.07.

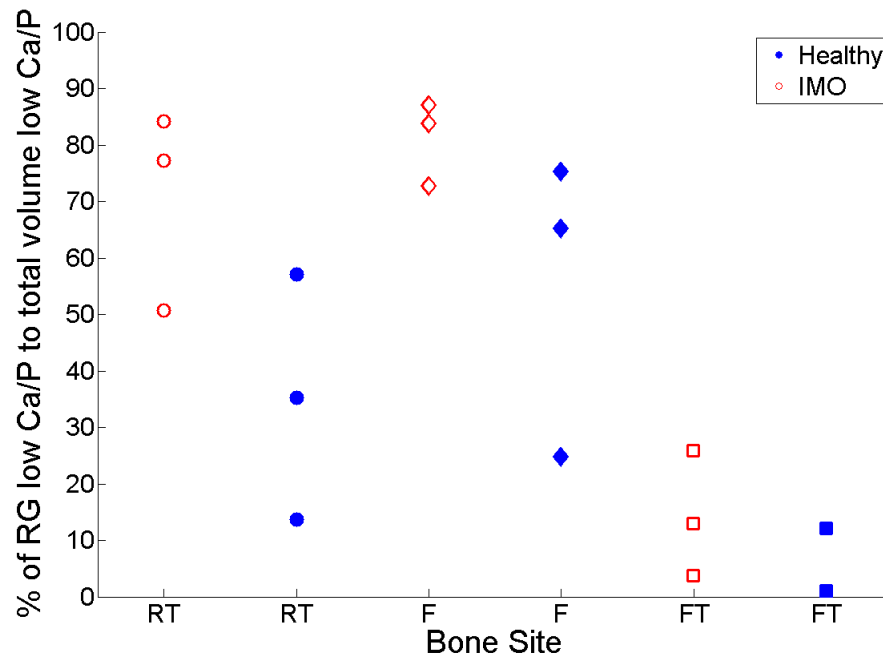


Figure 5.17: The low Ca/P ratio homogeneity (region-grown (RG) low Ca/P ratio volume to low Ca/P ratio total sample volume), of the collagen-free six RT, six F and six FT; healthy (red) and IMO (blue) samples.

Table 5.8: Student's t-test results of the studied parameters, between the 3 healthy and 3 IMO rear tibia, femur and front tibia bone samples. The number of observations in each analysis was 3.

Bone Type	Variables	Density	Ca/P ratio	Low Ca/P prop	RG Low Ca/P prop	Low Ca/P ratio homog.
Healthy	RT and FT	0.2863	0.2135	0.0691	0.0773	0.0612
	RT and F	0.3903	0.0581	0.0871	0.1406	0.1893
	FT and F	0.3669	0.0329	0.0185	0.0509	0.0368
IMO	RT and FT	0.0452	<0.0001	0.0004	0.0101	0.0070
	RT and F	0.2182	0.1232	0.1040	0.0983	0.2107
	FT and F	0.0812	0.0099	0.0014	0.0057	0.0008

bone site to its everyday life activities. For example, the different rabbit bone sites will experience different pressure and load conditions under different moving activities, therefore each bone's quality and strength, reflected in the Ca/P ratio, will be different.

There is a small probability (p-value 0.0581) of any difference in bulk Ca/P ratio between rear tibia and femur being due to chance. Comparing the rear tibia with front tibia, there is no statistical difference, possibly due to being both tibiae, thus experiencing similar loadings.

In the IMO bones, a statistically significant difference was observed between the Ca/P ratio parameters of front tibiae-rear tibiae and front tibiae-femurs. This suggests that front tibiae had a different reaction to osteoporosis to the other two bone sites. Under the assumption that the inflammation affected all bone sites in the same way, there is a different response from different bone sites to osteoporosis. This response could be the result of the different loadings experienced by each bone site, and which also affect the Ca/P ratio even when the bone is healthy.

In the diagnosis of osteoporosis using bone mineral density (BMD), using DEXA, was suggested that a particular osteoporotic bone site is only compared to its corresponding bone site (Kanis and Glu [2000], Grampp et al. [1997]). Similarly, in any potential osteoporosis diagnosis using the Ca/P ratio each bone site should be analysed separately.

5.5 Results: comparing healthy and IMO bones for each bone site

Following the differences of the studied parameters found between different bone sites, the Student's t-test was also used to assess the statistical significance in the difference in the bulk density (in g/cm³), the bulk Ca/P ratio, the low Ca/P ratio proportion, the region-grown low Ca/P ratio proportion and the low Ca/P ratio homogeneity, between the healthy and IMO bone samples, for each bone site separately. Table 5.9 shows the number of observations and p-values for each bone site, together with the average values, which were discussed above.

A statistically significant difference was found for all studied parameters between healthy and IMO rear tibiae (p-values: density 0.0470, Ca/P ratio 0.0132, low Ca/P ratio proportion 0.0026, region-grown low Ca/P ratio proportion 0.0119, low Ca/P ratio homogeneity 0.0481). Similarly, a statistically significant difference was found for all studied parameters between healthy and IMO femurs (p-values: Ca/P ratio 0.0286, low Ca/P ratio proportion 0.0088, region-grown low Ca/P ratio proportion 0.0210), except for the bulk density and low Ca/P ratio homogeneity (p-

Table 5.9: Student's t-test results of the studied parameters, of the 3 healthy and 3 IMO rear tibia, femur and front tibia bone samples.

Bone site	Variable	Density (g/cm ³)		Ca/P ratio		Low Ca/P ratio prop.		RG low Ca/P ratio prop.		Low Ca/P ratio homog.	
		Healthy	IMO	Healthy	IMO	Healthy	IMO	Healthy	IMO	Healthy	IMO
Rear tibia	Mean	2.30	2.05	1.67	1.65	7.2	13.5	2.7	9.4	35.3	70.7
	Observations	3	3	3	3	3	3	3	3	3	3
	p-value	0.0470		0.0132		0.0026		0.0119		0.0481	
Femur	Mean	2.31	2.15	1.66	1.64	9.4	15.4	5.5	12.6	55.1	81.2
	Observations	3	3	3	3	3	3	3	3		
	p-value	0.0821		0.0286		0.0088		0.0210		0.1137	
Front tibia	Mean	2.34	2.32	1.68	1.68	4.7	5.1	0.2	0.8	4.4	14.1
	Observations	3	3	3	3	3	3	3	3		
	p-value	0.3728		0.4038		0.3750		0.1469		0.1378	

values: density 0.0821, low Ca/P ratio homogeneity 0.1137). Front tibiae showed no statistically significant differences, between healthy and IMO, for any of the parameters tested (p-values: density 0.3728, Ca/P ratio 0.4038, low Ca/P ratio proportion 0.3750, region-grown low Ca/P ratio proportion 0.1469, low Ca/P ratio homogeneity 0.1378). In a study by Kourkouvelis et al. [2011] front tibiae also showed the smallest decrease of Ca/P ratio after inflammation-mediated osteoporosis compared to rear tibiae and femurs.

From the above results, it can be concluded that care has to be taken on the selection of the bone site for osteoporosis diagnosis as some bone sites might be more susceptible to osteoporosis and thus might be able to provide more information for the disease than others.

Moreover, it is worth noting that the density p-value in the comparison of healthy and IMO bone samples, for a specific bone site, is always bigger than the p-value of the Ca/P ratio of the same bone site. This is because the standard deviation in density, is bigger than than in Ca/P ratio (section 5.4). This suggests that the individual variation in density is lower than that in Ca/P ratio. The specificity of Ca/P ratio in a particular bone site may be more reliable for diagnosis of osteoporosis in bone apatite. However, no definite conclusions can be made unless a sufficiently high number of bone samples is being tested.

5.6 Summary

CT-DEA provides simultaneous bone (material) density and Ca/P ratio qualitative and quantitative results. One of the aims of this chapter was to investigate different analysis methods of the density and Ca/P ratio results, for a given set of data, using CT-DEA. The different analysis methods applied on a different scale in the sample provided different parameters.

The bulk density and bulk Ca/P ratio across the whole sample is a simple analysis method that provides results representative of the whole bone. The analysis of small ROIs against the bulk density is not representative of the whole sample and the selection is subjective for osteoporosis diagnosis. Low Ca/P ratio proportion is a useful and easy analysis method that quantifies the amount of possible osteoporosis in bone with respect to the whole sample. It is representative of the whole bone sample and it involves the analysis of a volume of interest (possible osteoporotic region), but without the need for the user to select the region to analyse (removing subjectivity). Region-growing technique is a more advanced version of low Ca/P ratio proportion that locates the low Ca/P ratio regions and only selects those that are interconnected. The disadvantage of region-grown low Ca/P ratio parameter is the long processing time required to assess it, but it does decrease the possibility of

noise affecting the results.

In this chapter, the magnitude and distribution of density and Ca/P ratio in healthy and IMO bone samples were investigated using the above parameters. CT-DEA application on collagen-free bone samples and a Student's t-test between all healthy and all IMO bone samples showed a statistically significant difference in the average density and Ca/P ratio across the whole bone sample and in the average density and Ca/P ratio across volumes of sizes 0.03 mm^3 ($6 \times 6 \times 1$ voxels). The low Ca/P ratio proportion, the region-grown low Ca/P ratio proportion and the low Ca/P ratio homogeneity were also significantly different between all healthy and all IMO bone samples.

Different bone sites show different ranges of Ca/P ratio, in agreement with previous studies. A Student's t-test between the different bone sites of samples showed a statistically significant difference between most of the Ca/P ratio parameters of different bone sites, but not the density.

The above results support the further study of bulk density, bulk Ca/P ratio, low Ca/P ratio proportion, region-grown low Ca/P ratio proportion and Ca/P homogeneity, in intact bone, as possible osteoporosis indicators. Furthermore, the analysis of each bone site separately is supported.

The non-invasive measurement of bone (material) density is unique to CT, and to date it has not been measured by DEXA. Ca/P ratio can be measured using planar DEA (Fountos et al. [1999]). However, the advantages of CT-DEA are that soft tissue and bone marrow can be omitted from analysis, using thresholding, and that VOIs can be selected, therefore providing knowledge for the low Ca/P ratio proportion and the distribution of Ca/P ratio in bone.

The technique so far has only been applied to animal healthy and inflammation-mediated osteoporotic bones. Both bone density and Ca/P ratio can be used to provide knowledge for their correlation to bone apatite quality. All the above conclusions support the use of the developed technique for further *in vitro* studies, in order to better understand the behaviour of density and Ca/P ratio in collagen-free healthy and osteoporotic cadaveric human bone apatite.

Chapter 6

Density and Ca/P ratio assessment in healthy and osteoporotic intact cortical bone

6.1 Overview

In this chapter the results of the application of CT-DEA on intact cortical bone samples are presented.

Eighteen healthy (nine) and inflammation-mediated osteoporotic (nine) rabbit intact (collagen present) cortical bone samples were imaged using the microCT system and analysed using CT-DEA. Their density and Ca/P ratio results were analysed and compared, aiming to investigate the magnitude of density and Ca/P ratio in healthy and IMO bones. This chapter presents these results and concludes on the feasibility of distinguishing healthy and IMO intact bone samples using CT-DEA.

In section 6.2, the methods followed are explained. In section 6.3 the results of the three studied parameters are presented and discussed, including the statistical analysis for the comparison of the studied parameters in healthy and IMO bone samples. In section 6.4, statistical analysis on the comparison of different bone sites is presented. The results of the comparison of healthy and IMO bone sites on different bone sites separately are shown in section 6.5. A summary of the chapter is given in section 6.6. Conclusions are made on how the magnitude and distribution of density and Ca/P ratio in intact cortical bone, change in osteoporosis.

6.2 Experimental methods

Bone samples of set 2 (table 2.4), 18 rabbit cortical intact bone samples, were prepared as explained in section 2.5.3. In half of the animals, inflammation-mediated

osteoporosis (IMO) was induced. All 18 bone samples were imaged using the microCT system at the same conditions at which collagen-free bone samples were imaged (table 3.3). Similarly, the same reconstruction, centre of rotation correction and binning processing methods were used (section 5.2.1). Thresholding was also applied to the images to remove any background voxels and any voxels suffering from edge (partial volume) artefacts. The threshold density limits applied were; background: $\rho \leq 0$, sample-edge: $0.01 < \rho \leq 1.25$ and $\rho > 3.60$ and bone sample: $1.25 < \rho \leq 3.60$. Figure 6.1 shows an example of thresholding on a CT slice of a rear tibia bone sample.

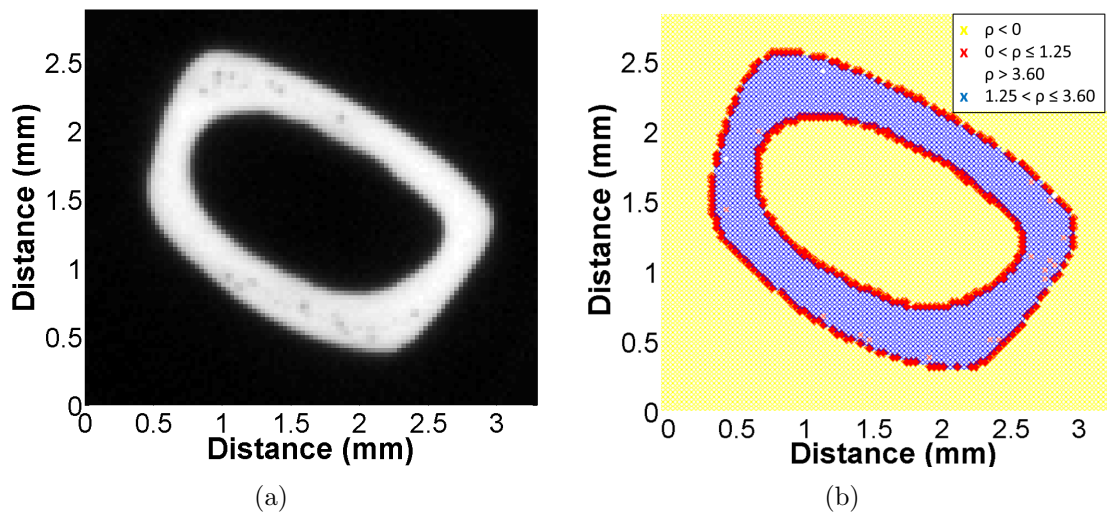


Figure 6.1: (a) Original low energy image of a rear tibia bone sample, and (b) its corresponding density map after thresholding. Yellow ($\rho \leq 0$) and red ($0.01 < \rho \leq 1.25$ and $\rho > 3.60$) areas were rejected, while blue areas ($1.25 < \rho \leq 3.60$) were used for bone analysis.

CT-DEA (section 2.4.5) provided simultaneous quantitative and qualitative results on the density and Ca/P ratio of the samples. The density and Ca/P ratio data was analysed using the methods 1-3, listed in section 5.2.2. The advantages and disadvantages of each of these parameters was discussed in chapter 5. The region-growing technique was not applied in bone samples with collagen, due to the long processing time required (longer time than collagen-free samples analysis, section 6.3.3).

The statistical analyses performed, using the Student's t-test, on the studied parameters), of all bone samples with collagen, was the same as in chapter 5, and is summarised in table 6.1.

Table 6.1: Statistical analyses, using the Student's t-test, performed on the studied parameters of intact bone samples (set 2) and their corresponding sections where the results can be found.

Statistical analysis	Section
Difference in parameters between all healthy and all IMO samples	6.3
Difference in parameters between bone sites	6.5
Difference in parameters between healthy and IMO of different bone sites	6.6

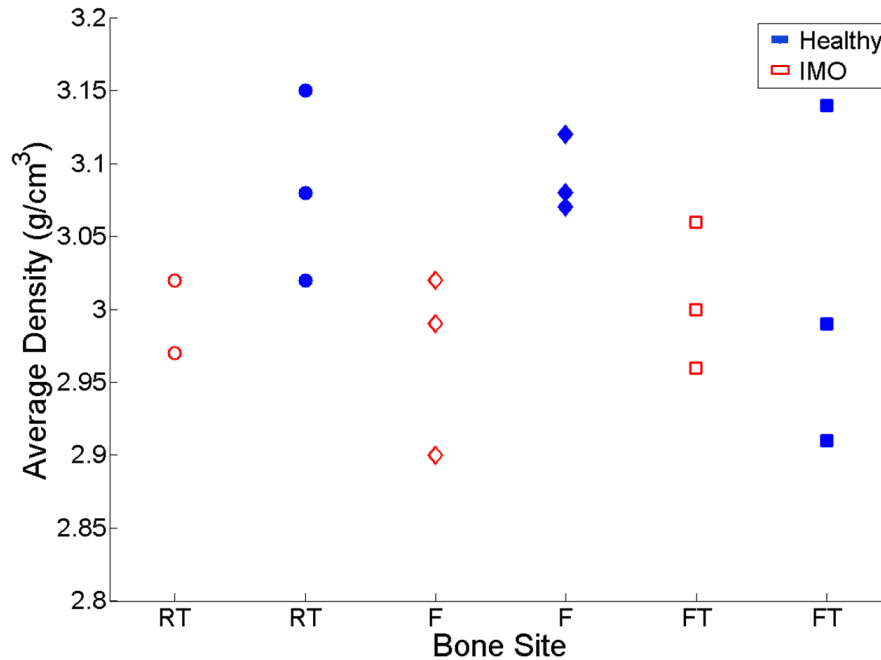


Figure 6.2: The densities (g/cm^3) of the 18 intact bone samples, with healthy samples in red and IMO samples in blue. Error bars have been excluded as the standard error < 0.002 .

6.3 Results: comparing healthy and IMO bones

6.3.1 Density and Ca/P ratio bulk results

The average density and Ca/P ratio were determined across the total volume (varies between 44-136 mm^3 in the 18 intact bone samples) of each of the nine healthy and nine IMO intact bone samples. Figure 6.2 shows the bulk density measurements, in g/cm^3 . The average density, across the whole sample, of the healthy bones (blue) varied within the range 2.91-3.15 g/cm^3 . In the IMO samples the bulk density results (red) varied within the range 2.90-3.06 g/cm^3 .

Figure 6.3 shows the bulk Ca/P ratios of the intact healthy (blue) and IMO (red) bone samples. The average Ca/P ratios, of the healthy bones varied within the range 1.67-2.07. These results are within the Ca/P ratio range (1.46-2.25) in intact bone found in previous studies (Zaichick and Tzaphlidou [2002], Hyvönen-Dabek et al. [1979], Grynopas et al. [1987], Fountos et al. [1999]). In collagen, the

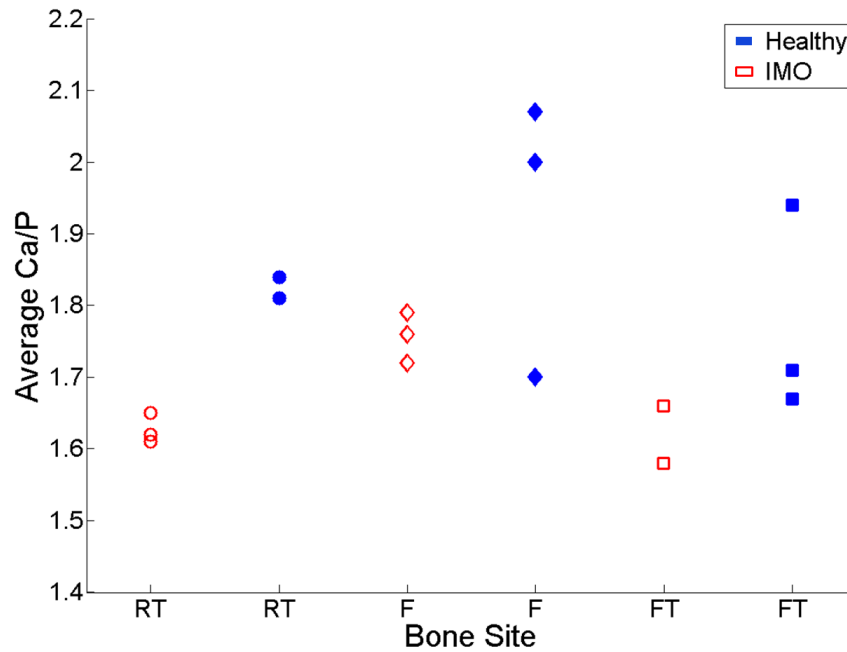


Figure 6.3: The Ca/P ratios of the low-density ($1.25\text{-}3.60\text{ g/cm}^3$) region of 18 intact bone samples, with healthy samples in red and IMO samples in blue. Error bars have been excluded as the standard error < 0.001 .

Table 6.2: Student's t-test results of the bulk density (g/cm^3) and bulk Ca/P ratio, of the 9 healthy and 9 IMO bone samples.

Variable	Density (g/cm^3)		Ca/P ratio	
	Healthy	IMO	Healthy	IMO
Mean	3.06	2.99	1.84	1.66
Observations	9	9	9	9
p-value	0.0137		0.0030	

amounts of Calcium and Phosphorus are lower than in bone apatite, and are also variable (Zaichick and Tzaphlidou [2002], Speller et al. [2005]). This results in a deviation from the stoichiometric Ca/P ratio of bone apatite (1.67) (Tzaphlidou and Zaichick [2003]), and this deviation might vary for different animals and bone sites. In the IMO samples the Ca/P ratio was slightly lower (1.58-1.79), in agreement with previous studies (Tzaphlidou et al. [2005], Speller et al. [2005], Kourkoumelis et al. [2011]).

Table 6.2 shows the significance in the differences between the density and Ca/P ratio of the healthy and IMO samples. P-values of 0.0137 and 0.0030, were found for density and Ca/P ratio respectively, suggesting a statistically significant difference in them between the healthy and the IMO bone samples.

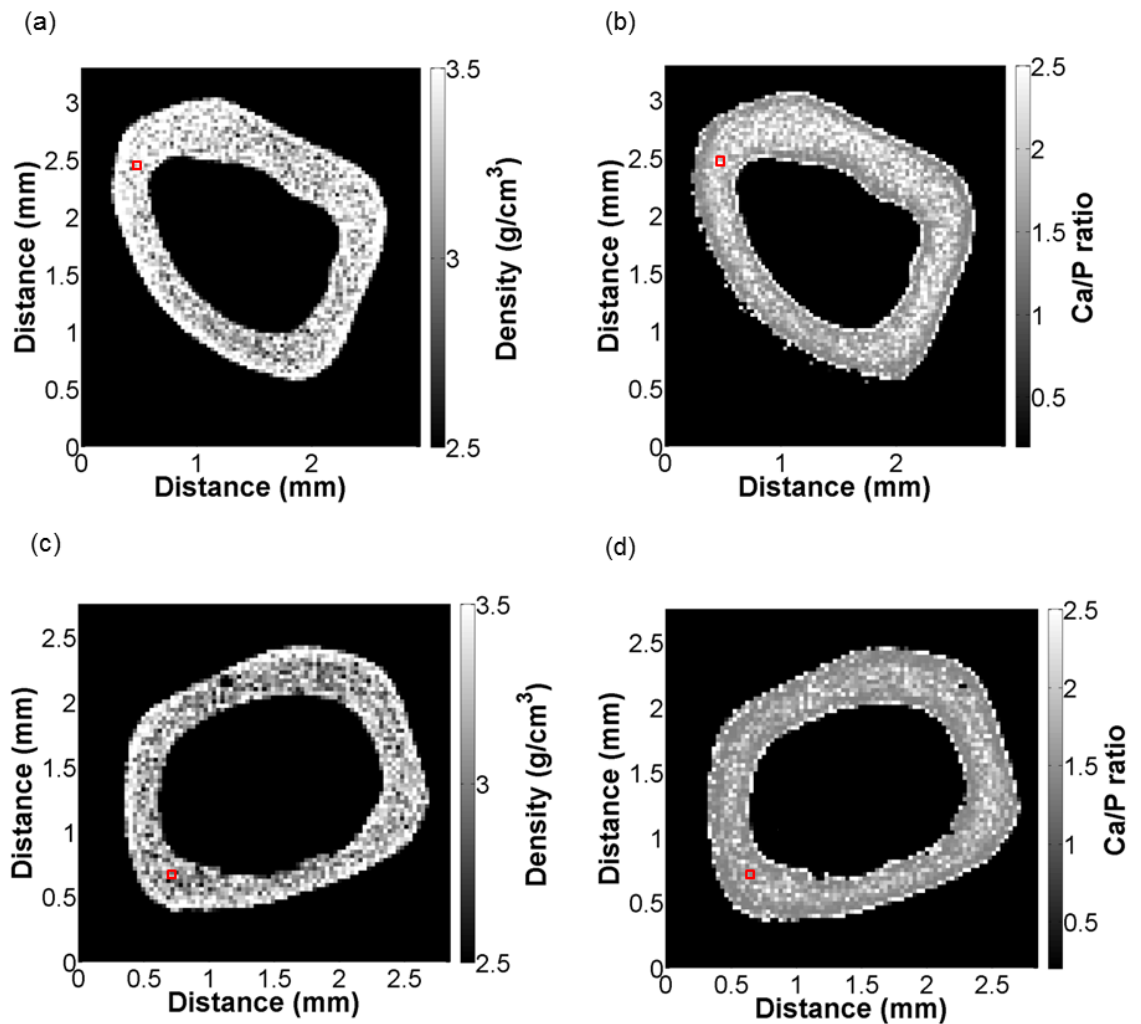


Figure 6.4: Density maps, ((a) and (c)), and their corresponding Ca/P ratio maps, ((b) and (d)), of one healthy (top) and one IMO (bottom) rear tibia intact cortical bone sample. The resolution of all maps is $96 \mu\text{m}$.

6.3.2 Density and Ca/P ratio in volumes of interest

Going through the density and Ca/P ratio maps of healthy samples, it is evident that the Ca/P ratio is not homogeneously distributed, same as in the case of collagen-free samples. Similarly, going through the density and Ca/P ratio maps of IMO samples, it was found that osteoporosis does not appear in the whole of the sample.

An example of a density and a Ca/P ratio map, from one healthy and one IMO bone sample are shown in figure 6.4. A lowered density and Ca/P ratio can be visualised across the IMO bone slice, compared to the healthy bone slice.

Quantitative analysis was performed in ROIs, with a volume of 0.03 mm^3 , as illustrated by the red squares in figure 6.4(a)-(d). Table 6.3 shows the average density (in g/cm^3) and Ca/P ratio of the ROIs. As Ca/P ratio decreases density decreases too.

Table 6.3: Average density and Ca/P ratio results of the selected ROIs of a healthy rear tibia, shown in figure 6.4

Bone type	Fig 6.4	Density (g/cm ³)		Ca/P ratio	
		Mean	SD	Mean	SD
Healthy	(a)-(b)	3.48	0.28	2.18	0.52
IMO	(c)-(d)	3.19	0.21	1.62	0.23

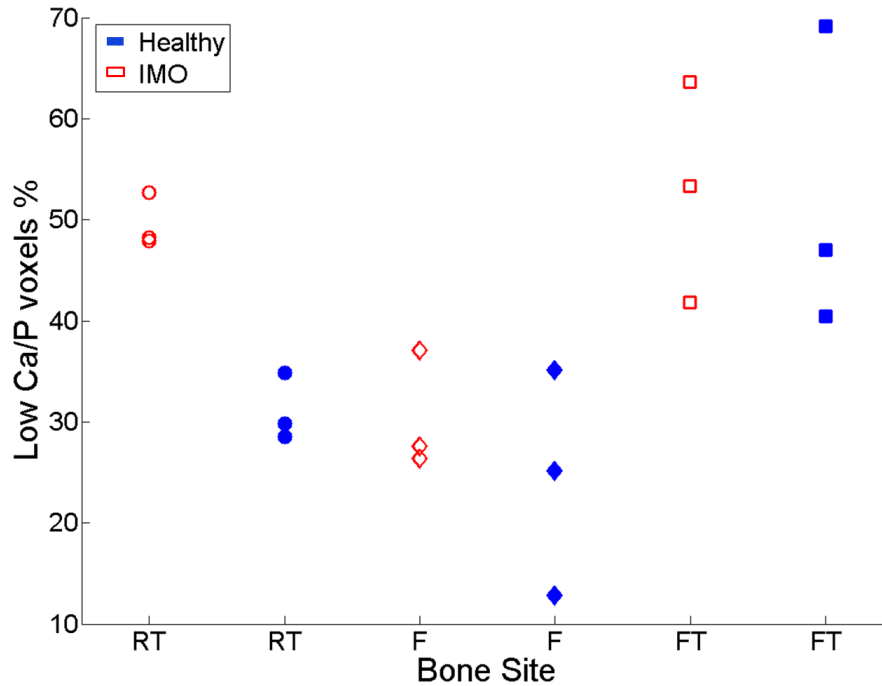


Figure 6.5: The bulk Ca/P ratios of the intact 9 healthy (red) and 9 IMO (blue) samples, after thresholding with density.

6.3.3 Low Ca/P ratio proportion

Figure 6.5 shows the low Ca/P ratio proportion in the intact nine healthy (blue) and nine IMO bone (red) samples. The results show a trend of increased low Ca/P ratio proportion in IMO samples (26.3%-63.6%) compared to healthy bone samples (12.7%-69.1%). A p-value from a Student's t-test of 0.1132 was found (table 6.2), suggesting a probability of 0.1132 of any difference in low Ca/P ratio proportion being due to chance.

Table 6.4: Student's t-test results of the low Ca/P ratio proportion, of the nine healthy and nine IMO bone samples.

Variable	Low Ca/P ratio proportion	
	Healthy	IMO
Mean	35.86	44.28
Observations	9	9
p-value	0.1132	

The low Ca/P ratio proportion of collagen-free bone samples compared to intact bone samples is up to 12 times higher, on a site by site analysis. Due to the large amount of voxels with low Ca/P ratio it would require a long processing time to analyse all the possible seed voxels in the low Ca/P region and perform the region-growing technique. For this reason, the application of region growing technique on intact bone samples was omitted.

6.4 Results: comparing different bone sites

In this section the variability of density and Ca/P ratio between different intact cortical bone sites is discussed. An investigation was made on how the presence of collagen affects the differences between density and Ca/P ratio in different bone sites.

All the average results discussed below are summarised in table 6.6. The average density of healthy and IMO femurs were 3.09 ± 0.02 and 2.97 ± 0.12 respectively. Similarly, for rear tibiae density was, healthy $\rho = 3.08 \pm 0.07$ and IMO $\rho = 2.99 \pm 0.03$, and front tibiae, healthy $\rho = 3.03 \pm 0.05$ and IMO $\rho = 3.00 \pm 0.06$. As in the case of the collagen-free samples, there was not any difference in the densities of bulk different bone sites.

In the analysis of the Ca/P ratio, as detailed in table 6.6, healthy the Ca/P ratio of femurs was $1.92 \pm <0.20$). Healthy rear tibiae had a Ca/P ratio of $1.82 \pm <0.02$, and healthy front tibiae $1.77 \pm <0.15$. Similarly, for the IMO samples: IMO femurs showed the highest Ca/P ratio ($1.76 \pm <0.04$) compared to IMO rear tibiae ($1.63 \pm <0.02$) and IMO front tibiae ($1.69 \pm <0.05$). In the collagen free bone sites, front tibiae presented the highest Ca/P ratio compared to rear tibiae and femurs. A possible reason for femurs showing the highest Ca/P ratio in intact cortical bone, is the different amount of collagen possibly present in each bone site, for example, under the requirement of some bone sites being more flexible than others. A different proportion of collagen in different bone sites would have the following effect. The CT-DEA process was calibrated with the assumption of 15% weight of collagen present in the samples and it was assumed that this is the case for all of the bone sites. A different weight fraction of collagen present in a sample would affect its Ca/P ratio result, forcing it to be calculated lower or higher than it is. This would change the order of the different bone sites with respect to the bulk Ca/P ratio. Another possible explanation for femur showing a higher Ca/P ratio compared to the other bone sites, is the presence of more Calcium and/or less Phosphorus in collagen, compared to the other bone sites.

For the low Ca/P ratio proportion the following results were observed for healthy bone samples; front tibiae ($51.0 \pm 15.0\%$), rear tibiae ($49.6 \pm 3.3\%$) and femurs ($30.3 \pm$

Table 6.5: Student's t-test results of the studied parameters, between the 3 healthy and 3 IMO rear tibia, femur and front tibia intact cortical bone samples. The number of observations in each analysis was three.

Bone Type	Variables	Density p-value	Ca/P ratio p-value	Low Ca/P prop
Healthy	RT and FT	0.2143	0.3179	0.0647
	RT and F	0.4406	0.2294	0.2045
	FT and F	0.1868	0.1764	0.0334
IMO	RT and FT	0.2951	0.2734	0.3285
	RT and F	0.3523	0.0047	0.0084
	FT and F	0.2373	0.0064	0.0246

11.2%). Similarly, for IMO bone samples; front tibiae ($52.2 \pm 10.9\%$), rear tibiae ($31.1 \pm 2.6\%$) and femurs ($24.3 \pm 5.9\%$).

Table 6.5 presents the p-values produced after the Student's t-test analysis, for the comparison of density, Ca/P ratio and low Ca/P ratio proportion in different intact cortical bone sites.

The results suggest no difference in bulk density or bulk Ca/P ratio between any sites, in healthy bone samples, except for the low Ca/P ratio proportion between femurs and front tibiae. In the IMO bone samples however, a difference was found between the bulk Ca/P ratio and low Ca/P ratio proportion between IMO rear tibiae and femurs, and front tibiae and femurs.

These results suggest that even with the presence of collagen differences between different IMO bone sites can be identified. As discussed in section 5.4, there is a different response to osteoporosis between different bone sites. At present, it is unknown if the difference responses found between different bone site are the result of an error introduced in the Ca/P ratio due to a wrong collagen proportion assumption, for a specific bone site, or if it is due to a different amount of Calcium and Phosphorus present in collagen of each bone.

6.5 Results: comparing healthy and IMO bones for each bone site

Table 6.6 shows the mean values, observations number and p-values of the comparison of healthy and IMO bone samples, for each bone site separately.

A statistically significant difference was found for bulk density and Ca/P ratio between healthy and IMO rear tibiae in the analysis of all bone samples sites together (table 6.2). A statistically significant difference was also found in the Ca/P ratio studied parameters between the three healthy and three IMO rear tibias (table 6.5). Femurs and front tibiae showed no statistically significant differences, between healthy and IMO samples, for any of the parameters tested.

Table 6.6: Student's t-test results of the studied parameters, of the three healthy and three IMO rear tibia, femur and front tibia bone samples.

Bone site	Variable	Density (g/cm ³)		Ca/P ratio		Low Ca/P ratio prop.	
		Healthy	IMO	Healthy	IMO	Healthy	IMO
Rear tibia	Mean	3.08	2.99	1.82	1.63	31.1	49.6
	Observations	3	3	3	3	3	3
	p-value	0.1086		0.0439		0.0204	
Femur	Mean	3.09	2.97	1.92	1.76	24.3	30.3
	Observations	3	3	3	3	3	3
	p-value	0.1008		0.1628		0.3893	
Front tibia	Mean	3.01	3.00	1.77	1.69	51.0	52.2
	Observations	3	3	3	3	3	3
	p-value	0.3317		0.1430		0.2615	

Any variable amount of collagen within the bone would affect the accuracy of the results, and thus the statistical significance given by the Student's t-test. A bigger number of samples would help conclude if there are any differences between healthy and IMO bone samples for each bone site separately.

6.6 Summary

The accuracy of planar DEA when applied on intact bone is restricted mainly by the presence of fat, marrow and collagen present in the bone. As shown experimentally, DEA marrow and fat can be a source of considerable error (Fountos [1997], Bolotin and Sievänen [2001]). However, this problem could be easily overcome in CT imaging, by analysing the cortical bone only, after the application of thresholding to the 3D images.

As far as the presence of collagen is concerned, it is still unknown to what degree the variable amount of collagen in bone affects the accuracy of the results. However, it was shown in this chapter that CT-DEA application on intact bone samples can provide qualitative analysis of density and Ca/P ratio on intact bone. Possible osteoporotic areas can be visualised, located and quantified. It is possible to produce realistic results of bone density and Ca/P ratio in intact bone, and provide sufficient accuracy for distinguishing between healthy and IMO bone samples. However, in the case of the analysis of each bone site separately, any error introduced due to the presence and/or variability of collagen in the sample, together with the standard deviation introduced by the small number of samples, superimpose the precision required to distinguish between healthy and IMO bones. A bigger number of samples would help conclude if there are any differences between healthy and IMO bone samples for each bone site separately.

In the analysis of all samples together, statistically significant differences were

found in bulk density and Ca/P ratio, between healthy and IMO bone samples. This conclusion supports the use of the developed technique for further *in vitro* studies, in cadaveric human bone samples, to better understand density and Ca/P ratio magnitude and distribution in healthy and osteoporotic bone. This is further discussed in chapter 7 of this thesis, together with the potential of the technique for *in vivo* applications.

Chapter 7

Concluding remarks and future potential of CT-DEA for density and Ca/P ratio 3D assessment

This thesis presented the development, optimisation and evaluation of a 3D CT-DEA method for density and Ca/P ratio assessment, as well as its application to bone apatite and intact rabbit cortical bone. The qualitative and quantitative data available from the technique could be used to: (i) study the correlation of density and Ca/P ratio to bone mechanical properties (and thus bone quality) *in vitro*, (ii) investigate the use of density and Ca/P ratio as new osteoporosis indicators, first *in vitro*, then *in vivo* (using a conventional CT). In turn, an improvement could be made on understanding and/or diagnosing osteoporosis.

In section 7.1, a summary of the results obtained in this study and the limitations of the developed technique will be discussed. In section 7.2 and 7.3, suggestions are given for how to develop the technique towards its use for the study of the correlation of density and Ca/P ratio to bone mechanical properties and its clinical implementation. Finally, in section 7.4, the final conclusions of this study are made.

7.1 Prospects for CT-DEA system: current limitations and future developments

7.1.1 Progress achieved in present study

Two prototype theoretical frameworks of CT-DEA were developed for the 3D assessment of density and Ca/P ratio using a microCT scanner. The two theoretical frameworks were aimed for their application in: (i) the mineral content of bone, *in vitro* for collagen-free bone samples, (ii) intact (contains collagen) bone, *in vitro*

7. Concluding remarks and future potential of CT-DEA

or *in vivo*. Possible qualitative and quantitative measuring parameters of the technique were identified. Qualitative (for visualisation) parameters include: 2D and 3D density and Ca/P ratio maps. Quantitative parameters include: bulk density, bulk Ca/P ratio, ROI density, ROI Ca/P ratio, low Ca/P ratio proportion, region-grown low Ca/P ratio proportion and low Ca/P ratio homogeneity. In future studies more measuring parameters could be developed.

The developed technique was optimised for its application to an X-tek benchtop microCT system. A framework for the optimisation of the geometry of the system, and thus of the sample position, accounting for the effects of both the focal spot and the detector, determined simultaneously from one set of measurements, was developed. The optimum sample position found fulfilled the resolution requirement of trabecular bone (150 μm). Additionally, all possible sources of error were minimised to ensure that uncertainty on the Ca/P ratio is not greater than the required accuracy in the measured quantity. The optimum low and high average energies for the particular imaging system were identified as 35 keV and 71 keV. These were achieved using a tube voltage pair of 100 kVp and 50 kVp, and respective tube currents of 100 μA and 150 μA , after filtering with 5 mm Al and 0.5 mm Sn, scanning parameters of: magnification = 10, 360 projections and 128 frames.

The evaluation of computed tomography dual energy analysis (CT-DEA) for 3D density and Ca/P ratio assessment in bone apatite was performed. The theoretical precision of the technique in the calculation of density and Ca/P ratio was assessed through simulation. The experimental precision was found by applying the technique in bone phantoms of known density and Ca/P ratio. It was concluded that the technique can assess the Ca/P ratio to a sufficiently high accuracy for identifying some, but not all osteoporotic regions. For the investigation of the feasibility of the technique on the assessment of Ca/P ratio in bone apatite, healthy and inflammation-mediated osteoporotic (IMO) rabbit cortical bone samples were used. The Ca/P ratio results assessed using CT-DEA in 58 different regions in eight bone samples were compared to the Ca/P ratio results of the same regions assessed using electron-dispersive X-ray spectroscopy. The mean difference in the Ca/P ratio between the two techniques was 0.11 ± 0.08 ($8 \pm 6\%$) and the correlation was $R^2 = 0.69$, suggesting sufficient confidence in the experimental capabilities of the CT-DEA technique.

Density and Ca/P ratio were assessed simultaneously in 3D for the first time in this study. The two parameters were firstly assessed in collagen-free bone samples, which represent bone apatite, the part of the bone which is mechanically considered to have the highest Young's modulus. Nine healthy and nine IMO bone samples were assessed. Density and Ca/P ratio changes in bone apatite due to osteoporosis were investigated. It was concluded that bulk density and bulk Ca/P ratio can

be considered as possible osteoporosis indicators. Also, it was found that there is a higher difference in density and Ca/P ratio, between healthy and IMO bone samples, when studied in regions of interest, than when performing bulk measurements of these parameters in bone. Low Ca/P ratio proportion, interconnected low Ca/P ratio proportion and low Ca/P ratio homogeneity were all higher in IMO bone samples. Furthermore, it was shown that there are statistically significant differences between bone sites. It was concluded that Ca/P ratio parameters in different bone sites should be studied separately. All the above results support the use of the developed technique for further *in vitro* studies, in order to better understand the behaviour of density and Ca/P ratio in collagen-free healthy and osteoporotic human cadaveric bone apatite.

Density and Ca/P ratio were also assessed using CT-DEA in intact cortical bone. The technique provided realistic density and Ca/P ratio results. Bulk density and low Ca/P ratio proportion in healthy and IMO bone samples were shown to be statistically significant. Low Ca/P ratio proportion was not statistically significant. In the case of the analysis of each bone site separately statistical significances were found only between a few of the studied parameters. A bigger number of samples would improve the confidence in the results. The conclusions support the use of the developed technique for further *in vitro* studies, in order to better understand density and Ca/P ratio magnitude and distribution in healthy and osteoporotic human bone. Furthermore, they are promising results for future implementations of CT-DEA *in vivo* for osteoporosis diagnosis.

7.1.2 Limitations of the current CT-DEA technique and results

The CT-DEA has promise as a density and Ca/P ratio 3D assessment technique and it is ready to be used for more *in vitro* studies. However, a number of limitations exist in the technique itself and the results that currently prevent clinical transfer of the technique.

Trials: Limitations arose from the lack of testing the technique on human healthy and osteoporotic bone tissues. IMO has so far proved to be a good substitute for osteoporosis. Ca/P ratio results obtained from rabbit healthy and IMO bone samples from this one, and other studies, compare well with results obtained from human healthy and aged or osteoporotic bone samples. However, all previous work on human bone Ca/P ratio was performed in 2D only. The extension to 3D poses many challenges, particularly with reference to how the injection distributes itself throughout the body. Results have shown that osteoporosis does not affect

7. Concluding remarks and future potential of CT-DEA

bone homogeneously, and each bone site at the same degree, but it is not yet known if this is caused by the injection uptake or is a property of the disease itself. This technique allows for 3D assessment, but question marks over the injection lead to the need for real osteoporotic bones to be studied. The technique is currently adequate but the conclusions made in this study do not necessarily apply to human bone.

Furthermore, the technique to date has only been applied to cortical bone and has not been tested on trabecular bone samples. This could be part of future work. The technique has been optimised so that it can provide sufficient resolution for the analysis of trabecular structure.

Instrumentation: One of the main instrumentation limitations of CT-DEA technique is the low power that can be achieved by the microCT system. This limits the accuracy that the technique can provide.

Furthermore, the beam width is small and so there is a limit to the total volume of a sample. At the optimum conditions used, the biggest sample that can be imaged is approximately 1 cm×1 cm×1 cm. This is sufficient when working with animal bone samples. However, one might need to be selective when working with human bone samples or other bigger bone samples. Currently, only a sample of a maximum diameter of <1 cm can be used. Alternative solutions include the cutting of bones to the appropriate size or the use of a different sample magnification/position. The last solution would provide less than 16 μm resolution in the images however. Compromises will need to be made on sample size and resolution, if the current system will be used.

CT-DEA algorithm: In the development of CT-DEA for Ca/P ratio assessment, the assumption was made that the chemical composition of bone varies in the same way that the chemical composition varies between the bone phantoms. This assumption provided realistic results for collagen-free bone samples. However, it is unknown how representative this variation is for human healthy and osteoporotic bone.

Furthermore, the assumption was made that intact bone is made up of 15% collagen. This assumption provided realistic results for intact bone. However, in literature the weight fractions found for bone vary up to 40% (Bauer and Link [2009]).

The above approximations were necessary for the purposes of this study. More accurate relations for the chemical composition variation might be able to be found using electron-dispersive X-ray spectroscopy measurements on bone samples.

7.2 Future system developments towards mechanical testing

Healthy and osteoporotic bone samples non-invasively assessed using CT-DEA can also be used to assess their mechanical properties, using biomechanical tests. Then, the correlation of density and Ca/P ratio to Young's modulus of bone can be investigated. In that case there are some factors which will need to be considered for the sample selection and preparation. There are different kinds of biomechanical tests; tensile, bending and compression. The bone site and bone size that will be chosen determines to a large extent what biomechanical tests can be accomplished. The mechanical properties of bone vary according to variations in the testing conditions. Therefore, important factors of the testing conditions including specimen preservation, hydration, and temperature and strain rate have to be considered. As far as hydration is concerned, it has been suggested that for accurate testing results it is best to test bone in its hydrated condition, by keeping them in physiological saline or wrapping them with saline-soaked gauze during the test. Finally, the rate at which strain is applied during biomechanical testing of bone is important. The resistance of the bone shock absorbed to load varies proportionally to the rate at which the load is applied, so the mechanical properties of wet bone vary slightly with strain rate. If one is trying to simulate physiological conditions, the strain rate should be between 0.01/s and 0.08/s, which is the range of strain rates that occur *in vivo* (Turner and Burr [1993]).

Similarly, Finite Element Analysis (FEA), using a dedicated software, can be applied on the same bone samples to investigate the correlation of density and Ca/P ratio to the mechanical properties of bone non-invasively and in 3D. The general procedure for the production of an FEA model includes the acquisition of a CT image, the production of a mesh (subject to sample geometry and CT value (density/composition)) of the CT image, the application of the mechanical properties (Young's modulus (function of CT number), Poisson's ratio (can be found in literature)), and the loading of the mesh with normal loads on the sample (Wirtz et al. [2000]). The outcome of this will be the mechanical properties of bone. Different degrees of osteoporosis can be assessed by CT-DEA as a function of density and Ca/P ratio as well as by FEA as a function of the mechanical properties of bone. The relation between the two can then be studied.

7.3 Future system developments towards clinical implementation

The CT and CT-DEA have recently received a lot of attention (Wang et al. [2008], Karçaaltıncaba and Akta [2011]). Improvements in CT and CT-DEA would increase the potential for CT-DEA for Ca/P ratio and density assessment in bone. For example, improvements can be made on the image reconstruction method. Due to increased computational power, iterative reconstruction promises significant improvements in image quality (Wang et al. [2008]). In addition, iterative reconstruction can eliminate the requirement of a second image acquisition, in DEA, by incorporating prior information. Furthermore, technological advances in CT make it possible for simultaneous acquisition of volumetric DEA data within seconds.

For the technique to be widely used in a clinical scenario, the factors to be considered include dose, cost and effectiveness compared to other osteoporosis diagnosis techniques.

Dose is an important factor that needs to be taken into account, if the technique is to be applied *in vivo* with a conventional CT system. Compromises will need to be made between dose and the optimum spectra selection, system power and signal to noise ratio.

Furthermore, compromises might need to be made on the body part and imaging system that will be scanned and diagnosed for osteoporosis. For example, the technique could potentially be clinically applied to a small area of the body, away from sensitive tissues, such as the wrist, using pQCT (section 1.4) (dose $< 2 \mu\text{Sv}$), with comparable/lower dose than that of DEXA (around 0.07-5.9 μSv depending on scan mode) (Langton [2010]).

Finally, the usefulness of the technique compared with other available osteoporosis diagnosis techniques will need to be investigated. For example, DEXA gives a dose of 4.6 μSv (Lewis et al. [1994]). Fountos' DEA technique that measures the Ca/P ratio in bone for osteoporosis diagnosis in 2D gives a dose to the skin of between 44-66 μSv (Fountos et al. [1999]). For 3D DEA as in this study, this figure will be higher. Consideration of the enhancement in the diagnosis of osteoporosis using CT-DEA will need to be weighed up against the potentially considerable extra dose.

7.4 Conclusions

In this study the development, optimisation and evaluation of CT-DEA for density and Ca/P ratio in bone 3D assessment, using an X-Tek microCT system were

7. Concluding remarks and future potential of CT-DEA

achieved. The developed technique was applied to healthy and IMO cortical bone samples, both collagen-free and intact. The results showed that the technique can distinguish between some healthy and IMO bone regions/samples. Furthermore, it was shown that there are statistically significant differences in the density and Ca/P ratio between healthy and IMO bone samples. This suggests that the two parameters could be used as osteoporosis indicators.

Possible improvements of the technique include the use of a higher power system and real bone calibration. Even without this, in its current state, the technique is ready to be used for further bone studies *in vitro*, including the application to human bone samples. CT-DEA, in combination with biomechanical tests or FEA, can be used to investigate the correlation of density and Ca/P ratio to bone mechanical properties. Finally, the potential of the technique for osteoporosis diagnosis can be investigated, by taking into consideration patient dose, cost and effectiveness compared to other osteoporosis diagnosis techniques.

References

- Aitken, J. M. (1976). Factors affecting the distribution of zinc in the human skeleton. *Calcified tissue research*, 20(1):23–30.
- Akesson, K., Grynpas, M. D., Hancock, R. G. V., Odselius, R., and Obrant, K. J. (1994). Energy-dispersive X-ray microanalysis of the bone mineral content in human trabecular bone: A comparison with ICPES and neutron activation analysis. *Calcified Tissue International*, 55(3):236–239.
- Alvarez, R. E. and Macovski, A. (1976). Energy-selective reconstructions in X-ray computerized tomography. *Physics in medicine and biology*, 21(5):733–744.
- Armour, K. and Armour, K. (2003). Bone Research Protocols: Inflammation-Induced Osteoporosis, The IMO Model. *Methods in Molecular Medicine*, 80.
- Arvanitis, C. D. and Speller, R. (2009). Quantitative contrast-enhanced mammography for contrast medium kinetics studies. *Physics in medicine and biology*, 54(20):6041–6064.
- Avioli, L. V. and Lindsay, R. C. (1990). *Metabolic bone disease*.
- Bauer, J. S. and Link, T. M. (2009). Advances in osteoporosis imaging. *European journal of radiology*, 71(3):440–449.
- Baum, T., Carballido-Gamio, J., Huber, M. B., Müller, D., Monetti, R., R ath, C., Eckstein, F., Lochm uller, E. M., Majumdar, S., Rummeny, E. J., Link, T. M., and Bauer, J. S. (2010). Automated 3D trabecular bone structure analysis of the proximal femur—prediction of biomechanical strength by CT and DXA. *Osteoporosis international*, 21(9):1553–1564.
- Beutel, J., Kundel, H. L., and Van Metter, R. (2000). *Handbook of medical imaging*.
- Boddy, K. and Glaros, D. (1973). The measurement of Phosphorus in human bone using radioactive neutron sources - a technique for partial body in vivo activation analysis. *International Journal of Applied Radiation and Isotopes*, 24(3):179–182.

- Bolotin, H. H. and Sievänen, H. (2001). Inaccuracies inherent in dual-energy X-ray absorptiometry in vivo bone mineral density can seriously mislead diagnostic/prognostic interpretations of patient-specific bone fragility. *Journal of bone and mineral research*, 16(5):799–805.
- Bonfield, W. (1998). Polyethylene as an Analogous Material for Bone Replacement. *Annals New York Academy of Sciences*, 523:173–177.
- Bonfield, W., Grynblas, M. D., Tully, A. E., Bowman, J., and Abram, J. (1981). Hydroxyapatite reinforced polyethylene—a mechanically compatible implant material for bone replacement. *Biomaterials*, 2(3):185–186.
- Bonfield, W., Wang, M., and Tanner, K. E. (1998). Interfaces in analogue biomaterials. *Acta Materialia*, 46(7):2509–2518.
- Boutroy, S., Rietbergen, B. V., Sornay-rendu, E., Munoz, F., Bouxsein, M. L., Delmas, P. D., and Bmd, A. (2008). Finite Element Analysis Based on In Vivo HR-pQCT Images of the Distal Radius Is Associated With Wrist Fracture in Postmenopausal Women. *Journal of bone and mineral research*, 23(3):392–399.
- Burgess, A. (1987). Vertebral trabecular bone: comparison of single and dual-energy CT measurements with chemical analysis. *Journal of Computer Assisted Tomography*, 11(3):506–515.
- Cameron, J. and Sorenson, J. (1963). Measurement of bone mineral in vivo: an improved method. *Science*, 142(3589):230–232.
- Chaney, E. L. and Hendee, W. R. (1974). Effects of x-ray tube current and voltage on effective focal-spot size. *Medical Physics*, 1(3):141–147.
- Chapman, R. W., Williams, G., Bydder, G., Dick, R., Sherlock, S., and Kreel, L. (1980). Computed tomography for determining liver iron content in primary haemochromatosis. *British medical journal*, 280(6212):440–442.
- Cho, Z. H., Tsai, C. M., and Wilson, G. (1975). Study of contrast and modulation mechanisms in X-ray/photon transverse axial transmission tomography. *Physics in medicine and biology*, 20(6):879–889.
- Ciarelli, M. J., Goldstein, S. A., Kuhn, J. L., Cody, D. D., and Brown, M. B. (1991). Evaluation of orthogonal mechanical properties and density of human trabecular bone from the major metaphyseal regions with materials testing and computed tomography. *Journal of orthopaedic research*, 9(5):674–682.

- Cohen, A., Liu, X. S., Stein, E. M., McMahon, D. J., Rogers, H. F., Lemaster, J., Recker, R. R., Lappe, J. M., Guo, X. E., and Shane, E. (2009). Bone microarchitecture and stiffness in premenopausal women with idiopathic osteoporosis. *The Journal of clinical endocrinology and metabolism*, 94(11):4351–4360.
- Cohn, S. H., Abesamis, C., Zanzi, I., Aloia, J. F., Yasumura, S., and Ellis, K. J. (1977). Body elemental composition: comparison between black and white adults. *American Journal of Physiology*, 232:419–422.
- Cowin, S. C. (1984). The mechanical and stress adaptive properties of bone. *Annals of biomedical engineering*, 111:263–295.
- Cunningham, I. and Reid, B. (1992). Signal and noise in modulation transfer function determinations using the slit, wire, and edge techniques. *Medical physics*, 19(4):1037–1044.
- Day, M. J. (1976). Specification and additivity of unsharpness in diagnostic radiology. *Physics in medicine and biology*, 21(3):399–405.
- Deodhar, A. A. and Woolf, A. D. (1996). Bone mass measurement and bone metabolism in rheumatoid arthritis: a review. *British journal of rheumatology*, 35(4):309–322.
- Dickerson, J. W. (1962). Changes in the composition of the human femur during growth. *The Biochemical journal*, 82:56–61.
- Dinten, J. (2001). Dual-energy x-ray absorptiometry using 2D digital radiography detector: application to bone densitometry. *Proceedings of SPIE*, 4320:459–468.
- Dorozhkin, S. V. (2009). Calcium orthophosphate-based biocomposites and hybrid biomaterials. *Journal of Materials Science*, 44(9):2343–2387.
- Endo, M., Tsunoo, T., Nakamori, N., and Yoshida, K. (2001). Effect of scattered radiation on image noise in cone beam CT. *Medical Physics*, 28(4):469.
- Fabbri, S., Taibi, A., Longo, R., Marziani, M., Olivo, A., Pani, S., Tuffanelli, A., and Gambaccini, M. (2002). Signal-to-noise ratio evaluation in dual-energy radiography with synchrotron radiation. *Physics in medicine and biology*, 47(22):4093–4105.
- Ferguson, N. (2004). *Osteoporosis in focus*.
- Fountos, G. (1997). The skeletal calcium/phosphorus ratio: A new in vivo method of determination. *Medical Physics*, 24(8):1303–1310.

- Fountos, G., Tzaphlidou, M., Kounadi, E., and Glaros, D. (1999). In vivo measurement of radius calcium/phosphorus ratio by X-ray absorptiometry. *Applied radiation and isotopes*, 51(3):273–278.
- Frost, H. M. (1990). Skeletal Structural Adaptations to Mechanical Usage (SATMU):1. Redefining Wolff’s Law : The Bone Modeling Problem. *The anatomical record*, 413:403–413.
- Fujita, H., Tsai, D. Y., Itoh, T., Doi, K., Morishita, J., Ueda, K., and Ohtsuka, A. (1992). A simple method for determining the modulation transfer function in digital radiography. *IEEE transactions on medical imaging*, 11(1):34–39.
- Gayer, A., Saya, A., and Shiloh, A. (1990). Automatic recognition of welding defects in real-time radiography. *NDT International*, 23(3):131–136.
- Genant, H. and Boyd, D. (1977). Quantitative bone mineral analysis using dual energy computed tomography. *Investigative radiology*, 12(1):545–551.
- Goldberg, H. and Cann, C. (1982). Noninvasive quantitation of liver iron in dogs with hemochromatosis using dual-energy CT scanning. *Investigative Radiology*, 17(1):375–380.
- Gong, J. K., Arnold, J. S., and Cohn, S. H. (1964). Composition of trabecular and cortical bone. *Anat. Rec.*, 149(3):325–331.
- Goodhew, P. J., Humphreys, J., and Beanland, R. (2001). *Electron microscopy and analysis*.
- Grampp, S., Genant, H. K., Mathur, A., Lang, P., Jergas, M., Takada, M., Glüer, C. C., Lu, Y., and Chavez, M. (1997). Comparisons of noninvasive bone mineral measurements in assessing age-related loss, fracture discrimination, and diagnostic classification. *Journal of bone and mineral research*, 12(5):697–711.
- Grynpas, M. (1993). Age and Disease-Related Changes in the Mineral of Bone. *Calcified Tissue International*, 53:57–64.
- Grynpas, M. D., Pritzker, K. P. H., and Hancock, R. G. V. (1987). Neutron activation analysis of bulk and selected trace elements in bones using a low flux SLOWPOKE reactor. *Biological Trace Element Research*, 13(1):333–344.
- Hall, S. (2006). *Basic Biomechanics*. McGraw-Hill Humanities.
- Hartman, R., Kawashima, A., Takahashi, N., Silva, A., Vrtiska, T., Leng, S., Fletcher, J., and McCollough, C. (2012). Applications of dual-energy CT in urologic imaging: an update. *Radiologic clinics of North America*, 50(2):191–205.

- Heaney, R. P., Recker, R. R., and Saville, P. D. (1978). Menopausal changes in bone remodeling. *The Journal of Laboratory and Clinical Medicine*, 92(6):964–970.
- Heismann, B. J., Leppert, J., and Stierstorfer, K. (2003). Density and atomic number measurements with spectral x-ray attenuation method. *Journal of Applied Physics*, 94(3):2073–2079.
- Hyvönen-Dabek, M., Riihonen, M., and Dabek, J. T. (1979). Elemental analysis of bone mineral by backscattering of alpha particles. *Physics in medicine and biology*, 24(5):988–998.
- Johnell, O. and Kanis, J. A. (2006). An estimate of the worldwide prevalence and disability associated with osteoporotic fractures. *Osteoporosis international*, 17(12):1726–1733.
- Johnson, T. R. C., Krauss, B., Sedlmair, M., Grasmuck, M., Bruder, H., Morhard, D., Fink, C., Weckbach, S., Lenhard, M., Schmidt, B., Flohr, T., Reiser, M. F., and Becker, C. R. (2007). Material differentiation by dual energy CT: initial experience. *European radiology*, 17(6):1510–1517.
- Judex, S., Boyd, S., Qin, Y.-X., Miller, L., Müller, R., and Rubin, C. (2003). Combining high-resolution micro-computed tomography with material composition to define the quality of bone tissue. *Current osteoporosis reports*, 1(1):11–19.
- Kalender, W., Perman, W., Vetter, J., and Klotz, E. (1986). Evaluation of a prototype dual-energy computed tomographic apparatus. I. Phantom studies. *Medical physics*, 13(3):334–339.
- Kandarakis, I. (2001). *Physical and technological principles of diagnostic imaging*.
- Kanis, J. A., Borgstrom, F., De Laet, C., Johansson, H., Johnell, O., Jonsson, B., Oden, A., Zethraeus, N., Pflieger, B., and Khaltsev, N. (2005). Assessment of fracture risk. *Osteoporosis international*, 16(6):581–9.
- Kanis, J. A. and Glu, C. (2000). An Update on the Diagnosis and Assessment of Osteoporosis with Densitometry. *Osteoporosis international*, 11:192–202.
- Kanis, J. A., Melton, L. J., Christiansen, C., Johnston, C. C., and Khaltsev, N. (1994). The diagnosis of osteoporosis. *Journal of bone and mineral research*, 9(8):1137–1141.
- Karçaaltıncaba, M. and Akta, A. (2011). Dual-energy CT revisited with multidetector CT: review of principles and clinical applications. *Diagnostic and interventional radiology (Ankara, Turkey)*, 17(3):181–194.

- Kazakia, G. J. and Majumdar, S. (2006). New imaging technologies in the diagnosis of osteoporosis. *Reviews in endocrine & metabolic disorders*, 7(1-2):67–74.
- Kelcz, F., Joseph, P., and Hilal, S. (1979). Noise considerations in dual energy CT scanning. *Medical physics*, 6(5):418–425.
- Kounadi, E., Fountos, G., and Tzaphlidou, M. (1998). The influence of inflammation-mediated osteopenia (IMO) on the structure of rabbit bone and skin collagen fibrils. *Connective tissue research*, 37(1-2):69–76.
- Kourkoumelis, N., Balatsoukas, I., and Tzaphlidou, M. (2011). Ca/P concentration ratio at different sites of normal and osteoporotic rabbit bones evaluated by Auger and energy dispersive X-ray spectroscopy. *Journal of Biological Physics*, 38(2):279–291.
- Koutalonis, M., Delis, H., Spyrou, G., Costaridou, L., Tzanakos, G., and Panayiotakis, G. (2008). Monte Carlo studies on the influence of focal spot size and intensity distribution on spatial resolution in magnification mammography. *Physics in medicine and biology*, 53(5):1369–1384.
- Krempien, B., Vukicević, S., Vogel, M., Stavljenić, A., and Büchele, R. (1988). Cellular basis of inflammation-induced osteopenia in growing rats. *Journal of bone and mineral research*, 3(5):573–582.
- Laib, A., Barou, O., Vico, L., Lafage-Proust, M. H., Alexandre, C., and Rügsegger, P. (2000). 3D micro-computed tomography of trabecular and cortical bone architecture with application with application to a rat model of immobilisation osteoporosis. *Medical & Biological Engineering & Computing*, 38:326–332.
- Laib, A., Hildebrand, T., Häuselmann, H. J., and Rügsegger, P. (1997). Ridge number density: a new parameter for in vivo bone structure analysis. *Bone*, 21(6):541–546.
- Langton, C. (2010). Bone densitometry for the assessment of osteoporosis. *RAD Magazine*, 36(416):15–16.
- Lehmann, L., Alvarez, R., and Macovski, A. (1981). Generalized image combinations in dual KVP digital radiography. *Medical physics*, 8(5):659–667.
- Lewis, M. K., Blake, G. M., and Fogelman, I. (1994). Original Article Patient Dose in Dual X-ray Absorptiometry. *Osteoporosis international*, 4:11–15.
- Liu, X., Yu, L., Primak, A. N., and McCollough, C. H. (2009). Quantitative imaging of element composition and mass fraction using dual-energy CT: Three-material decomposition. *Medical Physics*, 36(5):1602–1609.

- Louis, O., Boulpaep, F., Willnecker, J., Van den Winkel, P., and Osteaux, M. (1995). Cortical mineral content of the radius assessed by peripheral QCT predicts compressive strength on biomechanical testing. *Bone*, 16(3):375–379.
- Lu, Y., Genant, H. K., Shepherd, J., Zhao, S., Mathur, A., Fuerst, T. P., and Cummings, S. R. (2001). Classification of osteoporosis based on bone mineral densities. *Journal of bone and mineral research*, 16(5):901–910.
- Lubberts, G. and Rossmann, K. (1967). Modulation transfer function associated with geometrical unsharpness in medical radiography. *Physics in medicine and biology*, 12(1):65–77.
- Majumdar, S. (2008). Magnetic resonance imaging for osteoporosis. *Skeletal radiology*, 37(2):95–97.
- Majumdar, S., Genant, H. K., Grampp, S., Newitt, D. C., Truong, V. H., Lin, J. C., and Mathur, A. (1997). Correlation of trabecular bone structure with age, bone mineral density, and osteoporotic status: in vivo studies in the distal radius using high resolution magnetic resonance imaging. *Journal of bone and mineral research*, 12(1):111–118.
- Martn-Badosa, E., Elmoutaouakkil, A., Nuzzo, S., Amblard, D., Vico, L., and Peyrin, F. (2003). A method for the automatic characterization of bone architecture in 3D mice microtomographic images. *Computerized Medical Imaging and Graphics*, 27(6):447–458.
- McCreadie, B. R., Morris, M. D., Chen, T.-C., Sudhaker Rao, D., Finney, W. F., Widjaja, E., and Goldstein, S. A. (2006). Bone tissue compositional differences in women with and without osteoporotic fracture. *Bone*, 39(6):1190–1195.
- Miculescu, F. and Ciocan, L. (2011). Effect of heating process on micro structure level of cortical bone prepared for compositional analysis. *Digest Journal of Nanomaterials and Biostructures*, 6(1):225–233.
- Miller, E. J. and Martin, G. R. (1968). The collagen of bone. *Clinical Orthopaedics and related research*, 59:195–231.
- Minne, H. W., Pfeilschifter, J., Scharla, S., Mutschelknauss, S., Schwarz, A., Krempien, B., and Ziegler, R. (1984). (1984) Inflammation-mediated osteopenia in the rat: a new animal model for pathological loss of bone mass, *Endocrinology*, 115, 50-54. *Endocrinology*, 115:50–54.
- Moy, J. P., Bosset, B., and Moirans, F. (1999). How does real offset and gain correction affect the OQE in images from X-ray Flat detectors? *SPIE Conference on Physics of Medical Imaging*, 3659(February):90–97.

- Newitt, D., Majumdar, S., van Rietbergen, B., von Ingersleben, G., Harris, S. T., Genant, H. K., Chesnut, C., Garnero, P., and MacDonald, B. (2002). In vivo assessment of architecture and micro-finite element analysis derived indices of mechanical properties of trabecular bone in the radius. *Osteoporosis International*, 13:6–17.
- Nieves, J. W., Golden, A. L., Siris, E., Kelsey, J. L., and Lindsay, R. (1995). Teenage and current calcium intake are related to bone mineral density of the hip and forearm in women aged 30-39 years. *American journal of epidemiology*, 141(4):342–351.
- Ning, R., Tang, X., and Conover, D. (2004). X-ray scatter correction algorithm for cone beam CT imaging. *Medical Physics*, 31(5):1195–1202.
- Nowotny, R. (1998). XMuDat: Photon attenuation data on PC. In *IAEA-NDS-195 Vienna, Austria Available on diskette or at <http://www-mds.iaea>*.
- Nuzzo, S., Meneghini, C., Braillon, P., Bouvier, R., Mobilio, S., and Peyrin, F. (2003). Microarchitectural and physical changes during fetal growth in human vertebral bone. *Journal of bone and mineral research*, 18(4):760–768.
- Osnes, E. K., Lofthus, C. M., Meyer, H. E., Falch, J. A., Nordsletten, L., Cappelen, I., and Kristiansen, I. S. (2004). Consequences of hip fracture on activities of daily life and residential needs. *Osteoporosis international*, 15(7):567–574.
- Pasteris, J. D., Wopenka, B., and Valsami-Jones, E. (2008). Bone and Tooth Mineralization: Why Apatite? *Elements*, 4(2):97–104.
- Pfeilschifter, J., Wüster, C., Vogel, M., Enderes, B., Ziegler, R., and Minne, H. W. (1987). Inflammation-mediated osteopenia (IMO) during acute inflammation in rats is due to a transient inhibition of bone formation. *Calcified tissue international*, 41(6):321–325.
- Pistoia, W., van Rietbergen, B., Lochmüller, E.-M., Lill, C. A., Eckstein, F., and Rüegesegger, P. (2002). Estimation of distal radius failure load with micro-finite element analysis models based on three-dimensional peripheral quantitative computed tomography images. *Bone*, 30(6):842–848.
- Poludniowski, G., Landry, G., DeBlois, F., Evans, P. M., and Verhaegen, F. (2009). SpekCalc: a program to calculate photon spectra from tungsten anode x-ray tubes. *Physics in medicine and biology*, 54(19):433–438.
- Postnov, A. A., Vinogradov, A. V., Van Dyck, D., Saveliev, S. V., and De Clerck, N. M. (2003). Quantitative analysis of bone mineral content by x-ray microtomography. *Physiological measurement*, 24(1):165–178.

- Price, B. D., Esbrand, C. J., Olivo, A., Gibson, A. P., Hebden, J. C., Speller, R. D., and Royle, G. J. (2008). Assessing the validity of modulation transfer function evaluation techniques with application to small area and scanned digital detectors. *The Review of scientific instruments*, 79(11):1–6.
- Quelch, K. J., Melick, R. A., Binham, P. J., and Mercuri, S. M. (1983). Chemical composition of human bone. *Archives of oral biology*, 28(8):665–674.
- Ralston, S. H., Urquhart, G. D., Brzeski, M., and Sturrock, R. D. (1990). Prevalence of vertebral compression fractures due to osteoporosis in ankylosing spondylitis. *British medical journal (Clinical research edition)*, 300(6724):563–565.
- Raspanti, M., Guizzardi, S., De Pasquale, V., Martini, D., and Ruggeri, A. (1994). Ultrastructure of heat-deproteinated compact bone. *Biomaterials*, 15(6):433–437.
- Rauch, F. and Schoenau, E. (2001). Changes in bone density during childhood and adolescence: an approach based on bone’s biological organization. *Journal of bone and mineral research*, 16(4):597–604.
- Rebuffel, V. and Dinten, J.-M. (2007). Dual-energy X-ray imaging: benefits and limits. *Insight*, 49(10):589–594.
- Robinson, R. A. (1975). Physicochemical structure of bone. *Clin Orthop Relat Res*, 112:263–315.
- Rossmann, K. (1964). Measurement of the modulation transfer function of radiographic systems containing fluorescent screens. *Physics in Medicine and Biology*, 9(4):551–557.
- Samei, E., Flynn, M. J., and Reimann, D. A. (1998). A method for measuring the presampled MTF of digital radiographic systems using an edge test device. *Medical physics*, 25(1):102–113.
- Shelfbine, S. J., Simon, U., Claes, L., Gold, A., Gabet, Y., Bab, I., Müller, R., and Augat, P. (2005). Prediction of fracture callus mechanical properties using micro-CT images and voxel-based finite element analysis. *Bone*, 36(3):480–488.
- Shuping, R. E. and Judy, P. F. (1978). Resolution and contrast resolution. *Medical Physics*, 5(6):491–496.
- Sorenson, J., Duke, P., and Smith, S. (1989). Simulation studies of dual-energy x-ray absorptiometry. *Medical physics*, 16(1):75–80.
- Speller, R., Pani, S., Tzaphlidou, M., and Horrocks, J. (2005). MicroCT analysis of calcium/phosphorus ratio maps at different bone sites. *Nuclear Instruments and Methods in Physics Research A*, 548(1-2):269–273.

- Stewart, B. and Huang, H. (1990). Single-exposure dual-energy computed radiography. *Medical physics*, 17(5):866–875.
- Taylor, J. R. (1997). *An introduction to error analysis: the study of uncertainties in physical measurements*.
- Teegarden, D., Lyle, R. M., McCabe, G. P., McCabe, L. D., Proulx, W. R., Michon, K., Knight, a. P., Johnston, C. C., and Weaver, C. M. (1998). Dietary calcium, protein, and phosphorus are related to bone mineral density and content in young women. *The American journal of clinical nutrition*, 68(3):749–754.
- Toutountzis, A. (2009). Upgrading dual energy angiography algorithms. Technical report.
- Turner, C. H. and Burr, D. B. (1993). Basic biomechanical measurements of bone: a tutorial. *Bone*, 14(4):595–608.
- Tzaphlidou, M., Speller, R., Royle, G., and Griffiths, J. (2006). Preliminary estimates of the calcium/phosphorus ratio at different cortical bone sites using synchrotron microCT. *Physics in medicine and biology*, 51(7):1849–1855.
- Tzaphlidou, M., Speller, R., Royle, G., Griffiths, J., Olivo, A., Pani, S., and Longo, R. (2005). High resolution Ca/P maps of bone architecture in 3D synchrotron radiation microtomographic images. *Applied radiation and isotopes*, 62(4):569–575.
- Tzaphlidou, M. and Zaichick, V. (2003). Calcium, phosphorus, calcium-phosphorus ratio in rib bone of healthy humans. *Biological trace element research*, 93(1-3):63–74.
- Ulrich, D., van Rietbergen, B., Laib, a., and R uegsegger, P. (1999). The ability of three-dimensional structural indices to reflect mechanical aspects of trabecular bone. *Bone*, 25(1):55–60.
- van Der Linden, J. C., Birkenha, D. H., Verhaar, J. A. N., and Weinans, H. (2001). Trabecular bone’s mechanical properties are affected by its non-uniform mineral distribution. *Journal of biomechanics*, 34:1573–1580.
- van Staa, T. P., Dennison, E. M., Leufkens, H. G., and Cooper, C. (2001). Epidemiology of fractures in England and Wales. *Bone*, 29(6):517–522.
- Vukicevic, S., Marusic, A., Stavljenic, A., Cicak, N., Vogel, M., and Krempien, B. (1988). Talc granulomatosis in the rat: the relationship between osteoblast insufficiency and adjacent bone marrow hyperplasia. *Experimental Hematology*, 16:735–740.

- Wachter, N. J., Augat, P., Krischak, G. D., Sarkar, M. R., Mentzel, M., Kinzl, L., and Claes, L. (2001). Prediction of strength of cortical bone in vitro by microcomputed tomography. *Clinical biomechanics (Bristol, Avon)*, 16(3):252–256.
- Wagner, D. W., Lindsey, D. P., and Beaupre, G. S. (2011). Deriving tissue density and elastic modulus from microCT bone scans. *Bone*, 49(5):931–938.
- Wall, J. C., Chatterji, S. K., and Jeffery, J. W. (1979). Age-related changes in the density and tensile strength of human femoral cortical bone. *Calcified tissue international*, 27(2):105–108.
- Wang, G., Yu, H., and De Man, B. (2008). An outlook on x-ray CT research and development. *Medical Physics*, 35(3):1051.
- Wang, J., Garg, N., Duan, X., Liu, Y., Leng, S., Yu, L., Ritman, E. L., Kantor, B., and McCollough, C. H. (2011). Quantification of iron in the presence of calcium with dual-energy computed tomography (DECT) in an ex vivo porcine plaque model. *Physics in medicine and biology*, 56(22):7305–7316.
- Watanabe, Y., Uotani, K., Nakazawa, T., Higashi, M., Yamada, N., Hori, Y., Kan-zaki, S., Fukuda, T., Itoh, T., and Naito, H. (2009). Dual-energy direct bone removal CT angiography for evaluation of intracranial aneurysm or stenosis: comparison with conventional digital subtraction angiography. *European radiology*, 19(4):1019–1024.
- Webb, S. (1988). *The physics of medical imaging*. Institute of physics publishing, 1 edition.
- Wegrzyn, J., Roux, J.-P., Arlot, M. E., Boutroy, S., Vilayphiou, N., Guyen, O., Delmas, P. D., Chapurlat, R., and Bouxsein, M. L. (2010). Role of trabecular microarchitecture and its heterogeneity parameters in the mechanical behavior of ex vivo human L3 vertebrae. *Journal of bone and mineral research*, 25(11):2324–2331.
- Willnecker, J. (2006). Measurement of bone density and bone strength with pQCT. *Novel approaches towards primate toxicology*, pages 13–19.
- Wilson, E. E., Awonusi, A., Morris, M. D., Kohn, D. H., Tecklenburg, M. M., and Beck, L. W. (2005). Highly ordered interstitial water observed in bone by nuclear magnetic resonance. *Journal of bone and mineral research*, 20(4):625–634.
- Wirtz, D. C., Schi, N., Pandorf, T., Radermacher, K., Weichert, D., and Forst, R. (2000). Critical evaluation of known bone material properties to realize anisotropic FE-simulation of the proximal femur. *Journal of biomechanics*, 33:1325–1330.

- Woodart, H. Q. (1964). The composition of human cortical bone: Effect of age and some abnormalities. *Clinical Orthopaedics and related research*, 37:187–193.
- Wopenka, B. and Pasteris, J. D. (2005). A mineralogical perspective on the apatite in bone. *Materials Science and Engineering*, 25(2):131–143.
- Zaichick, S. and Zaichick, V. (2010). The effect of age and gender on 38 chemical element contents in human femoral neck investigated by instrumental neutron activation analysis. *Biological trace element research*, 137(1):1–12.
- Zaichick, V. and Tzaphlidou, M. (2002). Determination of calcium, phosphorus, and the calcium/phosphorus ratio in cortical bone from the human femoral neck by neutron activation analysis. *Applied radiation and isotopes*, 56(6):781–786.